A dissertation for Degree of Doctor of Philosophy:

グラファイト型窒化炭素を用いた高活性可視光応答型ナノハイブリット光触媒の開発に関する研究

Graphitic Carbon Nitride-based Nanohybrid Photocatalysts with Enhanced Photocatalytic Performance under Visible Light Irradiation

張　啓涛

ＺＨＡＮＧ　ＱＩＴＡＯ

九州工業大学大学院　工学府　物質工学専攻

応用化学分野　機能触媒創製工学研究室

2017 年 2 月

Contents

Chapter 1 General Introduction

1.1. Research background

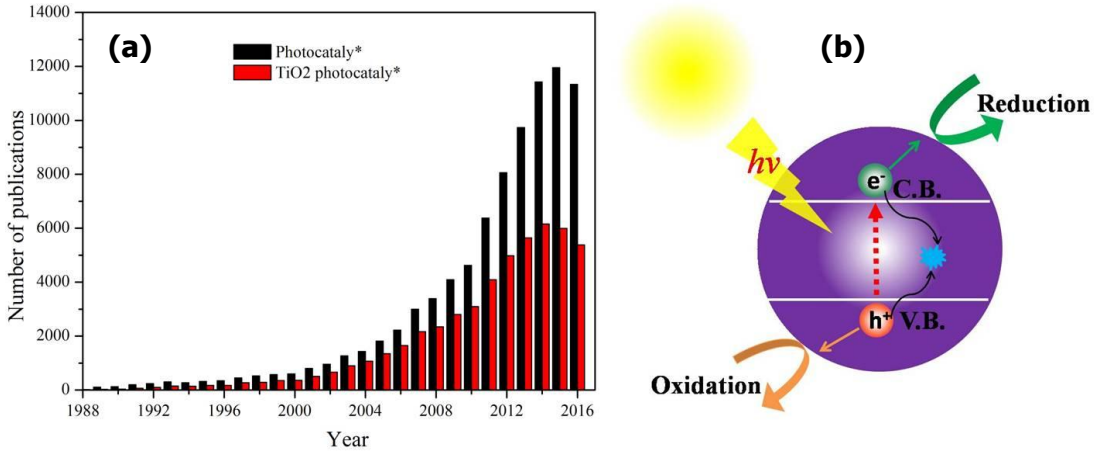

Figure 1 (a) Statistical histogram of annual papers with the keyword of "photocataly*" or "TiO_2 photocataly*" adapted from ISI Web of Science since 1900s; (b) Schematic illustration of a basic photocatalysis process.

Very recently, just as the former president of United States, Barack Obama emphasizes that the momentum of clean energy is irreversible in the latest issue of ***Science***[1]. Accompanying the rapid industrialization and human activity, the issues of environment pollution, CO_2 and other greenhouse gas emission and energy crisis have undoubtedly become our inevitable responsibility to settle. As one of the most cost-effective solutions, photocatalysis technique has been widely adopted to alleviate environment pollution, CO_2 fixation and hydrogen generation since 1990s[2-7], as illustrated by Figure 1a. Distinctly, the number of published papers on photocatalysis presents an exponential growth annually in the past decade. Most importantly, photocatalysis is also a green and cost-effective process, which fully satisfies the requirement of sustainable development for our contemporary society. Because in a typical photocatalysis process (Figure 1b), the photocatalyst can absorb solar lights and then electrons were photo-excited to the conduction band (CB) of the semiconductor, leaving behind the corresponding holes generated in valence band (VB). A portion of

charge carries would undergo recombination in the bulk, and the rest parts transfer to the surface of photocatalyst to involve in the subsequent redox reactions. It is an efficient way to fulfill the conversion of solar energy to chemical energy. Among the numerous investigated photocatalysts, TiO_2-based semiconductor materials, accounting for almost half of the papers related to photocatalyst or photocatalysis, has been turned out to be the most outstanding delegate to degrade various volatile organic compounds (VOCs), dyes and water pollutants as well as hydrogen and oxygen evolution reactions (HER and OER), CO_2 fixation and conversion to hydrocarbon fuels and some other energy-related applications[8-13]. However, as the proverb goes 'a fly in the ointment', TiO_2 photocatalysts are only UV-light-response, because of its relatively wide bandgap (E_g > 3.0 eV). Such intrinsic property greatly hinders its further practical applications. Because the UV light only accounts for 4% in the whole solar spectra, while the visible light occupies 45%. Simultaneously, other numerous inorganic metal oxides (such as ZnO[14-16], SnO_2[17,18], ZrO_2[3,19], NiO[20,21]) also encounter above-mentioned optical absorption restriction. Therefore, the fabrication of a novel polymeric semiconductor with excellent visible-light-driven ability is of necessity and urgency, which can also dramatically complement the drawbacks of conventional inorganic metal oxides. Graphitic carbon nitride is an optimal candidate to satisfy the above requirements.

1.2. Introduction of g-C_3N_4

Graphitic carbon nitride, abbreviated to g-C_3N_4, has been attracted immensely global attention since it was first adopted as a metal-free polymeric semiconductor for photocatalytic water-splitting to produce hydrogen and oxygen in 2009 by Xinchen Wang and his co-workers[22]. Henceforth, the research trends of g-C_3N_4 swerve from superhard properties to photocatalysis features (Figure 2a). Meanwhile, as given in Figure 2b, China, USA, Germany,

Japan and France are the top 5 countries focused on the research of g-C_3N_4-related materials. With intriguing features such as chemical and thermal stability, low cost, ease of preparation and visible light response, applications relevant to g-C_3N_4 prevails in photocatalytic (PC), photoelectrochemical (PEC), photovoltaic (PV), fluorescent bioimaging and some other areas[23]. However, the low specific surface area and fast photogenerated charges and holes greatly obstruct g-C_3N_4 photocatalyst to achieve full potential performance. Therefore, structural or morphological modification means should be employed to enhance its photocatalytic performance.

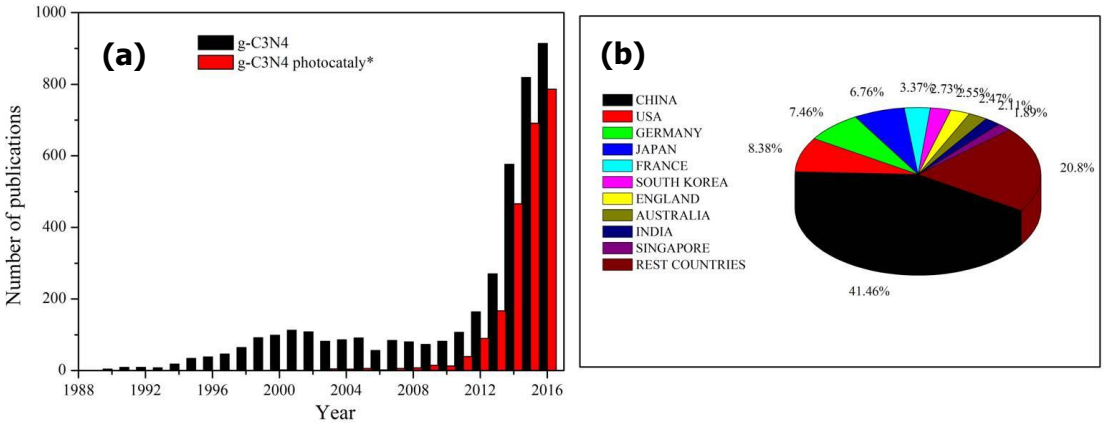

Figure 2 (a) Statistical histogram of annual papers with the keyword of "g-C_3N_4" or "g-C_3N_4 photocataly*" adapted from ISI Web of Science since 1900s; (b) Pie Chart of Top10 countries focus on the investigation of g-C_3N_4-related materials.

1.2.1 History of g-C_3N_4

Actually, g-C_3N_4 is not a novel material because Jöns Jakob Berzelius first mentioned the heptazines in the 1830s when he obtained a polymeric substance by pyrolysis of mercury (II) thiocyanate. At 1834, Justus von Liebig named the polymer material as 'melon'[24]. Much later in 1922, Edward Curtis Franklin discovered that the final calcination product of melon was carbon nitride polymer, denoted $(C_3N_4)_x$. However, restricted by the technical conditions at that time, the author just presented the possible structure of $(C_3N_4)_x$, the real evidence was still ambiguous[25]. In 1937, Linus Pauling proved that Liebig's

melon is a linear polymeric, containing numerous of tri-s-triazine unit bonded via secondary amine group by x-ray crystallography[26]. The unsubstituted heptazine $C_6N_7H_3$ was synthesized by Ramachandra S. Hosmane and others from the group of N. Leonard in the early 1980s[27]. In the ten years since then, the research of melon-based C_3N_4 seemed to be ignored. The exactly structure of C_3N_4 kept unknown because of the chemical stability and insolubility in most solvents. Entering 1990s, the research passions of C_3N_4 had been reignited again since the hardness and modulus of β-C_3N_4 are superior to that of diamond by theoretical prediction[28,29]. Although after tens of years' investigation, it is still as an extremely challenge subject due to the low thermodynamic stability of β-C_3N_4[30]. Moreover, the structure of Liebig's melon-based high polymers were first confirmed in 2001[31]. Up to now, five phases of C_3N_4 was depicted, they are allotropes, denoted as α-C_3N_4, β-C_3N_4, cubic-C_3N_4, pseudocubic C_3N_4 and g-C_3N_4 (subdivided into g-h-triazine, g-o-triazine and g-h-heptazine)[29,32].

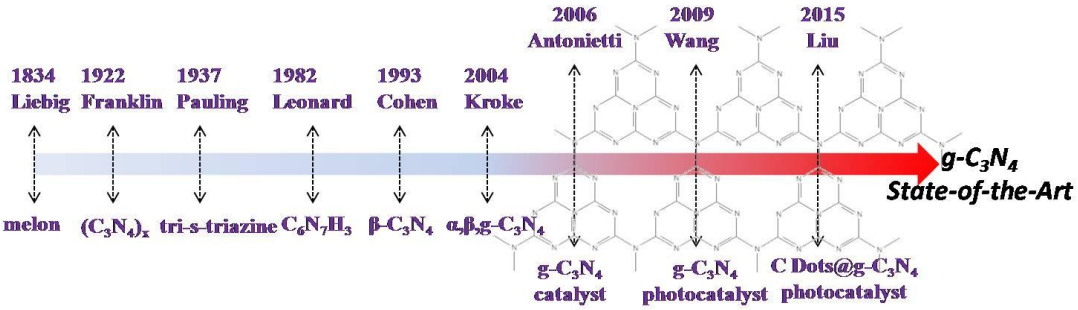

Figure 3 Discovery and development history of g-C_3N_4.

g-C_3N_4, as the most stable allotrope among the five types of C_3N_4 was first used as an efficient metal-free catalyst in Friedel-Crafts reactions for direct activation of benzene in 2006 by Markus Antonietti's group[33]. Three years later, collaborated with Markus Antonietti, Dr. Xinchen Wang adopted g-C_3N_4 as a polymeric photocatalyst to produce H_2 by water-splitting for the first time[22]. It

has turned out to be a great breakthrough and has profound significance to promote the development of artificial photosynthesis. Inspired by the pioneering work of Wang, a vast of functionalized g-C_3N_4 photocatalysts have been fabricated in recent years[23,34-40]. For instance, carbon nanodots (2 ~ 10 nm) were successfully anchored on g-C_3N_4 to prepare a fully metal-free nanocomposite photocatalyst by Liu and co-workers in 2015[39]. The C Dots@g-C_3N_4 photocatalyst achieved 200 days' overall water splitting to produce H_2 and O_2 with 16% quantum efficiencies (QE at 420 nm) and 2% solar-to-hydrogen (STH) efficiencies via a two-electron pathway. Meanwhile, this hybrid photocatalyst also presented mildly active for the overall sea-water photocatalytic splitting under visible light irradiation. Besides, g-C_3N_4 bulks were also successfully exfoliated to multi-layers and even single-layer nanosheet by various approaches, such as liquid-phase exfoliation[35-37], acid/alkaline treatment[41-47] and thermal oxidation etching[34,38]. And highly visible-light responsive g-C_3N_4 has been prepared by foreign elemental doping[48-54] and copolymerization[55-59].

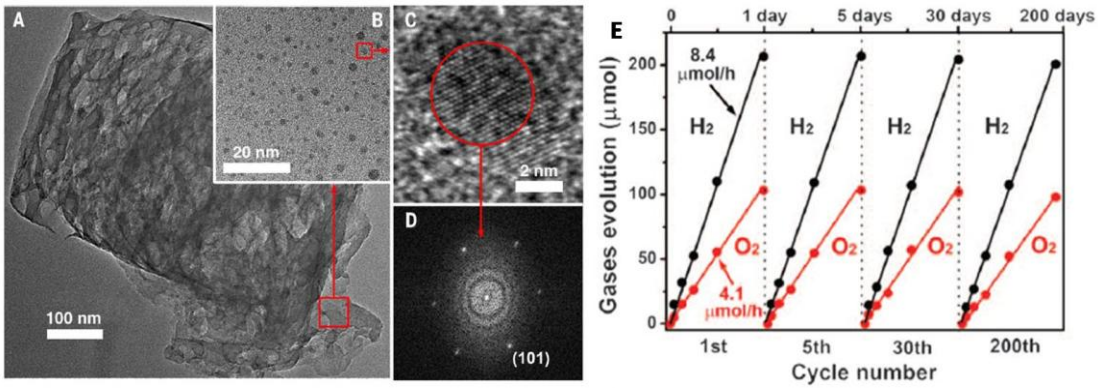

Figure 4 (A) TEM image of the C Dots@g-C_3N_4 composite. (B) A magnified TEM image of the C Dots@g-C_3N_4 region of (A) marked in red. (C) HR-TEM image of a single C Dot embedded in C_3N_4. (D) Corresponding FFT pattern of the crystallite in (C), indicating hexagonal symmetry. (E) Time course of H_2 and O_2 production from water under visible light irradiation (by a 300-W Xe lamp using a long-pass cutoff filter, λ > 420 nm) catalyzed by C Dots@g-C_3N_4. In all panels, the C Dots concentration was 1.6×10^{-5} gCDots/gcatalyst.

1.2.2 Exfoliation of g-C_3N_4

As is known to all, photocatalytic reactions usually occur on the surface of catalysts or interfacial between catalyst and reactants. Typically, the higher of specific surface area (S_{BET}) means the 'active sites' are much more. However, the S_{BET} of pristine g-C_3N_4 is ca. 8 m^2/g because of its densely stacked layers. Such a small S_{BET} greatly obstruct the photoactivity enhancement of g-C_3N_4. If g-C_3N_4 could be fully exfoliated into monolayer, the theoretical S_{BET} could be as high as 2500 m^2/g[60]. Thus, the strategies to delaminating g-C_3N_4 into several nanosheets or even a single atomic layer have drawn extensively attention recent years[40,61,62]. Among the reported methods, liquid phase exfoliation, strong acid/base chemical exfoliation and thermal oxidation etching exfoliation are the most commonly used and extremely efficient approaches[34-38,41-59].

Liquid phase exfoliation: On the one hand, the g-C_3N_4 bulk is a layer-stacked structure with interlayer space distance of 0.33nm. On the other hand, relatively weak van der Waals forces dominate the interlayers of g-C_3N_4. Theoretically, the g-C_3N_4 bulks can be exfoliated into nanosheets as the energy of ultrasonic wave overcomes the van der Waals forces between interlayers dispersed in certain solvents[63]. In fact, it really works experimentally. Similar with the exfoliation of graphite into 2D nanosheets called graphene[64], g-C_3N_4 nanosheets are also obtained by many research groups[34-38,41-47]. For example, via ultrasonication-assisted liquid phase exfoliation method, g-C_3N_4 nanosheets with 2 nm thickness (ca. 6~7 layers) were successfully exfoliated by Wang's group[35]. It was found that the exfoliation efficiency greatly depended on the adopted solvent. Among the following 5 solvents: isopropanol (IPA), N-methyl-pyrrolidone (NMP), water, ethanol, and acetone, as shown in Figure 5(A), IPA exerted the optimal exfoliation efficiency and it was also proved as the most promising solvent in many other previously reported papers for preparation nanosheets of MoS_2, BN and Graphene[65]. In detail, the below empirical

equation is prone to evaluate the exfoliation effectiveness for layered materials in designated solvent[66,67]: $\Delta H_{Mix}/V_{Mix} = [2\varphi(\delta_G - \delta_{sol})^2]/T_{sheet}$ (ΔH is enthalpy of mixing, δ is the square root of the component surface energy, φ is the nanosheet volume fraction, and T is the thickness of nanosheets). According to the above equation, g-C_3N_4 and IPA have the well-matched surface energies, thus IPA affords outstanding delaminated effect for g-C_3N_4 bulks. Remarkably, compared with g-C_3N_4 bulk, the exfoliated g-C_3N_4 possesses many excellent properties: extremely high specific surface area (384 m^2/g), significantly reduced charge transfer resistance (75% down) and ultra-long storage time without sedimentation (4 months). These improvement factors synergistically endowed better photocatalytic performance for H_2 evolution by g-C_3N_4 nanosheets, as illustrated in Figure 5(a-d).

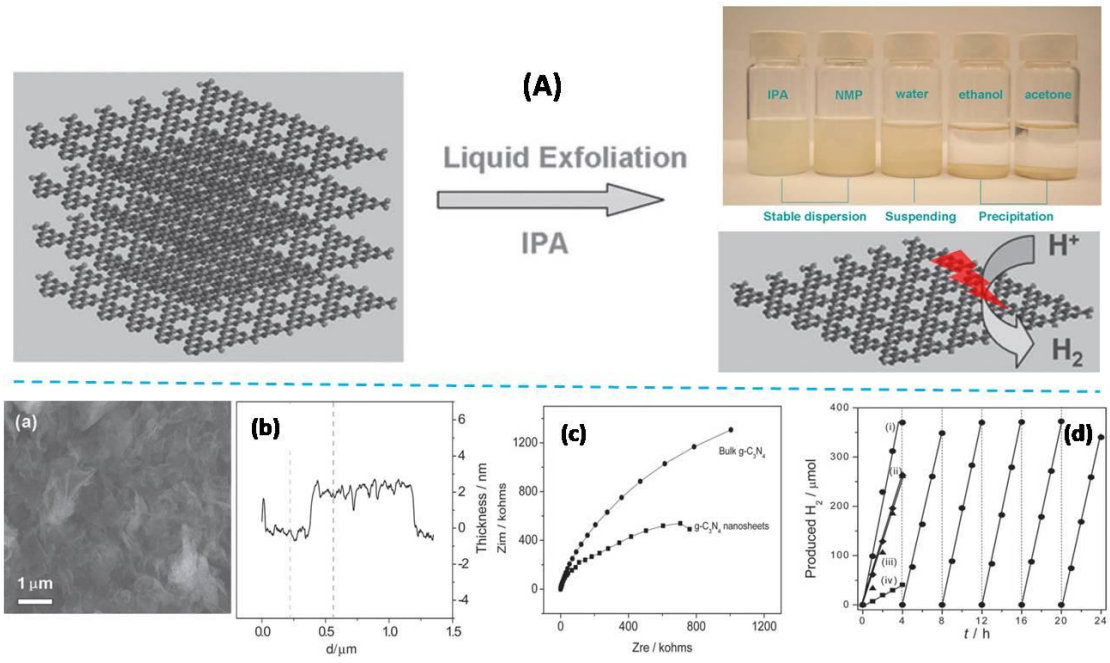

Figure 5 (A) Fabrication of g-C_3N_4 nanosheets by a liquid-exfoliation method. Characterization results of as-prepared g-C_3N_4 nanosheets (a) SEM; (b) AFM; (c) EIS and (d) Photocatalytic activities for H_2 evolution by: i) exfoliated g-C_3N_4 nanosheets, ii) g-C_3N_4 nanosheets synthesized by thermal exfoliation, iii) highly ordered mesoporous g-C_3N_4, and iv) bulk g-C_3N_4. Reaction conditions: 50 mg of catalyst loaded with 3 wt% of Pt co-catalyst; 100 mL of H_2O containing 10 vol% triethanolamine; 300 W Xe lamp with a 420 nm cut-off filter.

Acid/base chemical exfoliation: g-C_3N_4 nanosheets prepared by liquid phase exfoliation approach are often time-consuming (more than 10 h ultrasound), low yield (< 10%) and extremely low solid concentration (less than 0.3 mg/mL)[36]. Therefore, acid/base chemical exfoliation methods are widely regarded as an efficient alternative way to fabricate g-C_3N_4 nanosheets with high yield[41,43-47,68]. For instance, Sano and coworkers developed g-C_3N_4 nanosheets decorated with considerable mesopores by basic hydrothermal treatment[43]. As illustrated in Figure 6, the unstable domain in g-C_3N_4 bulks could be removed by hydrolysis reaction with the aid of 0.1M NaOH aqueous. The S_{BET} of obtained g-C_3N_4 (denoted as HT-g-C_3N_4) was increased 8 times higher than that of its counterpart, resulting in much more active sites and faster transfer and separation for photogenerated charge carriers. Coincidently, the photooxidation activity under visible light irradiation for NO conversion by HT-g-C_3N_4 was promoted 8.6 times up compared with the unmodified g-C_3N_4.

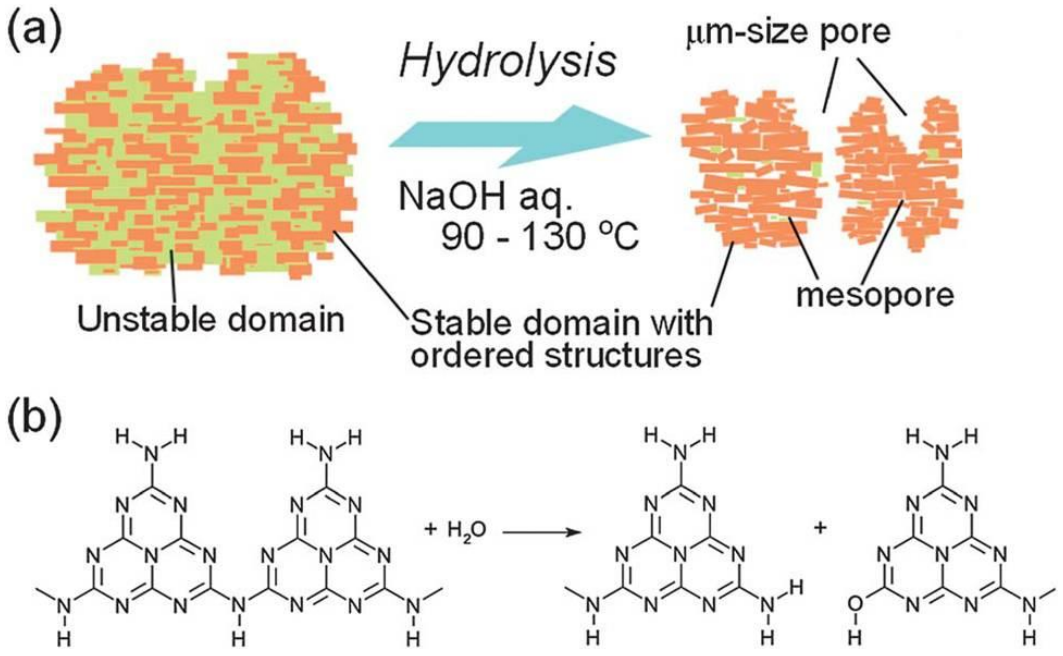

Figure 6 (a) Formation scheme of HT-g-C_3N_4 with a porous structure by alkaline hydrothermal treatment and (b) hydrolysis reaction scheme of g-C_3N_4

Similarly, incorporation of the concentrated H_2SO_4 (50% ~ 98%) and H_2O is also an effective and widely used intercalator for g-C_3N_4 exfoliation[44,45,69,70]. Because H_2SO_4 molecules can easily intercalate into space of g-C_3N_4 interlayer, and then the fast exfoliation happens as the rapid exothermic effect introduced by H_2O. Very early, concentrated H_2SO_4 together with K_2MnO_4 are usually adopted as strong oxidants to exfoliate graphite into 2D nanosheets[71,72]. Likewise, it is also effectual for g-C_3N_4 delamination. For example, single-layer g-C_3N_4 nanosheet was exfoliated by Zhu et al[44]. As AFM and HR-TEM measurement results displayed in Figure 7, the as-prepared g-C_3N_4 consists of numerous small-size fragments with a thickness of 0.4 nm, which is attributed to the cleavage of unstable bridged -NH- groups. From the low-angle shifted XRD peak of monolayer g-C_3N_4, it indicated that lattice spacing was enlarged greatly, changing from 0.325 nm to 0.356 nm. And the generated photocurrent of monolayer g-C_3N_4 is 4 times higher than that of g-C_3N_4 bulks, manifesting that the efficiency of photoinduced charge carries was promoted significantly.

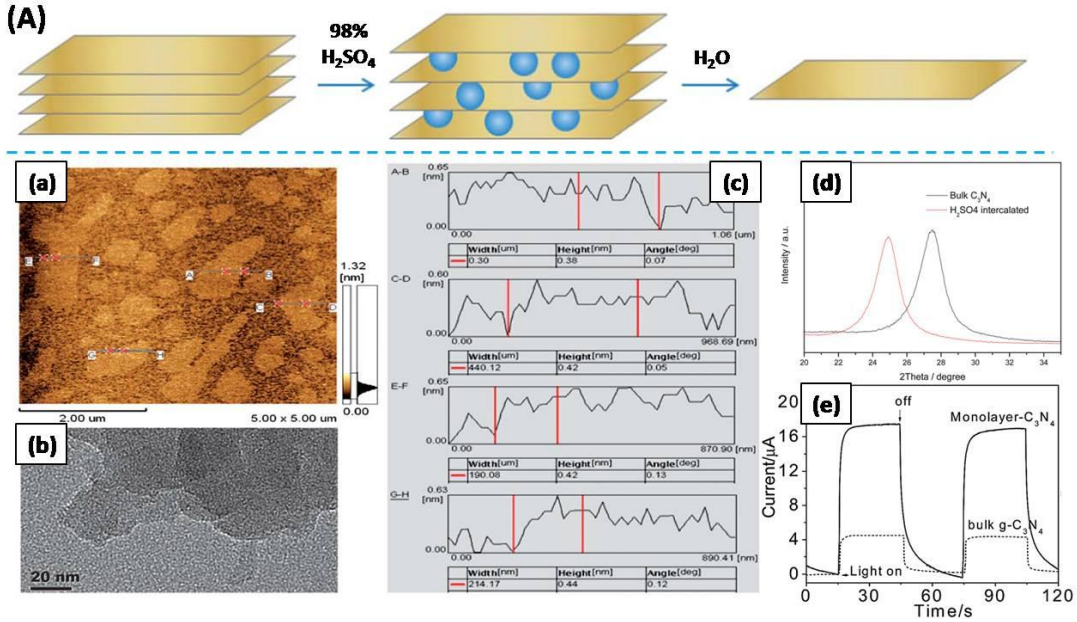

Figure 7 (A) Illustration of H_2SO_4 assisted exfoliation method. Characterization of single-layer g-C_3N_4 nanosheet by (a) AFM; (b) HR-TEM; (c) Height profiles; (d) XRD and (e) Photocurrent response under chopped illumination

Thermal oxidation etching exfoliation: Apart from the above-mentioned exfoliation methods, thermal oxidation etching exfoliation is also an efficient way to prepare g-C_3N_4 nanosheets[34,38]. It is also a much more cost-effective and environmental friendly way to produce g-C_3N_4 nanosheets on a large scale, which was first published on ***Adv. Funct. Mater.*** by Liu's group in 2012[34]. Given in Figure 8, the thickness of the nanosheets is easy to modulate by controlling the time of thermal oxidation in static air at 500 ℃. Via only 2 hours thermal oxidation etching, the S_{BET} of g-C_3N_4 nanosheets (with 2 nm thickness) is remarkably enlarged as high as 306 m^2/g. Moreover, the shortest lifetime of charge carries for g-C_3N_4 nanosheets was elongated from 1.327 ns to 1.926 ns. Consequently, better activity for •OH radical generation and H_2 production was achieved by thermal oxidation etched g-C_3N_4 nanosheets.

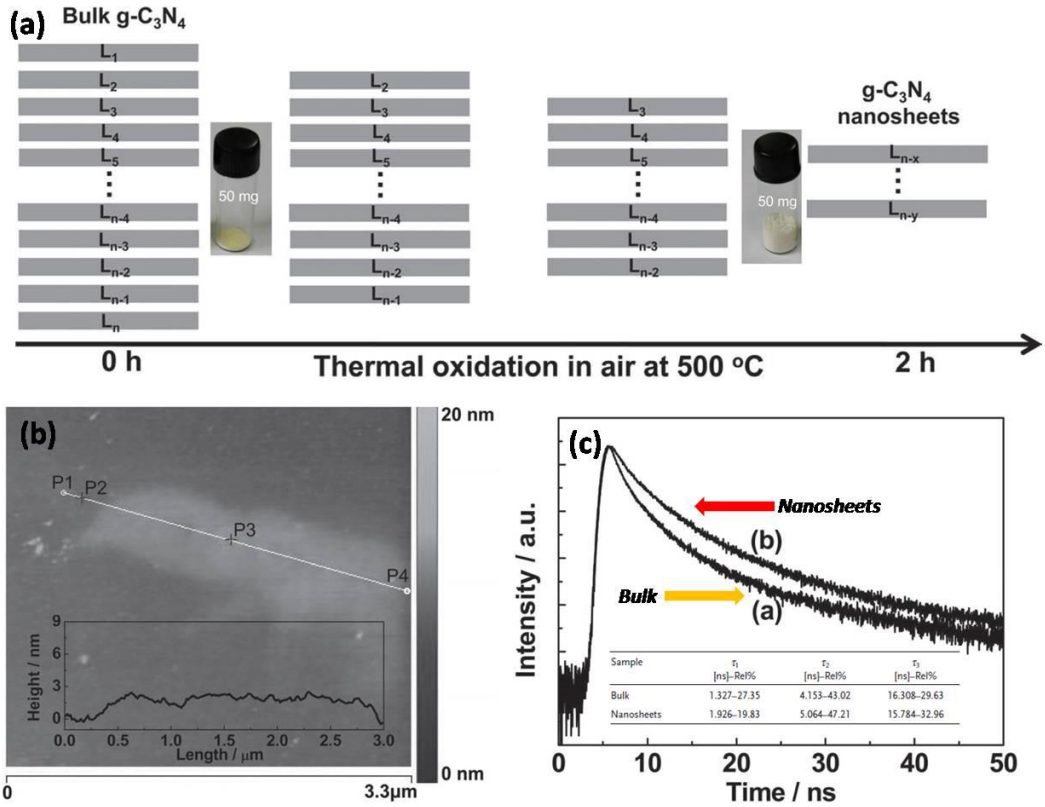

Figure 8 (a) Schematic of the formation process of g-C_3N_4 nanosheets by thermal oxidation etching exfoliation method; (b) AFM image of g-C_3N_4 nanosheets and (c) Time-resolved fluorescence decay spectra excited by the incident light of 330 nm from a picosecond pulsed light-emitting diode.

1.2.3 Fictionalization methods of g-C_3N_4

Although g-C_3N_4 has been universally acknowledged as efficient photocatalyst, its visible-light absorption edge is just around 460 nm[22]. This means pristine g-C_3N_4 can only utilize a small part of visible spectra in solar light, resulting in the relatively weak photocatalytic performance. Meanwhile, the photogenerated electrons and holes are prone to encounter fast recombination. Therefore, effective measurements should be adopted to overcome these shortcomings. Fortunately, doping chemistry and copolymerization methodology open new avenues and have turned out to be cost-effective countermeasures by a large number of studies[48-59]. Different with the pure carbon materials[73,74] such as Fullerene, CNTs, Graphene, Diamond and CNFs, etc., as given in Figure 9, g-C_3N_4 polymeric semiconductor contains plenty of sp^2 and sp^3 hybridized nitrogen atoms as well as numerous residual amine functional groups, providing an intriguing platform with much more superiority to achieve the functionalization of g-C_3N_4 photocatalyst by foreign elemental doping and copolymerization. Thus far, series of intriguing g-C_3N_4 photocatalysts have been synthesized by various functionalized approaches[75-81].

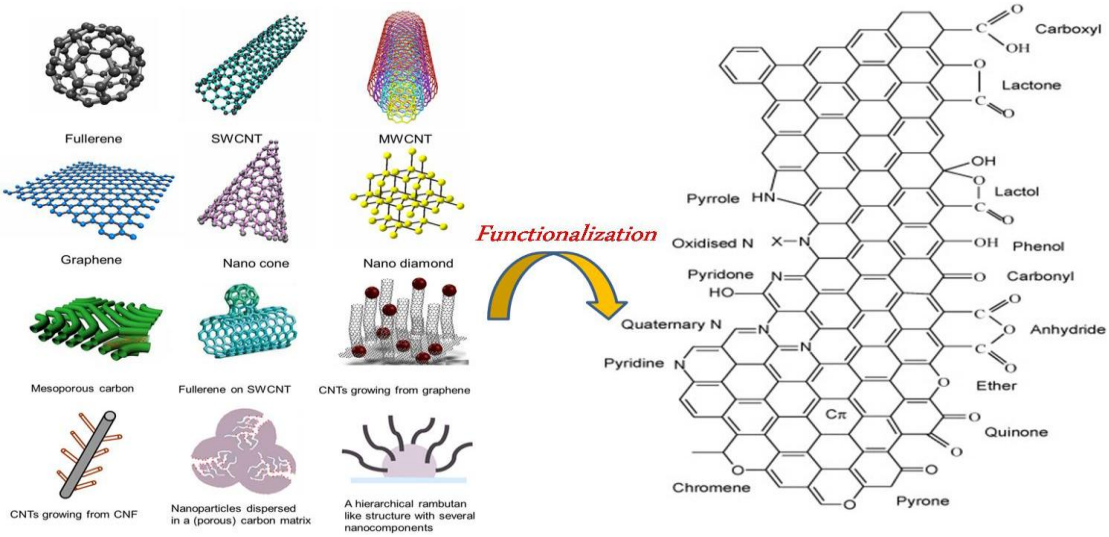

Figure 9 Structure and functionalization for pure carbon materials

Doping by nonmetal elements: g-C_3N_4, as a CN conjugated polymer, is composed of heptazine units, connected by primary, secondary and tertiary amines. Besides, DFT calcination results also indicate that the optical absorption, electrical density, luminescent emission and some other physicochemical properties can be well regulated by foreign elemental doping. Thus far, C[82,83], N[84], O[51,52,85-88], S[50,89-95], P[49,53,96-104], B[105-110], F[111,112] and I[113-115] elements have been successfully doped into g-C_3N_4 framework to modulate the visible light absorption and its photoredox abilities of as-prepared photocatalyst. Herein, take O-doped g-C_3N_4 as an example, O-doped g-C_3N_4 photocatalyst was first established by Chen et al[51]. A facile H_2O_2 hydrothermal treatment method was adopted to introduce O atoms into g-C_3N_4 framework. Direct evidence of N-C-O formation (531.6 eV) was given in Figure 10(a), such N-C-O species still remained even after 60 s Ar^+ etching. Besides, the absorption edge of g-C_3N_4 was red-shifted from 460 nm to 500 nm after O-doping and S_{BET} was also increased 5 times due to the generation of abundant mesoporous. The aforementioned modification consequently contributes to the enhanced photocatalytic performance for H_2 evolution by the O-doped g-C_3N_4. Recently, Huang and co-workers further develop O-doped g-C_3N_4 with simultaneous porous network and O-doping for efficient solar-energy-driven hydrogen evolution[52]. As displayed in Figure 11, hydrogen bonded melamine-H_2O_2 supramolecular aggregates were used as precursors to fabricate a highly porous O-doped g-C_3N_4 photocatalysts. The pore size distributions and O doping concentration can be easily controlled by altering the addition content of H_2O_2. DFT simulation results manifested that O doping preferentially substitutes the two-coordinated N position of CN conjugated framework, resulting in a narrowed bandgap for O-doped g-C_3N_4. Therefore, the introduced mesopores and O-doping greatly enhanced the light harvesting and charge carries separation, synergistically promoting the enhancement of photocatalytic activity.

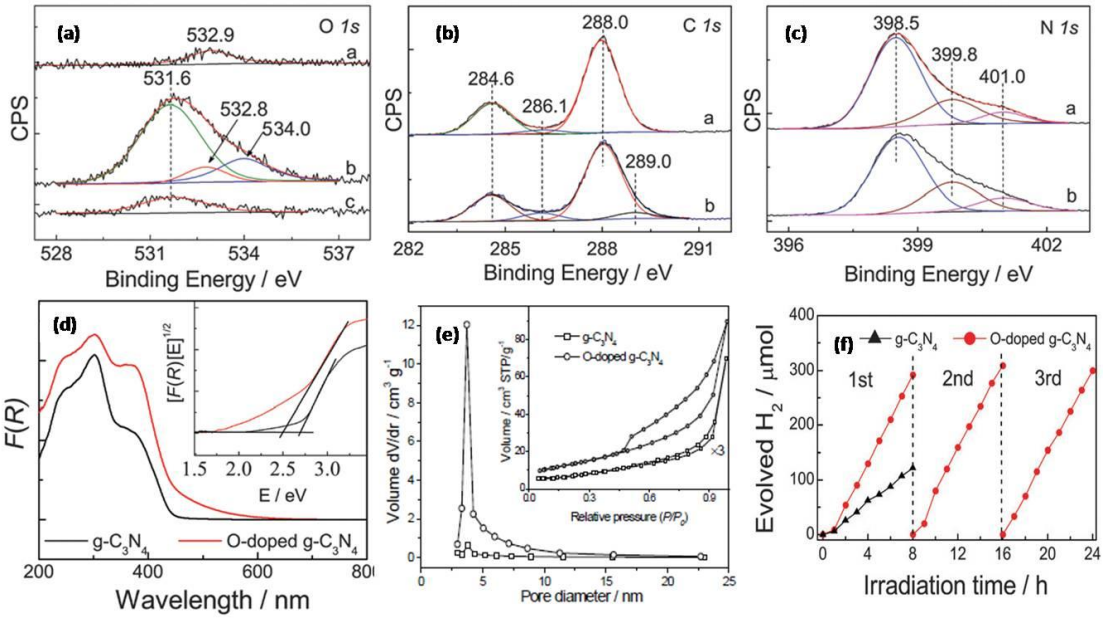

Figure 10 (a-c) O1s, C1s and N1s XPS spectra (insets of a: pristine g-C_3N_4, b: O-doped g-C_3N_4, c: O-doped g-C_3N_4 after 60s Ar+ etching); (d) UV-vis; (e) The pore size distributions and BET isotherms at 77K and (f) Photoactivity of H_2 evolution under visible light irradiation.

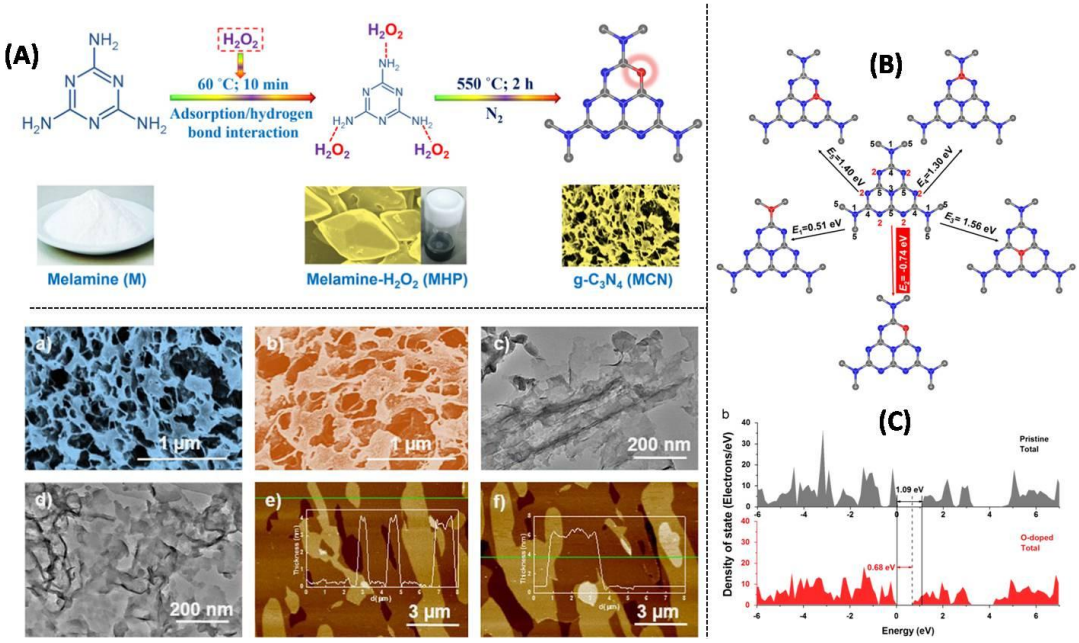

Figure 11 (A) Formation schematic of the O-doped g-C_3N_4; (B) Calculated formation energy of O-doped g-C_3N_4; (C) calculated DOS plots; (a, c, e) SEM, TEM and AFM images of 1.5mol%O-doped g-C_3N_4 and (b, d, f) SEM, TEM and AFM images of 3mol%O-doped g-C_3N_4. (C, N and O are indicated by gray, blue and red spheres, respectively.)

Doping by metal elements: In addition to nonmetal elements doping, metal elements are also apt to incorporate by g-C_3N_4. Because the size of regularized nitrogen pore unit in g-C_3N_4 is suitable to accommodate many metal ions, such as Fe[48,49,116,117], Cu[79,118,119], Zn[120], Ni[121,122], Co[123,124], Mn[125,126] and so forth. As early as 2009, Wang and coworkers introduced Zn^{2+} and Fe^{2+} into g-C_3N_4 network for the first time[49]. As depicted in Figure 12(a-c), it demonstrated that strong host-guest interaction between Fe and nitrogen pores exerted the extended visible light absorption edge with increasing Fe content in the Fe/g-C_3N_4 hybrids. Similar results were also obtained by Zn-doped g-C_3N_4. Moreover, K-doped g-C_3N_4 with better separation efficiency of charge carries and absorption ability for visible light was prepared by Dong et al[54]. DFT revealed that K atoms were intercalated into the g-C_3N_4 interlayer via bridging bonds, decreasing the electronic localization and extending the π-π conjugated system. Thus K-doped g-C_3N_4 possessed better activity for NO removal.

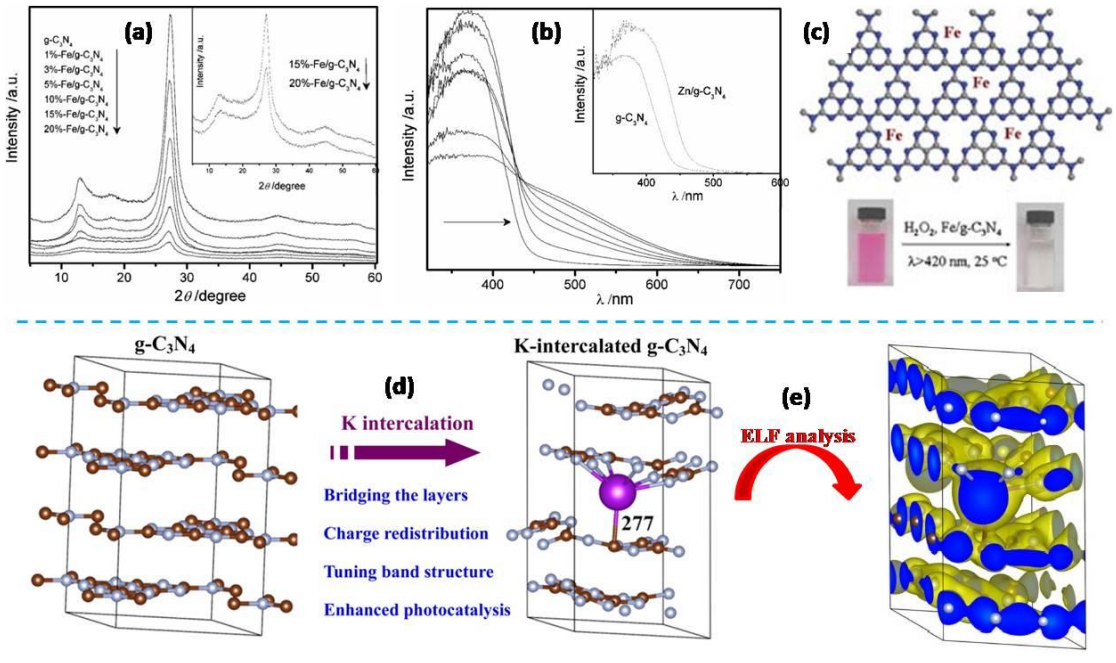

Figure 12 (a) XRD patterns (b) UV-vis spectra (c) Structural schematic of Fe-doped g-C_3N_4; (d) Calculated crystal structure and (e) Electronic location function (ELF) analysis of K-doped g-C_3N_4. The yellow region denotes charge depletion while blue region denotes accumulation. The isosurface is 0.01 e/$Å^3$.

Copolymerization of g-C_3N_4: It is well known that there are plenty of functional groups (-NH_2, -NH- and -C≡N) contained in the precursors or intermediates of g-C_3N_4. Therefore, copolymerization method is a good choice to adjust the optical absorption, electronic properties, and band structure of g-C_3N_4[75]. To date, a number of π-rich comonomers and π-deficient aromatic systems have been both implemented[55-59,75,127-134]. Detailedly, the efficient comonomers are listed as following: barbituric acid[55,132], 2-aminobenzonitrile (ABN)[56], diaminomalenitrile acid (DAMN)[129], 2-aminothiophene-3-carbonitrile (ATCN)[129], phenylurea[128], quinolone[133], pyromellitic dianhydride[75], pyromellitic diimide (PDI)[57,58], biphenyl diimide (BDI)[59], 2,6-diaminopyridine[130], 2,4,6-triaminepyrimidine[131], 3-aminothiophene-2-carbonitrile[127], terephthaladehyde[134] and so forth. For instance, as demonstrated in Figure 13, the charge separation and visible absorption were ameliorated conspicuously.

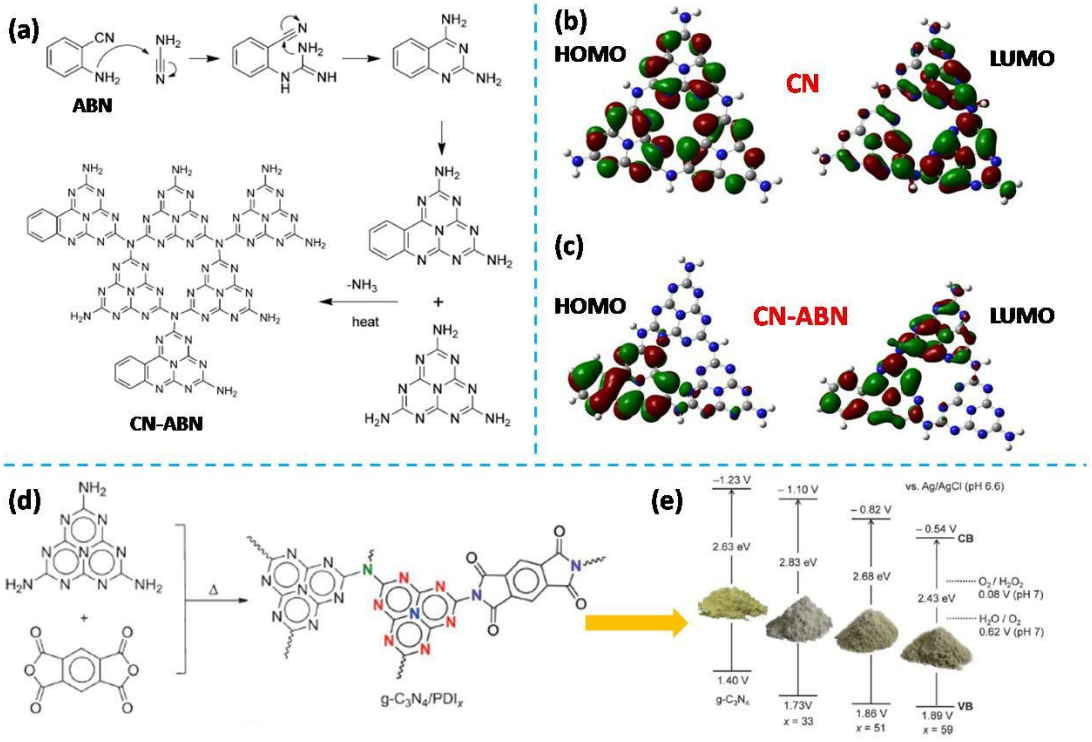

Figure 13 (a) Copolymerization reaction scheme of cyanamide with 2-aminobenzonitrile (ABN); DFT models calculated for (b) CN trimers and (c) CN-ABN trimers; (d) Synthesis of g-C_3N_4/PDI_x and (e) Electronic band structures of g-C_3N_4 and g-C_3N_4/PDI_x.

1.2.4 g-C_3N_4-based heterojunction photocatalysts

The bandgap information of g-C_3N_4 polymeric semiconductor and various famous inorganic semiconductors are illustrated in Figure 14. Valence band (VB) and conduction band (CB) of g-C_3N_4 locate at 1.4 V and -1.3 V (vs.NHE), respectively. Referring to the redox potentials at pH 7.0 for water-splitting, CO_2 conversion and pollutant degradation, g-C_3N_4 photocatalyst is of capacity for above chemical reactions in theory[23]. But g-C_3N_4 can't generate ·OH from H_2O and OH^-, greatly restricted the enhancement of photooxidation ability. Besides, the rapid recombination rate of photogenerated electrons and holes is another vital shortcoming for pristine g-C_3N_4. Thus, efficient strategies should be employed to overcome these demerits. The construction of g-C_3N_4-based heterojunction nanohybrids has drawn innumerable attention recent years[23,61,62,133,135,136]. Up to now, multifarious heterojunction g-C_3N_4-based photocatalysts have been established, including metal/g-C_3N_4 (Pd[137-139], Pt[140-142], Cu[143], Rh[144], etc), LSPR metal/g-C_3N_4 (Au[145,146], Ag[147,148], Bi[149], etc), metal complex/g-C_3N_4 (Ru[150], Co[151], Co-Pi[152], etc) metal oxide/g-C_3N_4 (TiO_2[153-155], ZnO[156-158], WO_3[159-162], etc), metal sulfide/g-C_3N_4 (CdS[163,164], MoS_2[165-167], ZnS[168], etc), isotype g-C_3N_4[135,169], carbon/g-C_3N_4 (C60[170], CNT[171,172], graphene[173-175], etc) and polymer/g-C_3N_4(PANI[176], P3HT[177,178], PPy[179,180], etc). Among them, Z-scheme g-C_3N_4-based heterojunction photocatalysts are of utmost challenging to surmount but with significant meanings. Because Z-scheme based heterojunction photocatalyst can maximize the redox abilities of its integrated components, overcoming the drawback of charge separation-type heterojunction photocatalyst[23,62,154,155,160,162,181]. For example, our group successfully fabricated an efficient Z-scheme WO_3/g-C_3N_4 heterojunction photocatalyst by a facile planetary milling method[154,160,162]. The established heterojunction structure can greatly inhibit the conversion of W^{6+} to W^{5+}, which is well corroborated by DB-PAS and UV-vis spectra, as illustrated in Figure 15.

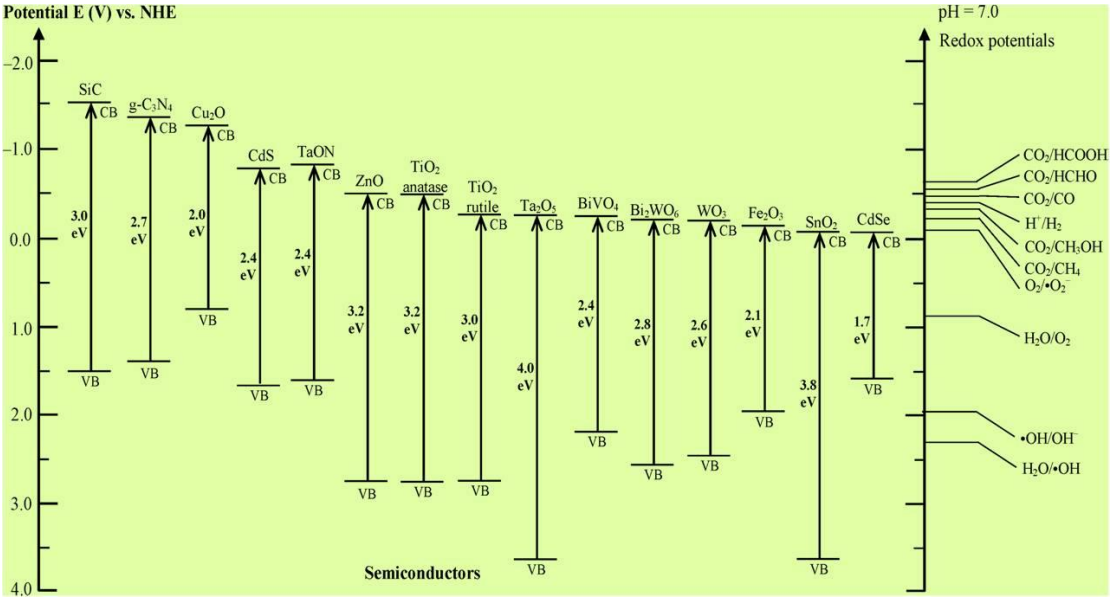

Figure 14 Band energy level diagrams of various semiconductors photocatalysts.

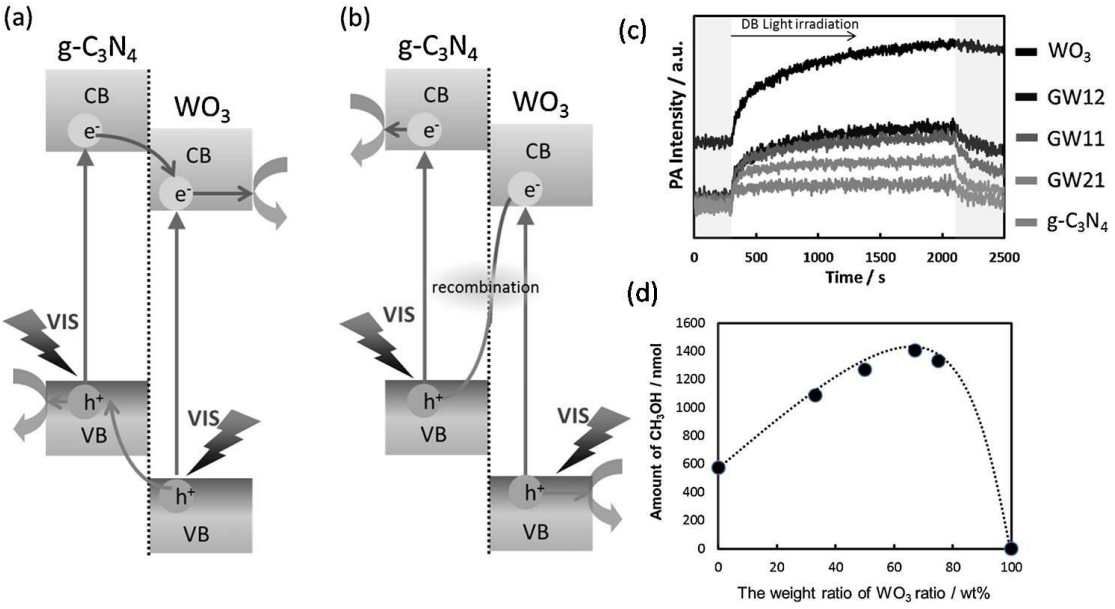

Figure 15 Proposed photocatalytic reaction mechanisms of the WO_3/g-C_3N_4 hybrid photocatalysts: (a) Charge separation type and (b) Z-scheme type; (c) DB-PAS spectra of WO_3/g-C_3N_4under visible light irradiation in the presence of EtOH under N_2 and O_2 atmosphere and (d) Photoreduction CO_2 to CH_3OH by hybrid photocatalyst as a function of the content ratio of g-C_3N_4 and WO_3 (3 mg photocatalyst under LED 435 nm with intensity of 3 mw/cm^2).

1.2.5 Applications of g-C_3N_4

As everyone knows, conventional energy depletion (coal, petroleum and natural gas), greenhouse effect and environmental pollution have been well recognized as inevitable issues desiderated to figure out in contemporary society. Luckily, the development of photocatalysis technology opens a cost-effective avenue to break the impasse. As a novel polymeric semiconductor, g-C_3N_4 has become a brilliant figure in artificial photosynthesis and environmental remediation since the pioneering work by Wang and coworkers in 2009[22], because of its visible-light responsive, abundant, thermal/chemical stability, low-cost, non-toxic and easy to scale up. As shown in Figure 16, g-C_3N_4-based photocatalysts have been widely applied in water splitting to produce H_2[22,35,38,50,55,56,140,182], CO_2 conversion to chemical fuels[110,150,151,162,183] and pollution degradation[54,68,154,160]. For instance, Martin and coworkers developed a dramatically efficient urea-derived g-C_3N_4 photocatalyst[182], showing a H_2 evolution rate of 20000 μmol h^{-1} g^{-1} and 3300 μmol h^{-1} g^{-1} under full arc and visible light irradiation, respectively. Most importantly, this g-C_3N_4 photocatalyst is also stable with 26.5% internal quantum yield. DFT calculation results proved that the N protonation greatly affected the CB edge (0.34 eV down-shifting), lowering the overpotential for H_2O reduction reaction (Figure 17(a-c)). Furthermore, due to its stable nonpolar structure and high activated energy, CO_2 photoreduction is a much more knotty issue. Maeda's group selected ruthenium complex as CO_2 catalytic center while g-C_3N_4 acts as light-harvesting units (Figure 17(d-f))[150]. The electrons generated from g-C_3N_4 smoothly injected to Ru complex reaction sites, promoting the conversion of CO_2 to HCOOH with a turnover number of greater than 1000 and an apparent quantum yield of 5.7% at 400 nm. Our group developed Z-scheme type S-doped TiO_2/g-C_3N_4 heterjunction photocatalyst with excellent photocatalytic activity for CH_3CHO degradation, presented in Figure 17(g-i)[154].

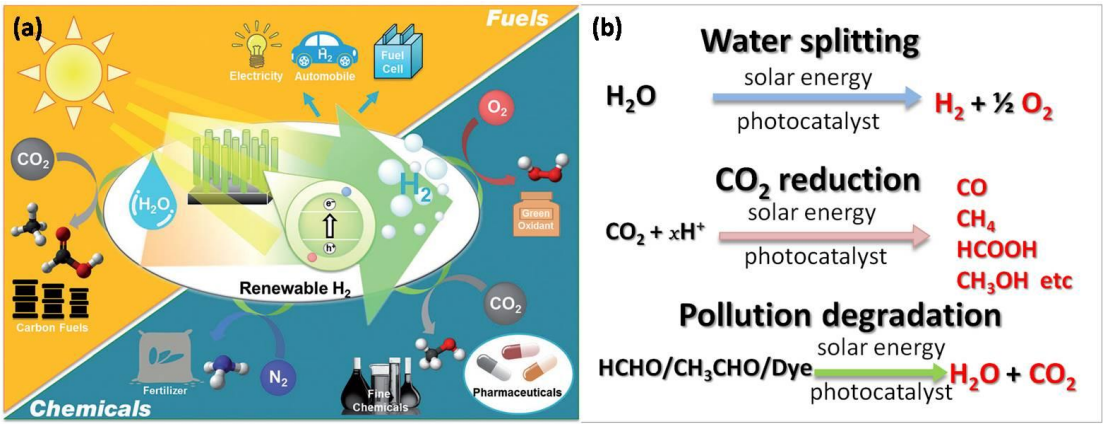

Figure 16 (a) The role of artificial photosynthesis in green chemistry; (b) Three main applications of g-C_3N_4-based photocatalysts.

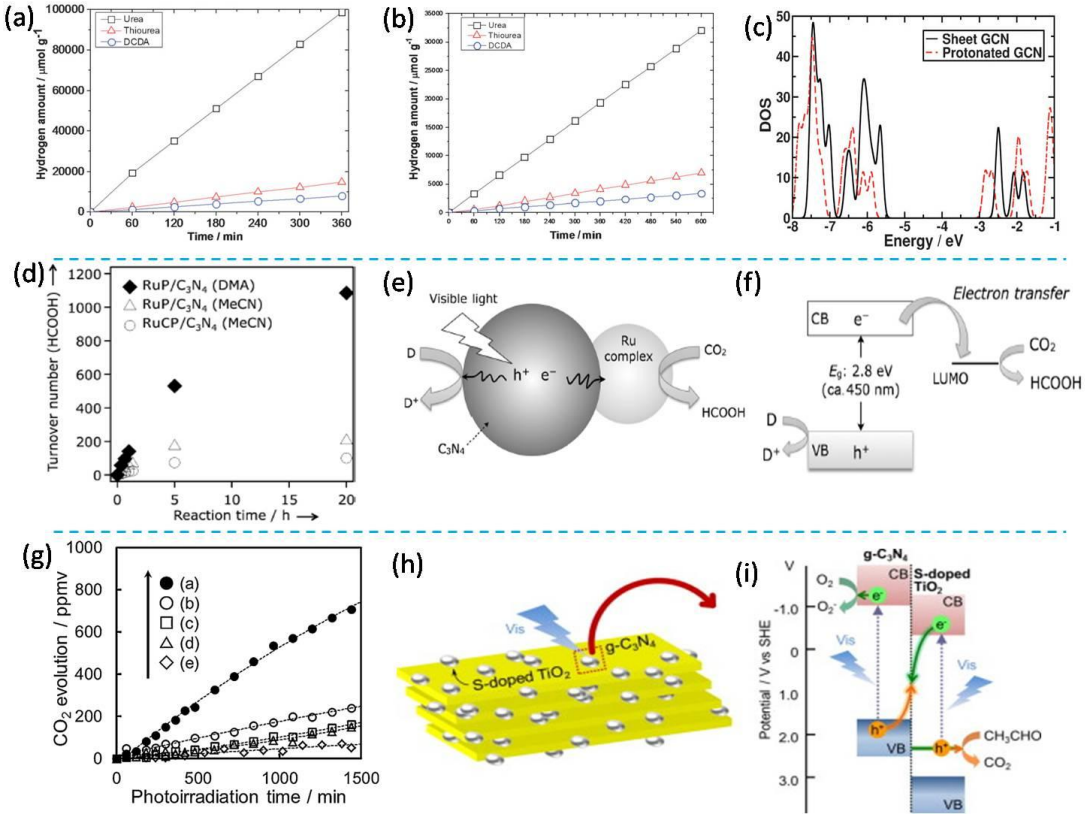

Figure 17 (a-c) Hydrogen evolution with a 300 W Xe lamp, 20 mg catalyst, 3 wt% Pt, and TEOA as a hole scavenger: (a) full arc, (b) λ≥395 nm, (c) total density of states for sheet g-C_3N_4 and protonated g-C_3N_4. (d-f) Carbon dioxide reduction using a Ru complex/g-C_3N_4 hybrid photocatalyst with a 400 W Hg lamp, 8 mg catalyst, and 20% TEOA as a hole scavenger: (d) turnover number of HCOOH production, (e) structure description, (f) band energy diagram. (g-h) Acetaldehyde (500 ppm) degradation by S-doped TiO_2/g-C_3N_4 with a 500 W Xe lamp, 12 mW/cm^2 intensity, 200 mg catalyst: (g) Time courses of CO_2 evolution, (h) structure description, (i) proposed mechanism.

1.3 Research purposes

In this thesis paper, we focus on the modification research related to g-C_3N_4-based photocatalysts. In order to overcome the shortcomings of pristine g-C_3N_4: low specific surface area, insufficient visible light absorption, weak photooxidation capacity and rapid recombination of photogenerated electrons and holes, a series of cost-effective solutions were adopted in our study. Multifarious types of intriguing g-C_3N_4 photocatalysts with enlarged S_{BET} and extended visible-light responsive have been successfully prepared by various physicochemical modification approaches, such as planetary milling, hydrothermal treatment, selenium assisted exfoliation, copolymerization with and two steps thermal oxidation treatment. Most importantly, the photocatalytic activity for CH_3CHO and 2-propanol oxidation of g-C_3N_4 was extremely promoted by morphology controlled CeO_2 nanocrystals. Meanwhile, the photoelectrochemical performance for CO_2 conversion to fuels was also ameliorated by this CeO_2/g-C_3N_4 nanohybrid photocatalysts. The promotion mechanism was also proposed. Besides, some other g-C_3N_4-based heterojunction photocatalysts were also fabricated by the established method (such as $Bi_2O_2CO_3$/g-C_3N_4, NiO/g-C_3N_4, and CeO_2/g-C_3N_4-Rods), which were also exemplified with excellent photocatalytic activities. Finally, we developed a simple route to purify the intermediate of melem oligomers and then hybridized with CeO_2 nanocrystals, which was adopted as a much more efficient nanohybrid photocatalyst for CH_3CHO and 2-PrOH oxidation in our study for the first time. Therefore, graphitic carbon nitride-based nanohybrid photocatalysts with enhanced photocatalytic performance under visible light irradiation were successfully prepared in this study. It also provides a cost-effective way to fabricate other efficient nanohybrid photocatalysts for environmental purification, water-splitting to H_2/O_2 and CO_2 conversion to high value-added fuels.

Chapter 2 Preparation and properties of pristine g-C_3N_4 bulks

2.1 Introduction

In this section, various g-C_3N_4 bulks were prepared from different N-riched precursors by a facile thermal condensation method. Urea, dicyandiamide and melamine were adopted as raw materials, their structural information and physical properties were given in Figure 18. With increasing the temperature to certain value, the light yellow powders would be obtained, denoted as CN-U, CN-D and CN-M, representing Urea, dicyandiamide and melamine derived g-C_3N_4 photocatalysts, respectively. Via XRD, SEM, BET, FTIR, UV-vis, PL and XPS measurements, the crystallinity, morphology, optical and electrical properties of as-prepared g-C_3N_4 photocatalysts were discussed. Finally, the photocatalytic performance of g-C_3N_4 bulks was evaluated by acetaldehyde (CH_3CHO) degradation under visible light irradiation.

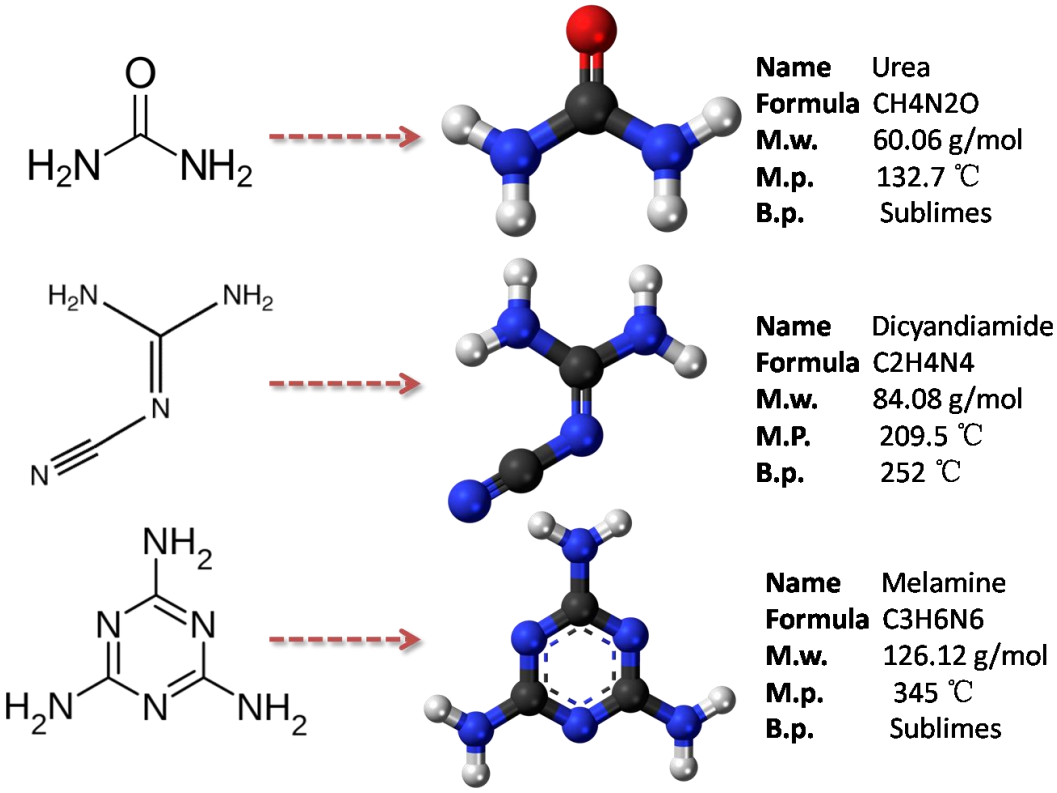

Figure 18 Structural information and physical properties of N-riched precursors.

2.2 Experimental

2.2.1 Materials

All of the reagents were of analytical grade and were used as received. Deionized water (18.4 MΩ, PURELAB flex3 water systems) was used in all of the experiments. Urea, Dicyandiamide and Melamine were purchased from Wako Pure Chemical Industries, Ltd. Acetaldehyde was purchased from Sigma-Aldrich. Because acetaldehyde VOCs are extremely toxic and carcinogenic, thus the use of personal protective equipmentis is required. Pure Air (CO_2 < 0.1 ppm) is a product of Taiyo Nippon Sanso.

2.2.2 Preparation of samples

Typically, g-C_3N_4 bulks were prepared according to the previously reported method with a slight modification[184]. Briefly, thirty grams of melamine (Urea or Dicyandiamide) was placed in an alumina crucible with a cover and then heated to 550℃ under dynamic air atmosphere (or other designated temperatures: 450℃, 500℃, 600℃ and 650℃) with a ramping rate of 2.3 ℃ min^{-1} in a temperature programming electric furnace (HPM-1G, AS ONE) and was kept at that temperature for 4 h and then cooled to room temperature (RT), the emission of ammonia gaseous during polymerization reaction was degassed through post-treatment procedures .The obtained yellow bulks were ground into powder and is denoted as CN-P-T (P stands for precursor acronym of Urea, Dicyandiamide and Melamine, T is the heated temperature, such as CN-M-550 means g-C_3N_4 produced from melamine at 550℃).

2.2.3. Characterization

The crystalline structures of the as-prepared samples were recorded on a powder X-ray diffractometer (XRD, Rigaku, MiniFlex-II, Japan) equipped with

Cu-Kα radiation (λ= 0.15418 nm) at 30 kV accelerating voltage while maintaining the emission current at 15 mA. FTIR spectra were obtained on a JASCO FT/IR 4200 spectrometer with a DR-81 diffuse reflectance attachment. UV–vis diffuse reflectance spectra (DRS) of the samples were obtained by using a spectrometer (Shimadzu, UV-2600) with an integrating sphere accessory (Shimadzu, ISR-240A). BaSO4 was used as a reference and adsorption spectra were calculated from reflectance data using the Kubelka-Munk function. Morphology information was obtained by using a scanning electron microscope (SEM, Jeol, JSM-6701F) and a high-resolution transmission electron microscope (HR-TEM, FEI, Tecnai G^2F30 S-TWIN, 300 KV) equipped with EDX component. N_2 adsorption-desorption isotherms were recorded at 77 K on asurface area analyzer (Quantachrome, Nova 4200e). Specific surface area (S_{BET}) and pore size/volume were calculated from the Brunauer-Emmit-Teller (BET) theory and Barrett-Joyner-Halenda (BJH) theory, respectively. Photoluminescence spectra (PL) of the samples were measured by a Jasco FP-8500 (Japan) spectrofluorometer at an excitation wavelength of 300 nm. Surface chemical states were investigated by X-ray photoelectron spectroscopy (XPS) measurement with a Shimadzu Kratos AXIS-NOVA system by Al Kα radiation and adventitious C1 s peak (284.6 eV) as the reference.

2.2.4. Photocatalytic activity experiment

Before evaluation of the photocatalytic activity, all samples were irradiated with UV light using black light (UVP, XX-15BLB) overnight in order to remove organic contaminants on the surface. Then 0.1 g of a sample was tiled with good uniformity on the bottom of a watch-glass (φ= 26.5 mm). The watch-glass and 125 mL of 500 ppm acetaldehyde/pure air mixture gas were injected into a Tedlar bag (Polyvinyl fluoride, AS ONE Co., Ltd). The bag was kept in a dark room for 2 h to establish the adsorption equilibrium between

samples and acetaldehyde. Then the sample was irradiated by a light-emitting diode (LED, Epitex, L435-30M32L) energy-saving lamp (central wavelength of 435 nm) with light intensity of 3 mW cm^{-2}. The variation in concentration of acetaldehyde and CO_2 evolution were monitored by on-line gas chromatography (Agilent Technologies, 3000A Micro-GC, TCD detector) with OV1 and PLOT-Q columns. The schematic illustration of photocatalytic activity evaluation for CH_3CHO degradation is presented in Figure 19.

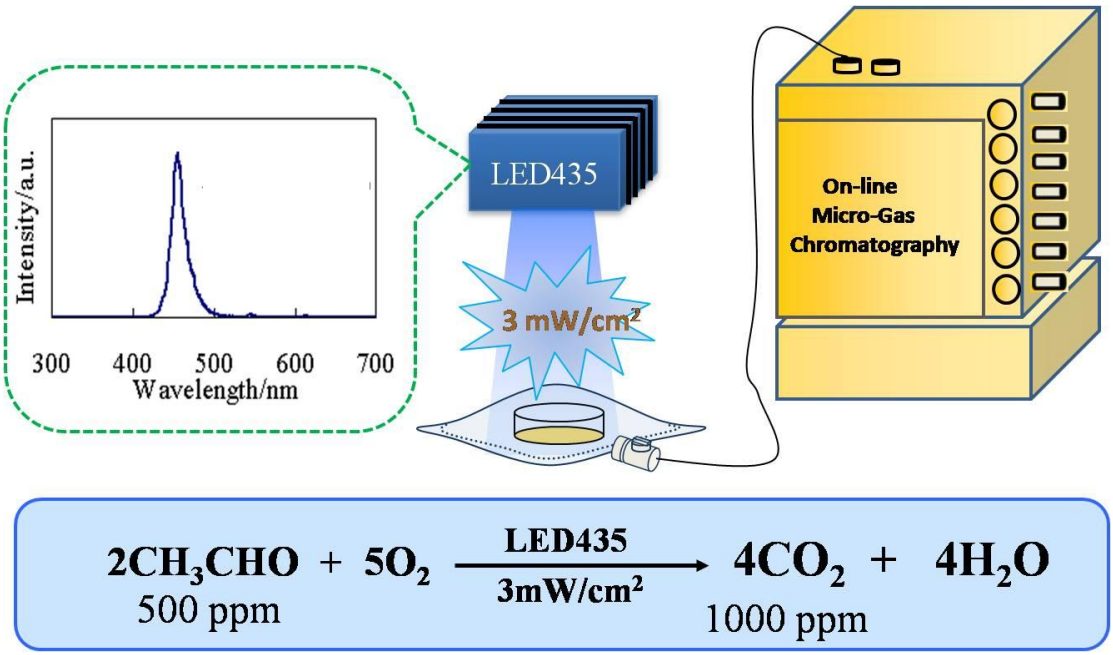

Figure 19 Schematic illustration of photoactivity evaluation

2.3 Results and discussion

2.3.1 Effect of N-rich precursor

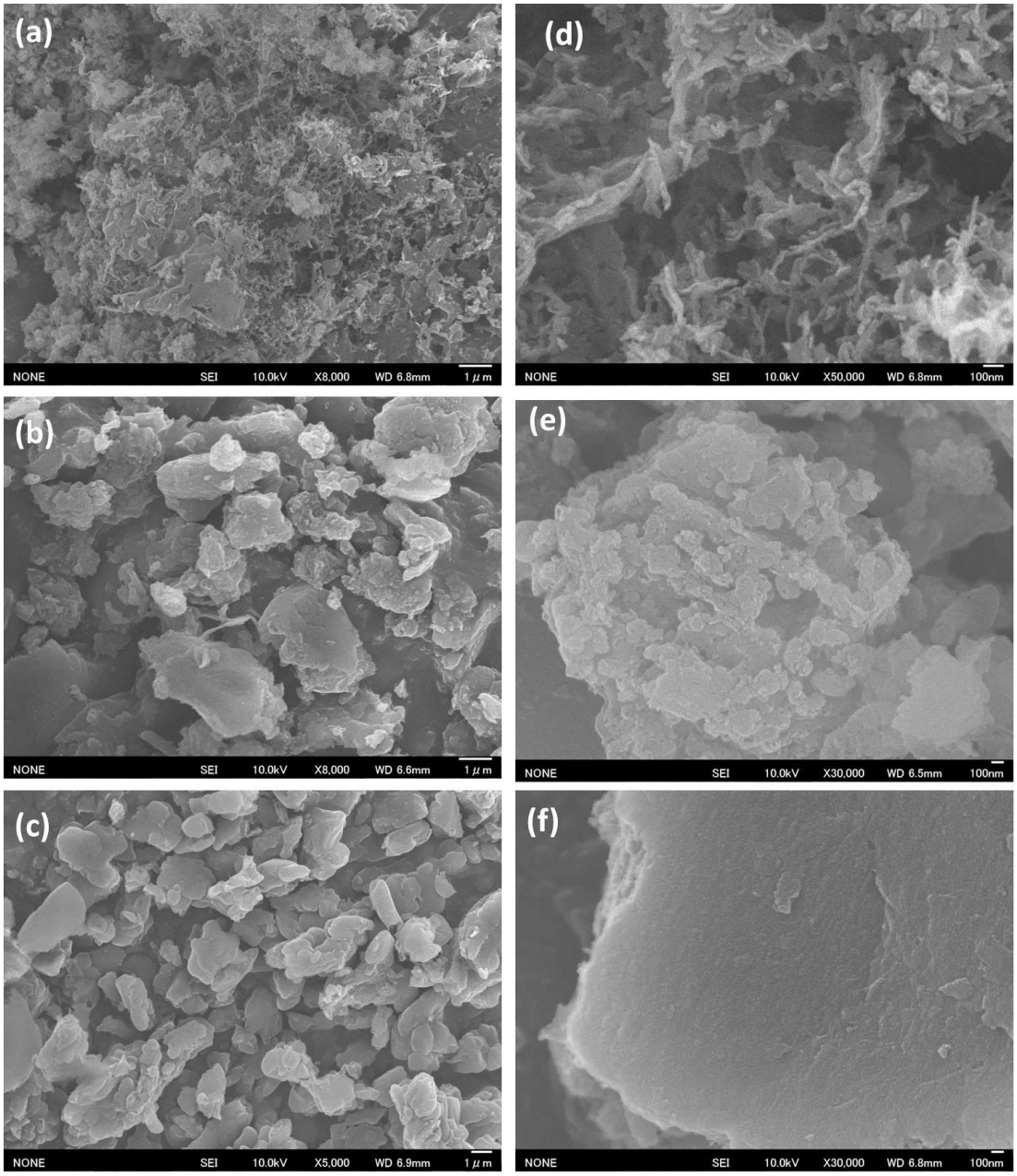

Figure 20 SEM images of g-C_3N_4 bulks prepared by different N-rich precursor. (a,c) CN-U-550; (b,d) CN-D-550 and (c,e) CN-M-550. The scale bars in (a-c) is 1 μm, while in (d-f) is 100 nm.

In this study, three N-rich precursors (urea, dicyandiamide and melamine) were adopted as the starting raw materials to prepare g-C_3N_4 bulks. As shown in Figure 20, the three precursors-derived g-C_3N_4 bulks are with utterly different textural structure and particle size distributions. More detailedly, the urea-derived g-C_3N_4 bulks are composed of curly nanosheets with the thickness of 20 nm, and the nanosheets are also decorated with numerous tiny mesoporous. As to dicyandiamide-derived g-C_3N_4, the bulk-like appearance dominates the polymerization product, the surface of g-C_3N_4 is rough and some particles with a few hundred nanometers grew on it. However, compared with CN-U-550 and CN-D-550, CN-M-550 presents an extremely smooth surface with an enlarged dimensional size (ca. few μm). The distinctly morphology difference can be attributed to the intrinsic properties of precursors, such as content of ammonia groups, degree of polymerization, the route of reaction and so forth. Apart from morphology modulation, different precursors also alter the degree of crystallinity, optical absorption and electric properties of the as-prepared g-C_3N_4 bulks. The structural characterization results were summarized in Figure 21. From XRD patterns, the diffraction peaks at 13.2° and 27.7° can be assigned to (100) and (002), respectively. The crystalline degree of CN-D-550 and CN-M-550 is better than CN-U-550 ones. All the three g-C_3N_4 samples displayed the characteristic absorption peaks of triazine (810 cm^{-1}), CN heterocyclic ring (1200-1800 cm^{-1}) and amino groups in FTIR spectra. From UV-vis, the bandgap of CN-U-550, CN-D-550 and CN-M-550 is 2.72 eV, 2.75 eV and 2.95 eV, respectively. The obviously blue-shift of CN-U-550 is attributed to the famous quantum confinement effect. The PL spectra indicated that CN-M-550 sample is with the fastest rate of photoinduced charge carriers. Urea-derived g-C_3N_4 is with the largest S_{BET} (84 m^2/g) and volume of mesoporous (V_{meso}=0.659 cc/g), with respect to CN-D-550 (S_{BET}=15 m^2/g, V_{meso}=0.115 cc/g) and CN-M-550 (S_{BET}=10 m^2/g, V_{meso}=0.027 cc/g).

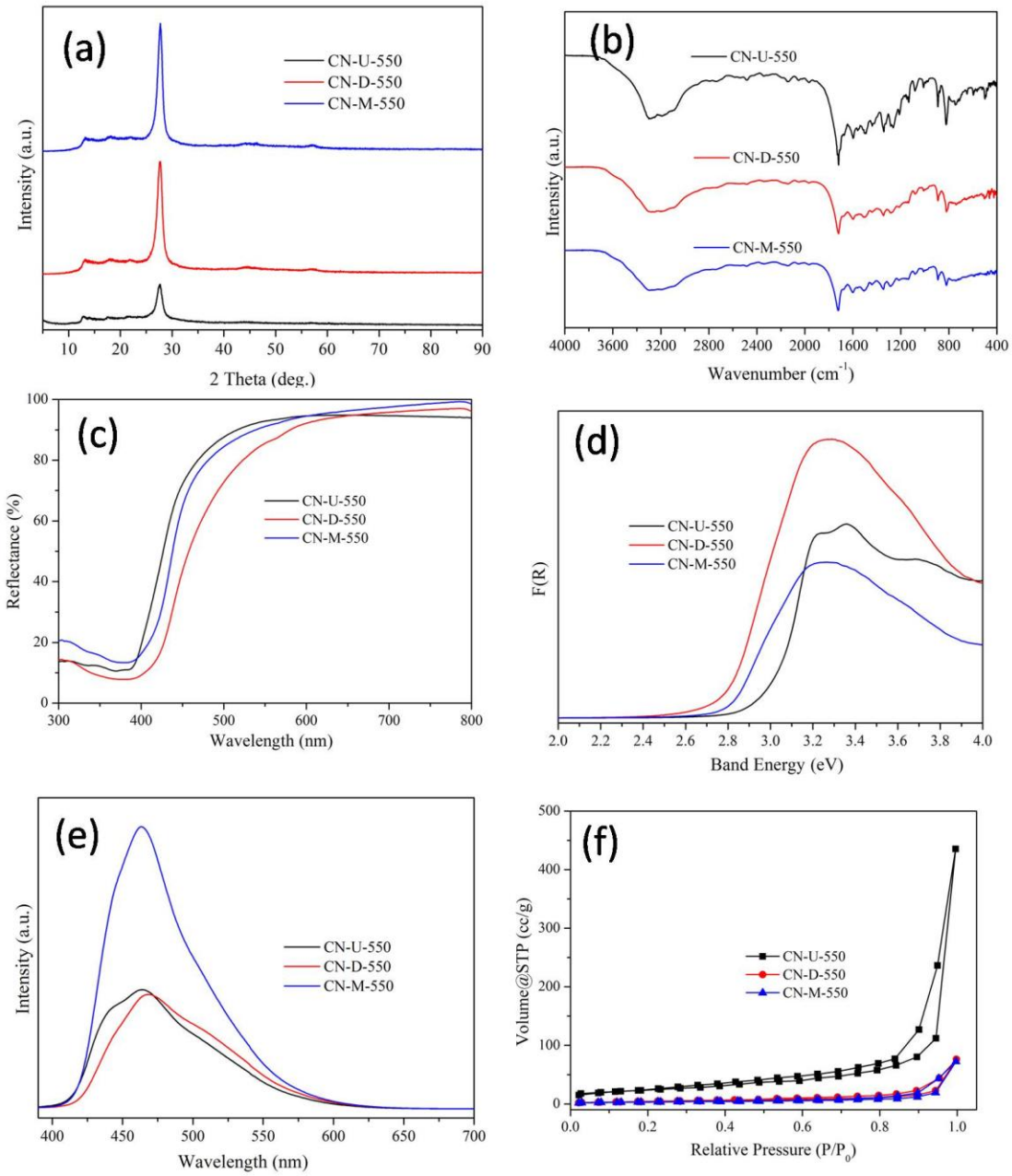

Figure 21 Structural characterizations of g-C_3N_4 bulks prepared from different precursors. (a) XRD patterns; (b) FTIR spectra; (c) Reflectance spectra; (d) Kubelka-Munk transformation; (e) PL spectra (excited at wavelength of 365 nm) and (f) N_2 adsorption-desorption isotherms (measured at 77K).

2.3.2 Effect of polymerization temperature

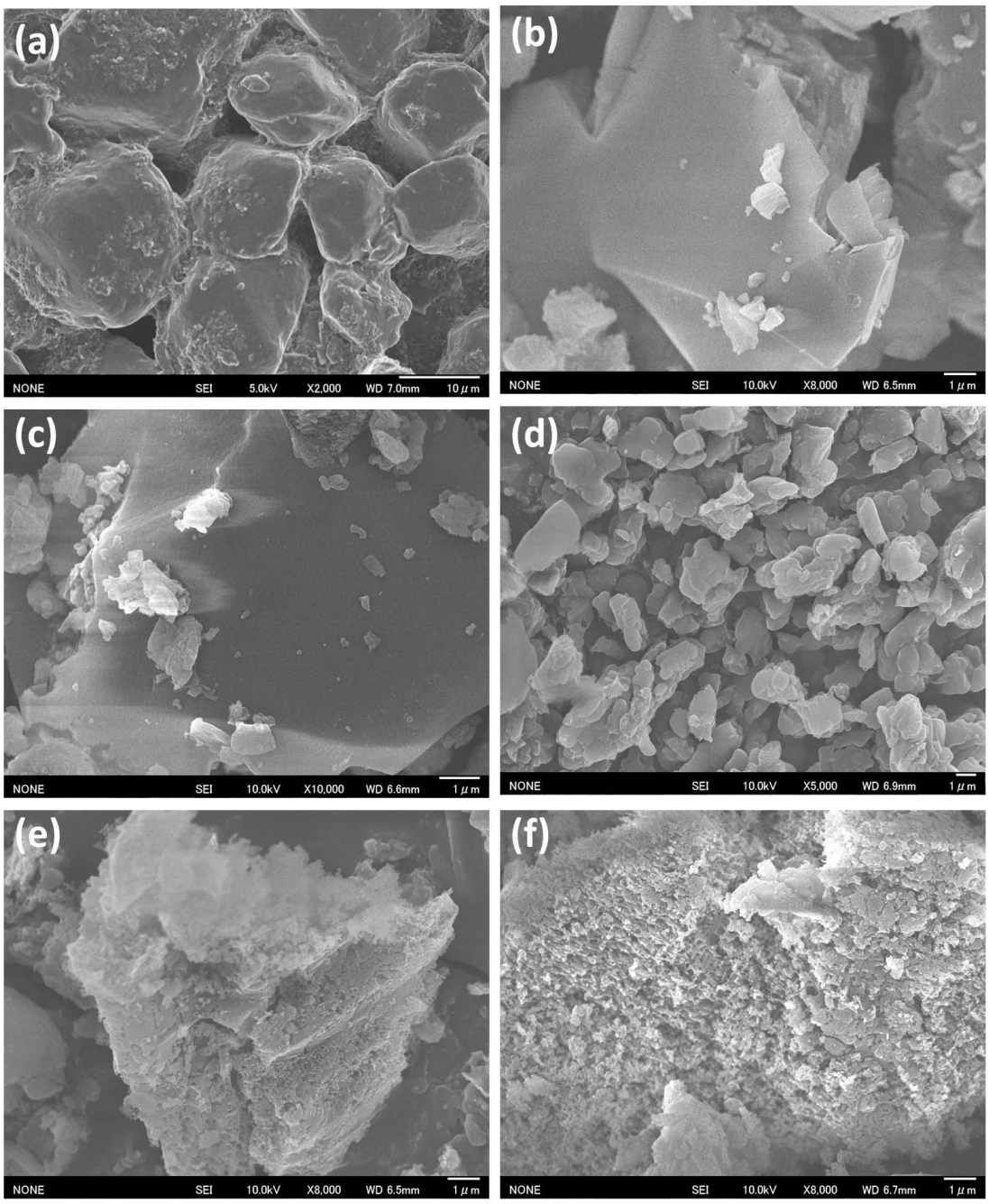

Figure 22 SEM images of g-C_3N_4 bulks prepared at different polymerization temperature. (a) Melamine precursor; (b) CN-M-450, (c) CN-M-500, (d) CN-M-550, (e) CN-M-600 and (f) CN-M-650. The scale bar in (a) is 10 μm, while in (b-f) is 1 μm.

As is known to all, the temperature is a crucial parameter in preparation of various materials. Because the reaction to produce g-C_3N_4 networks is a thermal polymerization process, thus the temperature affects the degree of polymerization of g-C_3N_4 conjugated polymers. In our study, we investigated a wide range of preparation temperature from 450 °C to 650 °C. Herein, take g-C_3N_4 bulks prepared from melamine precursor as an example. As shown in Figure 22, the starting raw material, melamine is an extremely large block with dozens of micrometers. Once the temperature is increased above 345 °C, melamine crystals would sublimate from solid to gaseous phase. The gaseous melamine molecules react quickly to generate melem-related solids in an alumina crucible (with cover). g-C_3N_4 conjugated polymer cannot be formed during the temperature is below 500 °C, which is well verified by XRD and FTIR results in Figure 23(a,b). The diffraction peaks of CN-M-450 can be ascribed to melem oligomers. As presented in Figure 22, g-C_3N_4 bulks with smooth surface were obtained by increasing temperature to 500 °C. If continue to increasing the temperature to 550 °C, smaller g-C_3N_4 bulks would be produced because of crystal growth and ammoxidation effect. Moreover, ammoxidation effect will be further aggravated with hoisting the polymerization temperature to 600 °C and 650 °C. Simultaneously, numerous mesoporous would be introduced to g-C_3N_4 system (Figure 23(f)). By bandgap calcination, the absorption edge (E_g) of CN-M-450 is 440 nm, while the E_g of CN-M-500 and CN-M-550 is 445 nm and 450 nm respectively. The absorption edges of CN-M-600 and CN-M-650 are obviously blue-shift to 435 nm and 415 nm, however, these two samples feature by the presence of medium tail absorption (Urbach tail)[185,186], which is attributed to the formation of midgap states within the band gap. In accordance with UV-vis spectra, the central wavelength of PL emission peaks for as-prepared g-C_3N_4 was also red-shifted at first and then blue-shifted as temperature was increased from 450 °C to 650 °C.

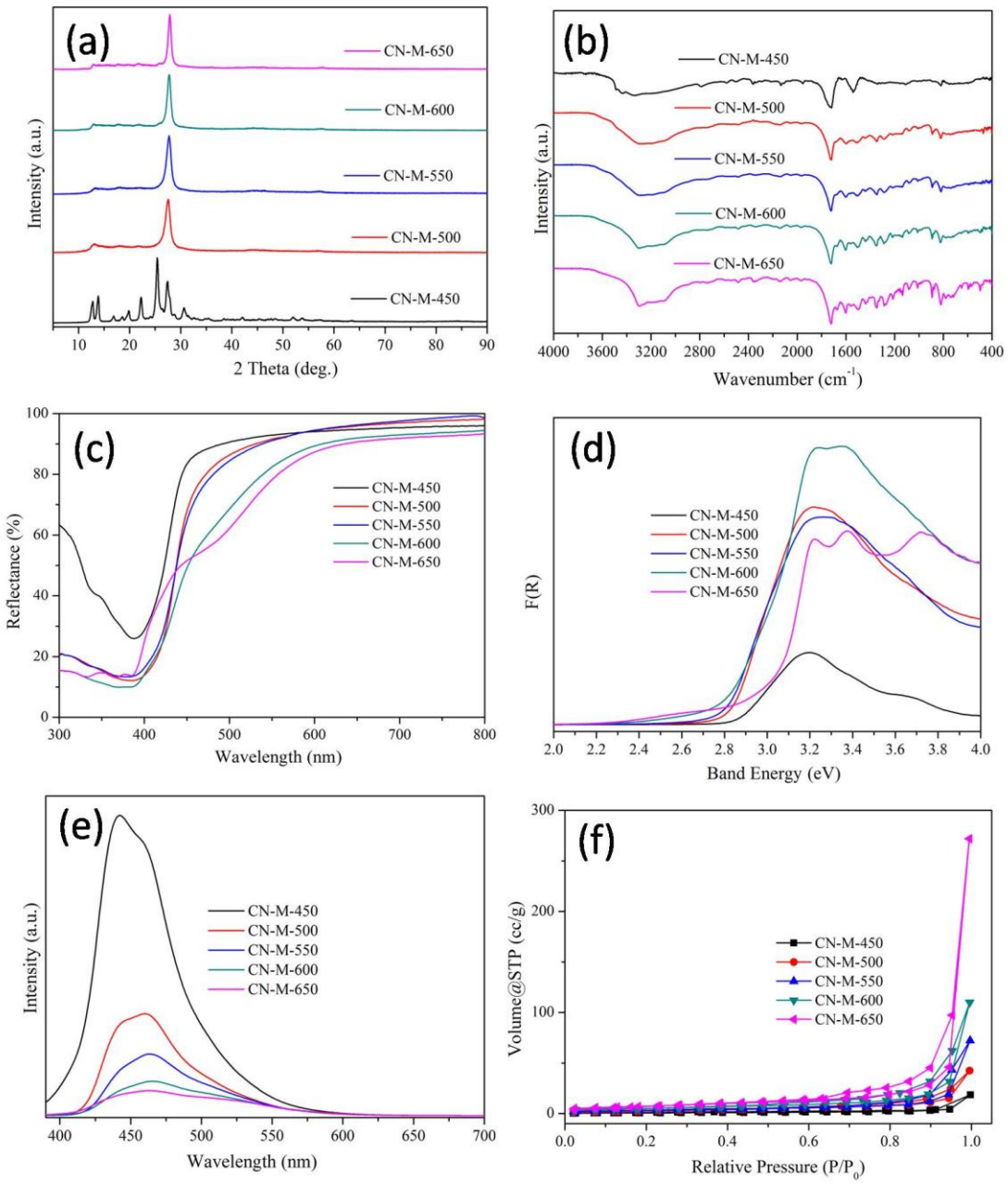

Figure 23 Structural characterizations of g-C_3N_4 bulks prepared at different polymerization temperature. (a) XRD patterns; (b) FTIR spectra; (c) Reflectance spectra; (d) Kubelka-Munk transformation; (e) PL spectra (excited at 365 nm) and (f) N_2 adsorption-desorption isotherms (measured at 77K).

2.4 Photocatalytic activity of pristine g-C_3N_4 bulks

Gaseous CH_3CHO is one of the most toxic volatile organic compounds (VOCs), together with formaldehyde, which widely exists in our daily life. It is usually with higher concentration indoor than outdoors, released from some building materials and some daily consumer products such as cigarettes, adhesives, coatings and inks[187]. Exposed to CH_3CHO atmosphere would irritate the human respiratory system and it has been listed as Group I carcinogens by the International Agency for Research on Cancer (IARC). Acetaldehyde is one of the most frequently found air toxins with cancer risk greater than one in a million[188]. Therefore, it is of great necessity and significantly practical meanings to eliminate CH_3CHO by a green and cost-effective way. Based on this thoughtfulness, we adopted gaseous CH_3CHO as model pollution to evaluate the photocatalytic activity of g-C_3N_4-based photocatalysts. Figure 24 presented the photoactivities of the three g-C_3N_4 bulks. Within 24 h visible light irradiation, CN-M-550 only generated 60 ppm CO_2, while CN-D-550 and CN-U-550 enhanced 2.6 and 3.3 times higher. Thus it still needs further promotion.

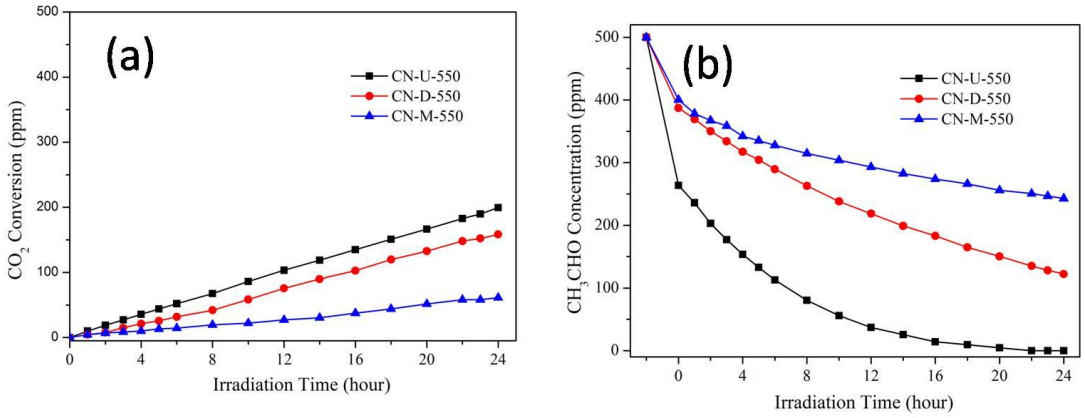

Figure 24 Photocatalytic activities for CH_3CHO degradation under visible light irradiation by various g-C_3N_4 bulks. (a) CO_2 evolution curves; (b) CH_3CHO concentration curves. (Photocatalyst mass: 0.1g, light source: LED 435 nm, light intensity: 3 mW/cm^2, CH_3CHO concentration: 500 ppm)

2.5 Conclusions

In this section, a series of g-C_3N_4 bulks was prepared by altering the N-rich precursor and polymerization temperature. The reaction routine was investigated preliminarily (illustrated in Figure 25). With respect to g-C_3N_4 bulks prepared from melamine and dicyandiamide, urea-drived g-C_3N_4 nanosheets shows much higher specific surface area and mesoporous volume, resulting in superior photocatalytic performance. Besides, the polymerization temperature also plays a vital role in tuning the textrual structure, optical absorption and electric properties, as summarized in Table 1. However, restricting by the small S_{BET} and rapid recombination of photoinduced charge carriers, the photocatalytic activities of g-C_3N_4 bulks (especially to CN-M-550) are still low, which needs further promotion.

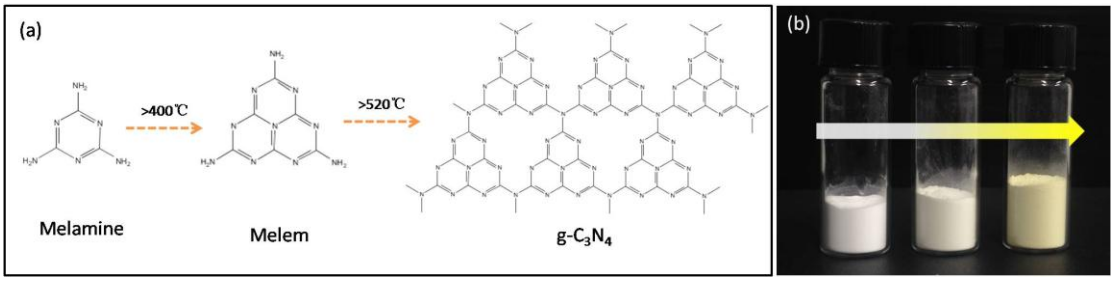

Figure 25 (a) Reaction route from melamine to g-C_3N_4 bulks; (b) Color variation diagram from melamine to melem and g-C_3N_4 bulks.

Table 1 Summary of yield, bandgap, surface area and mesoporous volume for g-C_3N_4 prepared at different N-rich precursors and polymerization temperatures

Items	CN-U-550	CN-D-550	CN-M-450	CN-M-500	CN-M-550	CN-M-600	CN-M-650
Yield (g)	0.65	11.4	16.2	15.1	14.4	11.9	8.8
E_g *(eV)*	2.72	2.95	2.82	2.79	2.75	2.85	2.99
S_{BET} *(m²/g)*	83.8	15.4	2.4	8.9	10.4	18.3	26.5
V_{meso}(cc/g)	0.659	0.115	0.007	0.022	0.027	0.046	0.417

Chapter 3 Morphology engineering of g-C_3N_4 by physicochemical modification

3.1 Introduction

In order to improve the low surface area of g-C_3N_4 bulks, three absolutely different physicochemical modification methods were employed to raise the S_{BET} of g-C_3N_4 as well as to regulate its morphology. It is well known that surface/interfacial properties of a photocatalyst often play a vital role in controlling the involved redox reactions. On the one hand, the higher S_{BET} typically means more reactive sites. However, on the other hand, the higher S_{BET} also implies lower crystallinity. Because the crystallinity of a photocatalyst greatly affects the transfer rate of photogenerated charge carriers from bulk phase to surface reactive sites. For this reason, we should make a tradeoff between surface area and crystallinity to quest for optimal photocatalytic performance. Therefore, elaborated textural modification approaches should be felicitously adopted. In our study, planetary milling, hydrothermal etching and selenium-assisted exfoliation, these three morphology engineering treatment means were utilized to fabricate g-C_3N_4 with special textural structure and enhanced photocatalytic performance. Generally, planetary milling is a cost-effective way to crush bulks into small fragment (even to nanometer size) via mechanical shearing force. And hydrothermal treatment is considered to be a commendable methodology to fabricate high-crystallized inorganic compounds. Moreover, g-C_3N_4 nanorods array (named CN-Rods) was also fabricated by copolymerization melamine and selenium monomers for the first time. With increasing of the pyrolyzation temperature, selenium component could be fully removed. Most importantly, the separation efficiency of photoinduced electrons and holes of g-C_3N_4 could be well promoted simultaneously. The structure-activity relationships of three above physicochemical modified g-C_3N_4 would be further systematically elucidated in results and discussion section.

3.2 Experimental

3.2.1 Materials

All of the reagents were of analytical grade and were used as received. Ethanol (Wako) Assay min 99.5%; Melamine (Wako) Assay min 99.0%; Selenium powder (Sinopharm Chemical) Assay min 99.0%; Acetaldehyde (SIGMA-ALDRICH,) ACS reagent Assay min 99.5%; Pure Carbon Dioxide(Taiyo Nippon Sanso) Assay min 99.995%; Pure Air(Taiyo Nippon Sanso) CO_2<0.1ppm.

3.2.2 Preparation of photocatalysts

CN-Bare photocatalyst: 30 g melamine was heated at 550 ^{0}C for 4 h in electric furnace with ramping rate of 2.3 ^{o}C/min, and then the yellow bulks were ground into powder, denoted as CN-Bare.

CN-PM photocatalyst: The above as-prepared CN-Bare (0.6 g) powders were put into a 50 mL agate bowl containing 50 g yttrium-stabilized zirconia (YSZ) grinding beads (0.6 mm in diameter, Nikkato Co.,). The agate bowl was put on a planetary mill machine (Planetary Micro Mill pulverisette 7, Fritsch Japan Co.,), operating at 750 rpm for 10 min with 3 repetitions. After cooling to RT, the YSZ beads could be moved by screening, and the sample was separated by filtration, washed with deionized water 3 times, and dried in a vacuum drying oven at 60 ^{o}C overnight. The as-prepared sample was denoted as CN-PM.

CN-HT photocatalyst: In a typical synthesis, the above as-prepared CN-Bare (0.6 g), were added to Teflon reaction lined equipped with stainless steel autoclave. After dispersed in ethanol/water mixed solvent for 2 h, the autoclave was transferred to an oven at 160 ^{o}C for 18 h. After cooling, the residue was centrifuged, dried and ground. The obtain product was denoted as CN-HT.

CN-Rods photocatalyst: In a typical synthesis, 10 g melamine together with 1.0 g selenium powder (other addition contents were also adopted: 0.1g, 0.3g and 0.5g) were added to a 100 mL beaker with 50 mL ethanol as solvent. After dispersed and stirred for 1 h, the beaker was transferred to an oven at 80 ^{0}C for 12 h. After cooling, the residue powder was put into an alumina crucible and then heated at 550 $^{\circ}$C for 4 h in electric furnace. Finally, the resultant yellow bulks were ground into powder. For simplification, the obtain products were denoted as CN-Rods.

3.2.3 Characterization

The samples were characterized by XRD, SEM, TEM, BET, FTIR, PL, XPS and UV-vis. The detailed instrument models and relevant parameters refer to the characterization section given in chapter 2.

3.2.4 Photocatalytic activity experiment

In this section, 500 ppm CH_3CHO was still adopted as model pollution to evaluate the photocatalytic performance under visible light irradiation. The evaluation process and parameter setting are same with chapter 2.

3.3 Results and discussion

3.3.1 Textrual and structure characteristic of modified g-C_3N_4

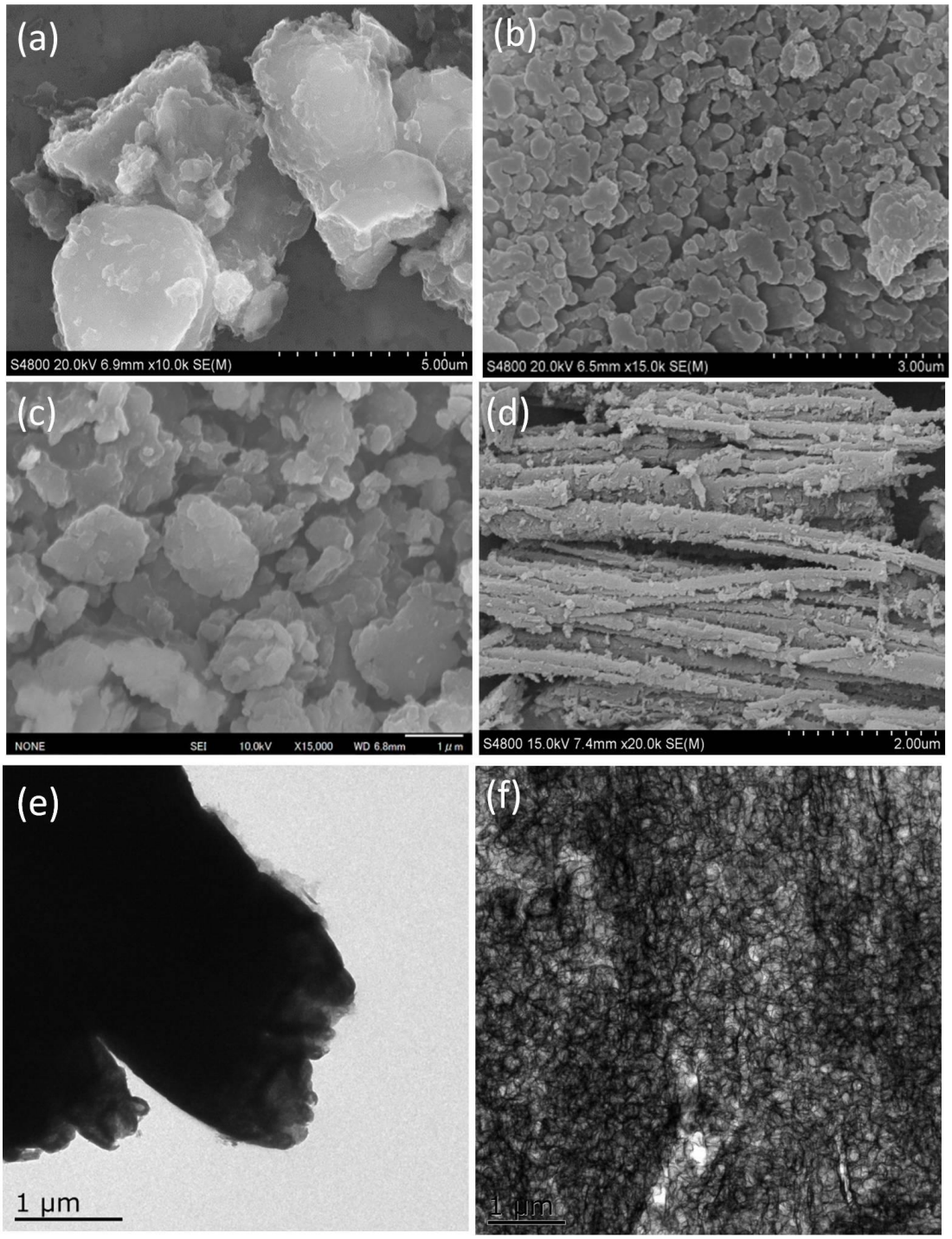

Figure 26 SEM (a-d) and TEM (e-f) images of physicochemical modified g-C_3N_4 photocatalysts. (a, e) CN-Bare, (b) CN-PM, (c) CN-HT, (d, f) CN-Rods.

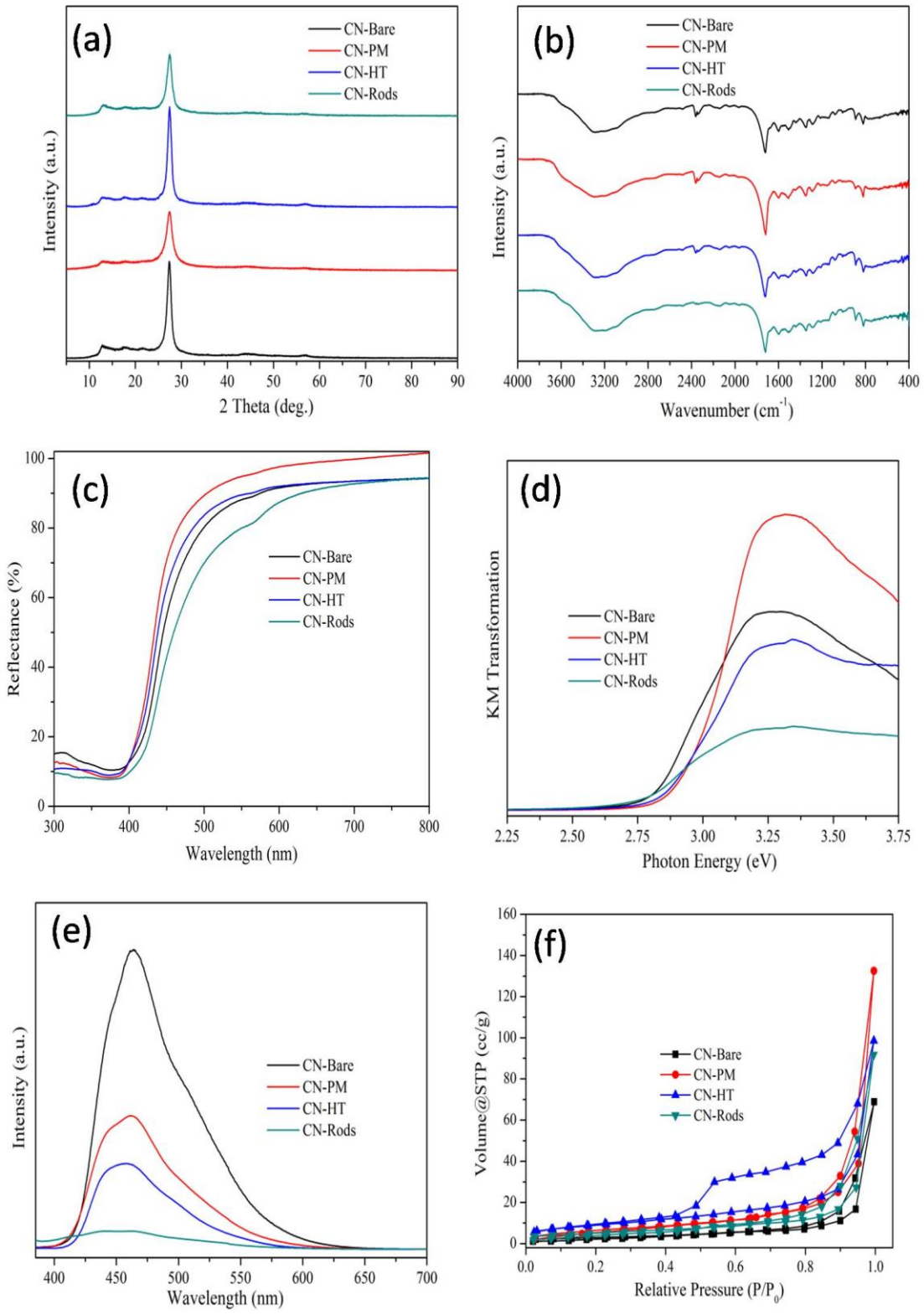

Figure 27 Structural characterizations of physicochemical modified g-C_3N_4 photocatalysts. (a) XRD patterns; (b) FTIR spectra; (c) Reflectance spectra; (d) Kubelka-Munk transformation; (e) PL spectra (excited at 365 nm) and (f) N_2 adsorption-desorption isotherms (measured at 77K).

Figure 26(a-b) indicated the CN-Bare bulks with dozens of micrometers were fully crushed into small lamellar units with a few microns dimension by planetary milling treatment. Nonetheless, such mechanical treatment just endows insignificant impact on the roughness of the surface. Thus, we further attempt a hydrothermal treatment to tailor the surface morphology of g-C_3N_4. Interestingly, nanoparticles and porosity were both successfully introduced onto the surface of g-C_3N_4. And these nanoparticles connected each other to form "sea-island" structure. Such unique structure is vitally beneficial to enlarge the contact areas between reactive substrates and active sites, which is ascribed to the etching effect and hydrolysis of unstable side chains and functional groups in g-C_3N_4. Referring to Figure 26(d, f), g-C_3N_4 prepared from selenium-assisted exfoliation method is with numerous mesoporous and spontaneously (or called self-assembled) nanorods arrays were formed. The CN-Rods are also with long aspect ratio (>25). From the characterization results of XRD and FTIR in Figure 27(a-b), it can be confirmed that the three modified g-C_3N_4 samples resemble the structure of CN-Bare, indicating that the main C-N network are well maintained. However, the optical absorption, specific surface area, porous volume and separation of charge carriers were altered obviously (given in Figure 27(c-f)). The slight blue-shift of optical absorption after physicochemical treatment for CN-PM and CN-HT is attributed to quantum confinement effect. The red-shift of CN-Rods may derive from the multilevel scattering absorption effect by the distinctive cellular structure on g-C_3N_4 rods (Figure 26(f)). With respect to the isotherm curve of CN-Bare, CN-HT shows much more mesoporous and higher S_{BET}, because hydrothermal treatment is very beneficial to remove the unstable zone from the surface of g-C_3N_4 bulks. From PL spectra, it can be inferred that the recombination rate of charge carriers are improved greatly by comparison with CN-Bare counterpart. Moreover, CN-Rods present the best separation efficiency among them.

3.3.2 Effect of selenium contents on CN-Rods

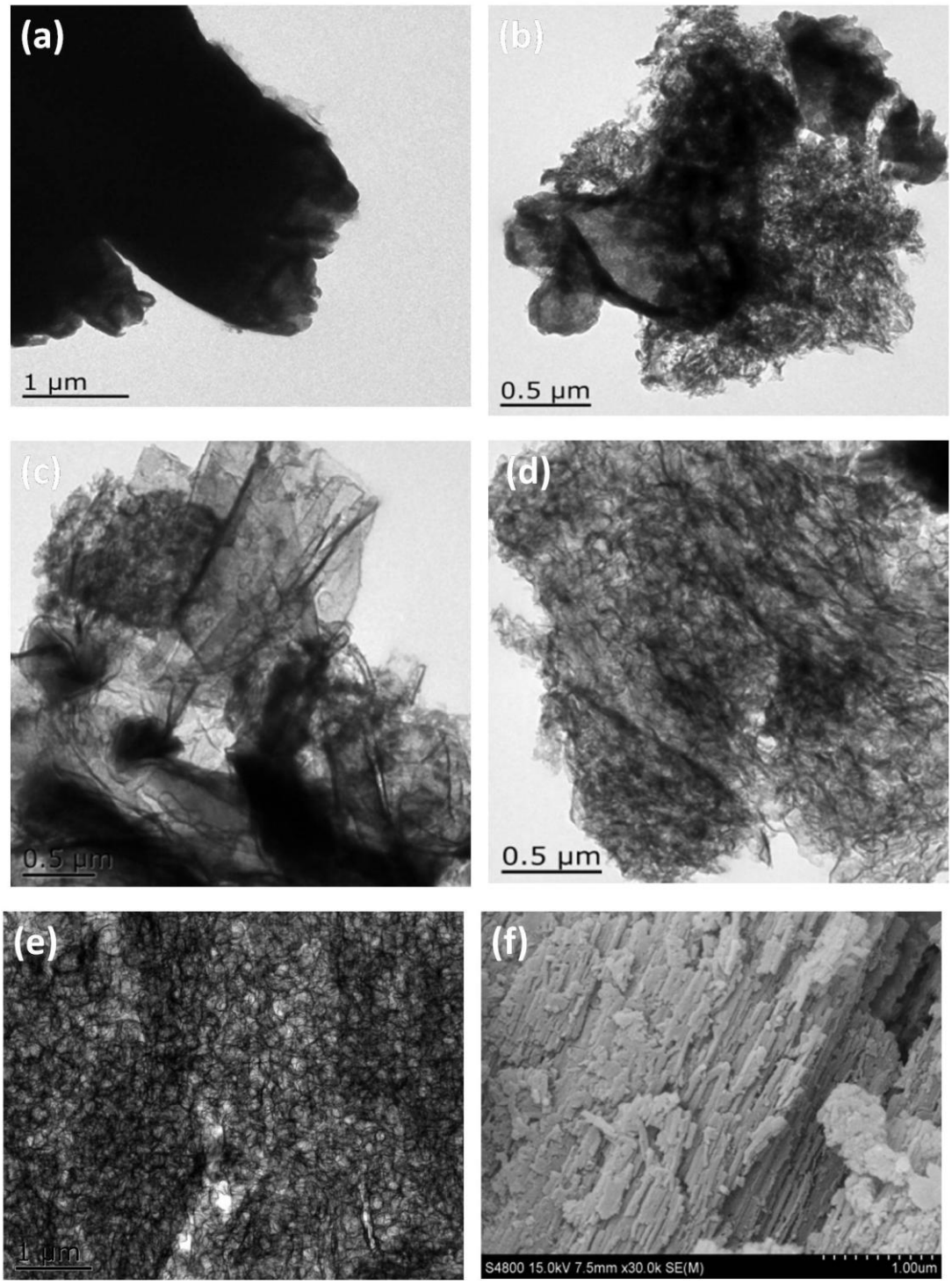

Figure 28 TEM and SEM images of g-C_3N_4 photocatalysts exfoliated with different contents of selenium. (a) CN-Bare; (b) CN-1Se; (c) CN-3Se; (d) CN-5Se; (e-f) CN-10Se (also denoted as CN-Rods).

The morphology results of as-prepared Se-modified g-C_3N_4 were shown above. Figure 28 (a) indicated that g-C_3N_4 prepared without copolymerizing with Se monomer displayed numerous sheets-stacked bulks with an extremely smooth surface. When 1wt% selenium powder was introduced into the melamine substrates, the generated g-C_3N_4 2D sheets were partially crushed attributed to the preferential combination between melamine molecule and Se monomer. By this way, the Van der Waals's interaction force of interlamination can be weakened tremendously, which was proved by the low-angle shift of (002) diffraction peak. It is worth to noting that with increasing the addition content of Se co-polymerization component, the degree of fragmentation is much more obvious, even g-C_3N_4 nanosheets with a few nanometers thickness could be obtained locally, as TEM images shown in Figure 28 (b-e). Besides, the generated wrinkles on g-C_3N_4 surface can not only provide much more active sites for redox reaction (as well as larger specific surface area for substrate molecules adsorption), but also beneficial to separate photogenerated electrons and holes (a shorter e^-/h^+ diffusion and transfer distance than bulk material). Intuitively, we can observe a hackly surface from SEM image of Figure 28(f). Meanwhile, the hackly surface is made up of numerous nanorod arrays. The appearance of this unique hierarchical structure was ascribed to the orientation attachment of melamine molecules assisted by the coordination effect between $-NH_2$ groups and Se molecules. Meanwhile, with increasing the pyrolyzation temperature to 550 $^{\circ}C$, selenium component could be fully removed (verified by EDS and XPS). Under this condition, g-C_3N_4 nanorods array, even nanosheets with numerous mesoporous structure could be obtained successfully. However, it still needs more evidence and further experiment to support this orientation attachment hypothesis.

3.4 Photocatalytic activity of morphology modified g-C_3N_4

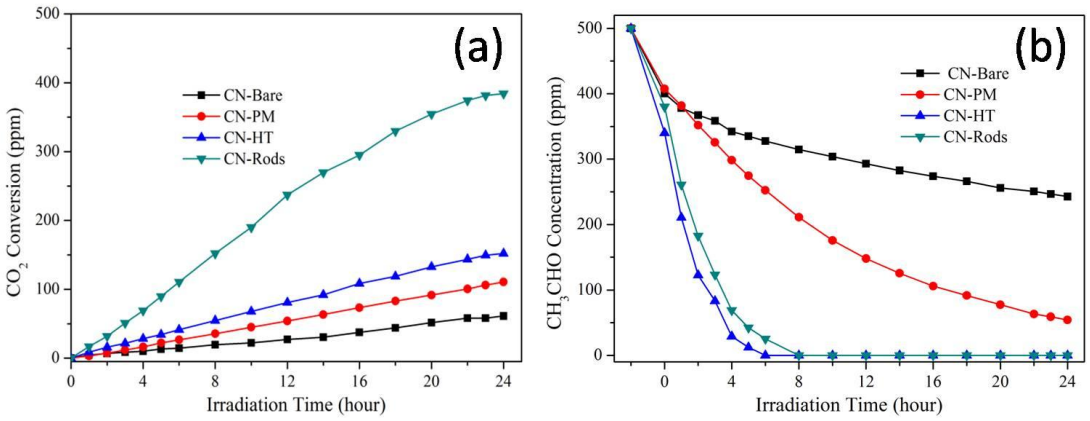

Figure 29 Photocatalytic activities for CH_3CHO degradation under visible light irradiation by various modified g-C_3N_4 photocatalysts. (a) CO_2 evolution curves; (b) CH_3CHO concentration curves. (Photocatalyst mass: 0.1g, light source: LED 435 nm, light intensity: 3 mW/cm^2, CH_3CHO concentration: 500 ppm)

Figure 29 showed the photocatalytic activities for various modified g-C_3N_4 photocatalysts. By planetary milling treatment, hydrothermal etching and selenium-assisted exfoliation, the photocatalytic activities were enhanced 1.8, 2.5 and 6.3 times up than CN-Bare without any treatment. The reasons of photocatalytic activity enhancement were elucidated as following: (1) CN-Rods provide much more absorption and reaction active sites. (2) CN-Rods possess much smaller size and lower dimensionality, which is greatly beneficial for photogenerated charge carriers to separate and then transfer to the surface to participate in CH_3CHO photooxidation reaction. From PL spectra, it can also be inferred that the recombination rate of charge carriers are improved greatly by comparison with CN-Bare counterpart, in accordance with the highest photooxidation performance. (3) The optical absorption capacity is strengthened by multilevel diffractive of the cellular structure on g-C_3N_4 nanorods. Therefore, the photocatalytic performance was facilitated by the above-mentioned synergistic effect.

3.5 Conclusions

Via morphology engineering approaches, three types of physicochemical modified g-C_3N_4 photocatalysts were successfully fabricated (as summarized in Figure 30). By planetary milling treatment, hydrothermal etching and selenium-assisted exfoliation, the photocatalytic activities of modified g-C_3N_4 were enhanced 1.8, 2.5 and 6.3 times, respectively. For the first time, elemental selenium, as a good structural-directing agent, efficiently stimulates the formation of rod-like g-C_3N_4 with numerous cellular in this study. Such specific morphology is extremely beneficial to separate and transfer the photoinduced charge carries. Obviously, selenium-assisted exfoliation would be a cost-effective way to tailor the morphology of g-C_3N_4 with outstanding photocatalytic performance.

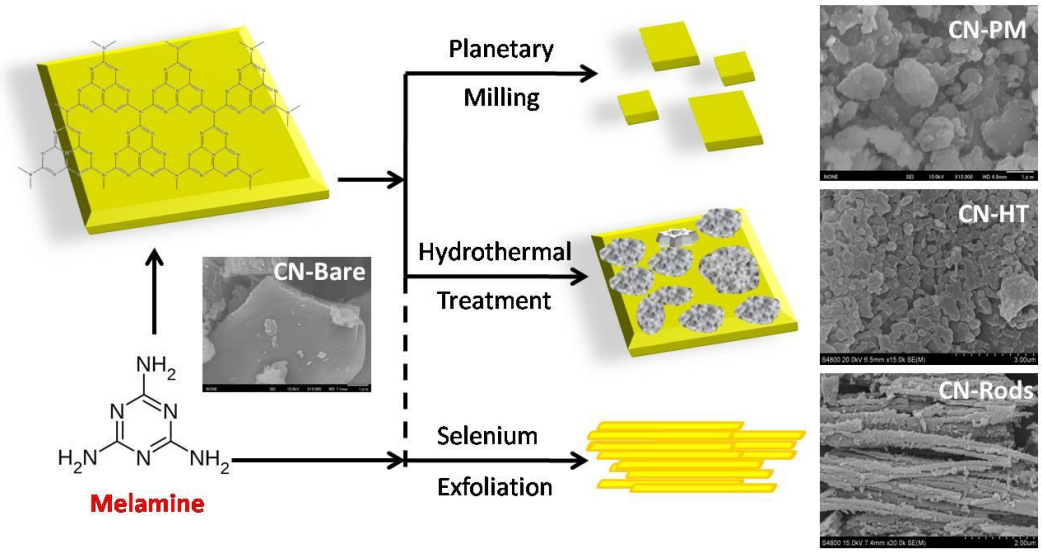

Figure 30 Schematic of physicochemical modified g-C_3N_4 photocatalysts prepared by morphology engineering approaches.

Chapter 4 Extended visible light absorption of g-C_3N_4 by bandgap engineering

4.1 Introduction

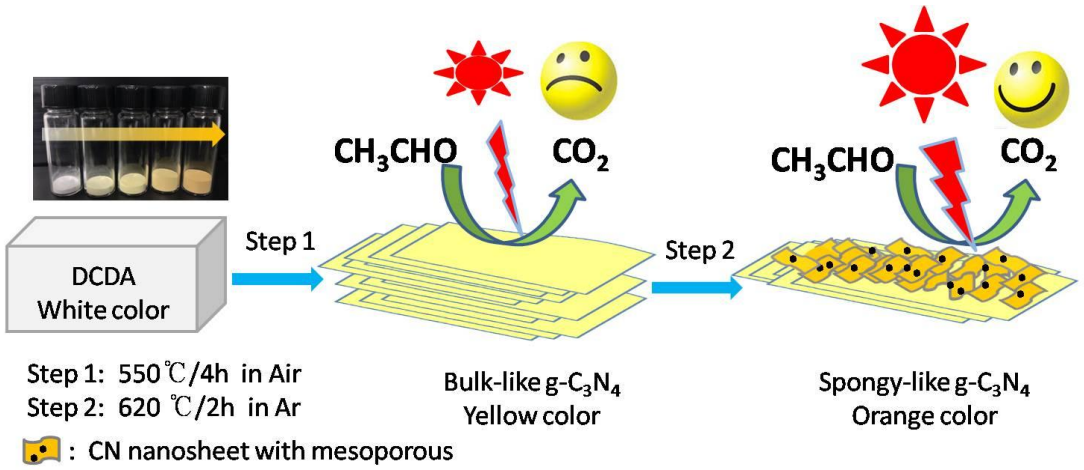

Figure 31 Schematic illustration of extended visible-light-responsive g-C_3N_4

Apart from investigating the effect of morphology engineering on photocatalytic activity, the optical absorption ability of g-C_3N_4 was also tuned in our study. Because the CN-Bare photocatalyst possesses a medium bandgap (ca.2.7eV), indicating that it can only utilize the photons with wavelength smaller than 460nm, while the visible light accounts for 50% of the whole solar spectrum. As discussed in 2.4 section, g-C_3N_4 bulks prepared by conventional one step thermal treatment show extremely weak CH_3CHO photooxidation activity under visible light irradiation. Therefore, feasible measurements should be taken to surmount this barrier. In this study, two-steps thermal treatment strategy was adopted to extend the visible-light absorption (as schematic illustrated in Figure 31). A spongy-like g-C_3N_4 with highly extended visible-light-responsive capacity was prepared by two-steps thermal treatment (denoted as CN-Spy), and optical absorption edge of CN-Spy was expanded from 460nm to 650 nm. Meanwhile, the photocatalytic performance for CH_3CHO degradation was also promoted.

4.2 Experimental

4.2.1 Materials

Dicyandiamide (Wako) Assay min 90.0%; Acetaldehyde (SIGMA-ALDRICH,) ACS reagent Assay min 99.5%; Pure Carbon Dioxide (Taiyo Nippon Sanso) Assay min 99.995%; Pure Air (Taiyo Nippon Sanso) CO_2<0.1ppm, Nitrogen and Argon (Taiyo Nippon Sanso).

4.2.2 Preparation of photocatalysts

Step 1: 6 g Melamine was put into a 100 mL alumina crucible and then heated at 500 ^{o}C for 4 h in static air in the electric furnace, the ramping rate was kept at 2 ^{o}C·min^{-1}, the sample was cooled to room temperature and the yellow products were denoted as CN-500Air.

Step 2: The resultant CN-500Air powder from step 1 was heated at 620 ^{o}C (550/600/650 ^{o}C) for 2 h in an alumina crucible in an argon (nitrogen/air) atmosphere with a flow rate of 50 mL·min^{-1}, the ramping rate was kept at 2 ^{o}C /min (5 or 10 ^{o}C /min), the as-prepared bulk was ground into powder. For simplification, it was denoted as CN-500Air-620Ar.

4.2.3 Characterization

The samples were characterized by XRD, SEM, BET, FTIR, PL and UV-vis. The detailed instrument models and relevant parameters refer to the characterization section given in chapter 2.

4.2.4 Photocatalytic activity experiment

In this section, 500 ppm CH_3CHO was still adopted as model pollution to evaluate the photocatalytic performance under visible light irradiation. The evaluation process and parameter setting are same with chapter 2.

4.3 Results and discussion

4.3.1 Morphology characterization of two-steps thermal treated g-C_3N_4

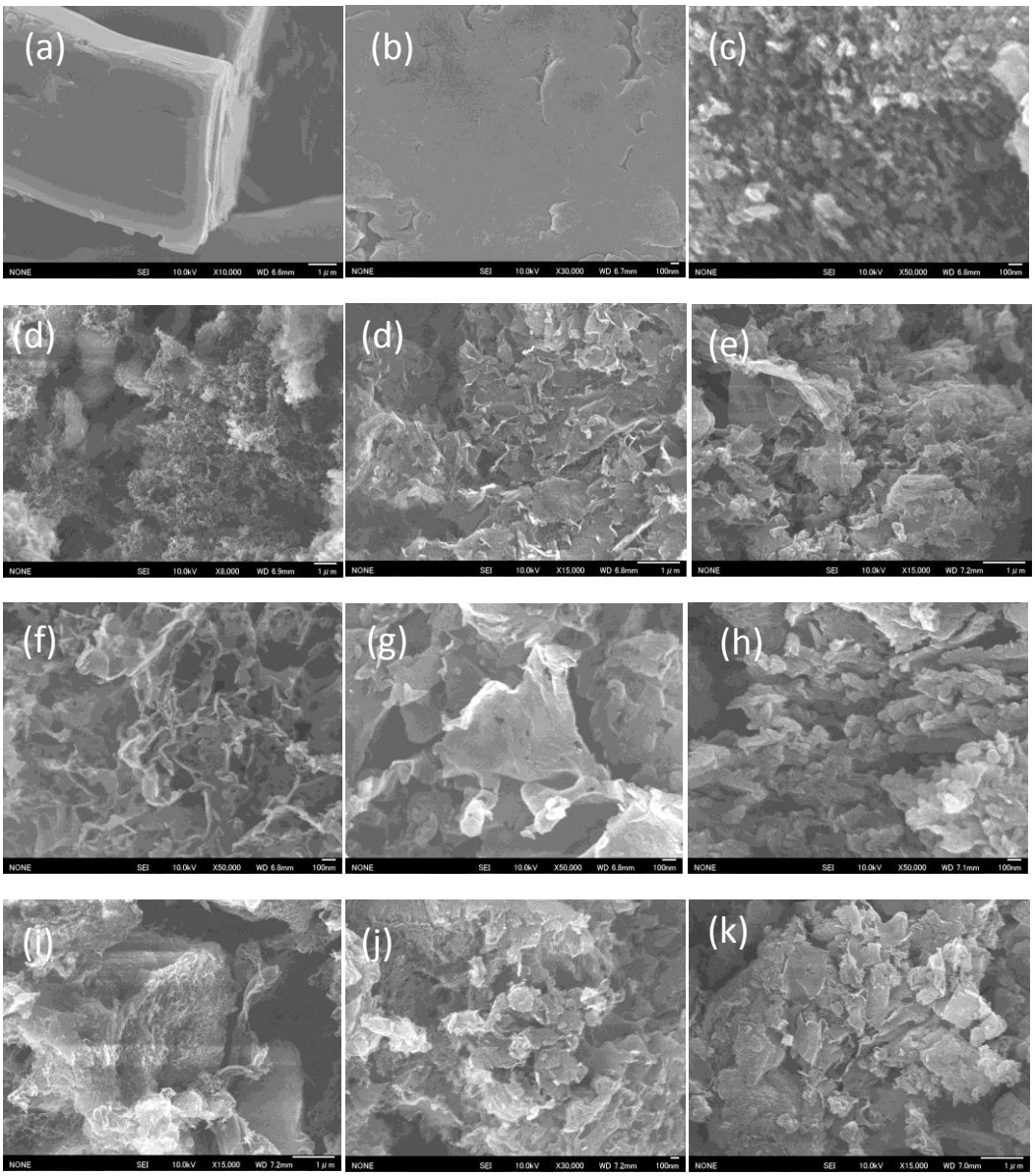

Figure 32 SEM images of CN prepared at different conditions. (a) DCDA precursor; (b) CN-500Air; (c) CN-500Air-620Ar With Cover; (d, f) CN-500Air-620Ar Without Cover; (e, g) CN-500Air-620Ar 5 ^{o}C/min; (f, h) CN-500Air-620Ar 10 ^{o}C /min; (i, j) CN-500Air-600Ar; (k) CN-500Air-550Ar;

The morphology of as-prepared graphitic carbon nitrides at different conditions is shown above. Figure 32 (a) shows the morphology information of DCDA precursor, it presents bulk-like texture structure with tens of microns size. Figure 32(b) indicated that CN-500Air prepared without two-step thermal treatment displayed numerous sheets-stacked bulks with an extremely smooth surface. By observation of SEM images in Figure 32(c-k), in which two-steps thermal treatment was introduced, the generated CN 2D sheets were partially crushed, which is attributed to the secondary ammonia gases evolution from incomplete condensation of CN-500Air. By this way, the Van der Waals's interaction force of interlamination can be weakened tremendously. It is worth to noting that with increasing the two-step thermal treatment temperature or decreasing the temperature ramping rate, the degree of fragmentation is much more obvious, even g-C_3N_4 nanosheets with a few nanometers thickness as well as mesoporous could be obtained locally, as shown in Figure 32(c-k). Besides, the generated wrinkles on g-C_3N_4 surface can not only provide much more active sites for redox reaction (as well as larger specific surface area for substrate molecules adsorption), but also beneficial to separate photogenerated electrons and holes (a shorter e^-/h^+ diffusion and transfer distance than bulk material). Intuitively, we can observe a spongy surface from SEM image of Figure 32(d, f). Meanwhile, the spongy surface is made up of numerous CN nanosheets and nano-porous, the appearance of this unique hierarchical structure was ascribed to the fully removal of $-NH_2$ groups on CN surface.

4.3.2 Effect of crucible cover in two-steps thermal treatment

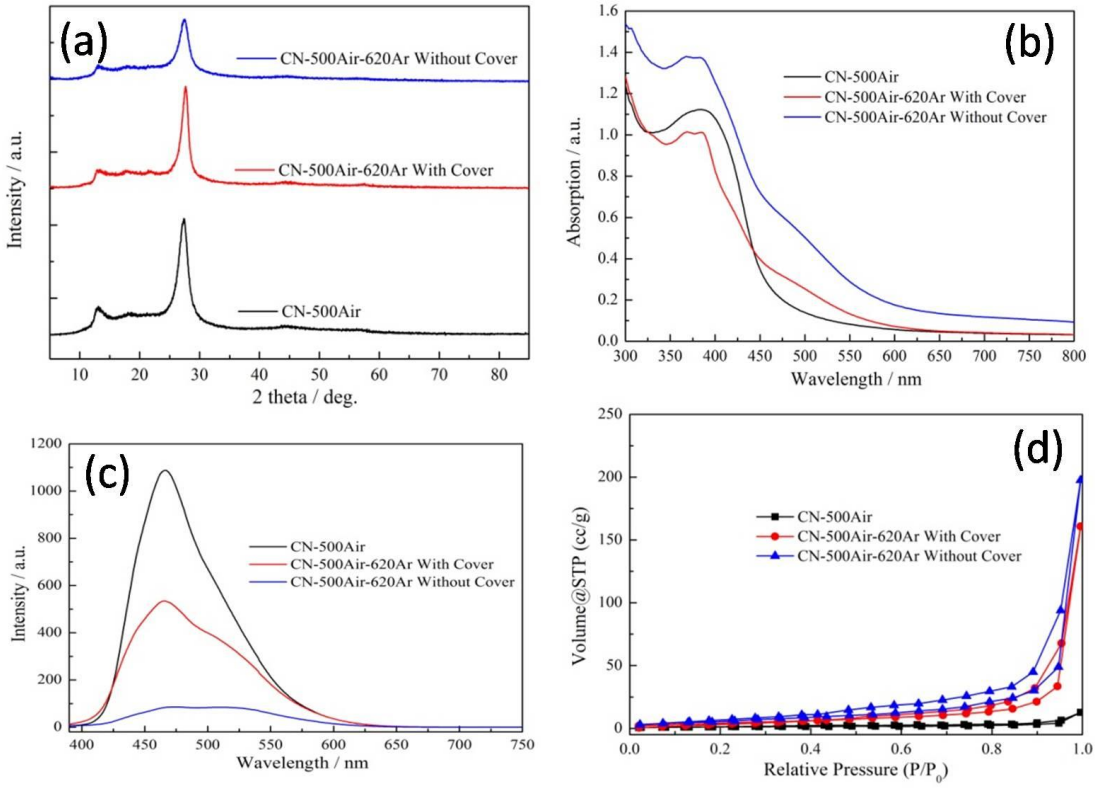

Figure 33 Structure characterization of CN. (a)XRD; (b)UV-vis; (d)PL; (c)BET.

Figure 33 showed various measurement results to probe its structure information of as-prepared g-C_3N_4. From XRD patterns (Figure 33(a)), it indicated that with introducing two-step thermal treatment, the intensity of (100) and (002) crystal planes were both weakened greatly, which may mean that some amorphous CN polymers formed on its surface. And its visible light absorption was also enhanced greatly with absorption edge shifting from 460 nm to 650 nm (Figure 33(b)). Moreover, from PL spectra, we can draw the conclusion that two-step thermal treatment, especially without crucible cover could greatly promote the photogenerated holes and electrons separation. Meanwhile, CN polymeric photocatalyst with a higher specific surface area (S_{BET}= 23.2 m^2/g) can be achieved, nearly 6 times enlarged than that of CN-500Air (S_{BET}=4.3 m^2/g), as shown in Figure 33 (d).

4.3.3 Effect of temperature ramping rate in two-steps thermal treatment

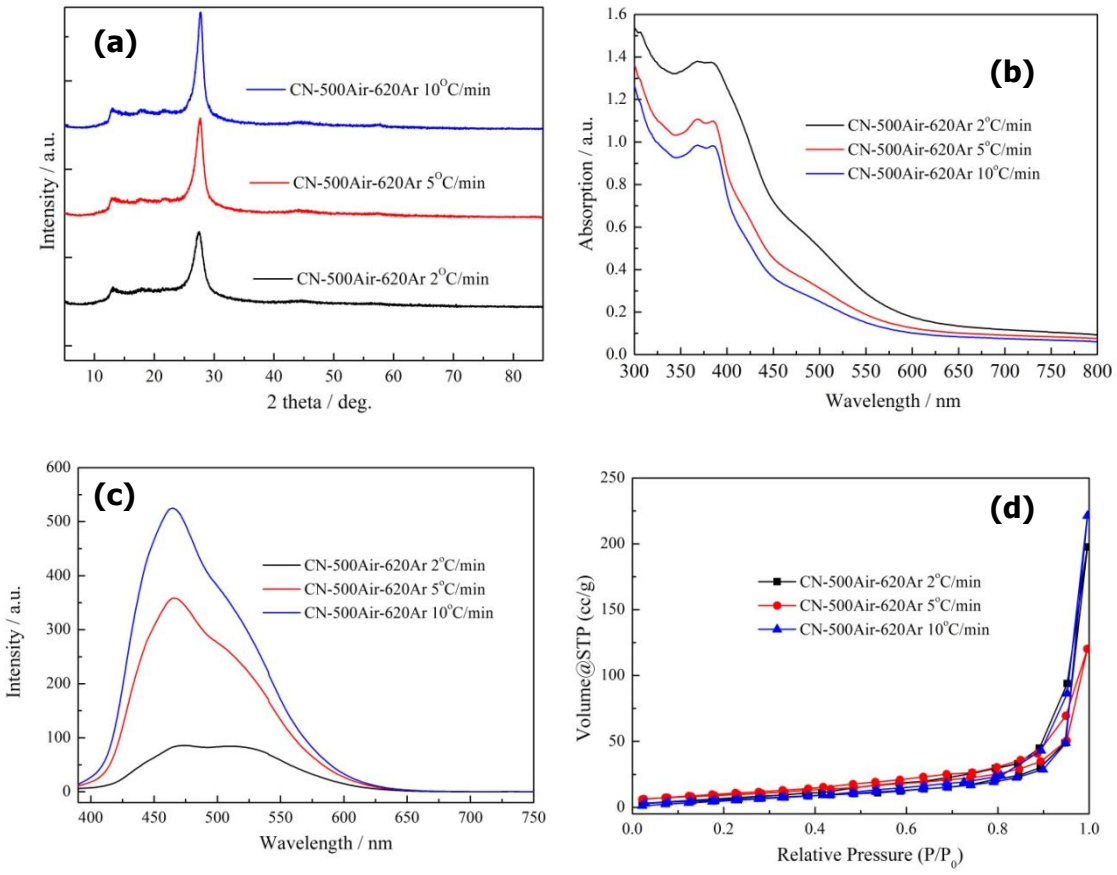

Figure 34 Structure characterization of CN. (a)XRD; (b)UV-vis; (d)PL; (c)BET.

From Figure 34(a-c), it can infer that the slower temperature ramping rate is, the longer extended visible-light-responsive range can be obtained. Simultaneously, it also beneficial to achieving a better separation efficiency of photogenerated holes and electrons, which can be ascribed to a slow temperature ramping rate often means a big probability for fully condensation. Namely, it means CN polymer photocatalyst with less defects can be prepared by controlling the temperature ramping rate in a two-step thermal treatment.

4.3.4 Effect of adopted temperature in two-steps thermal treatment

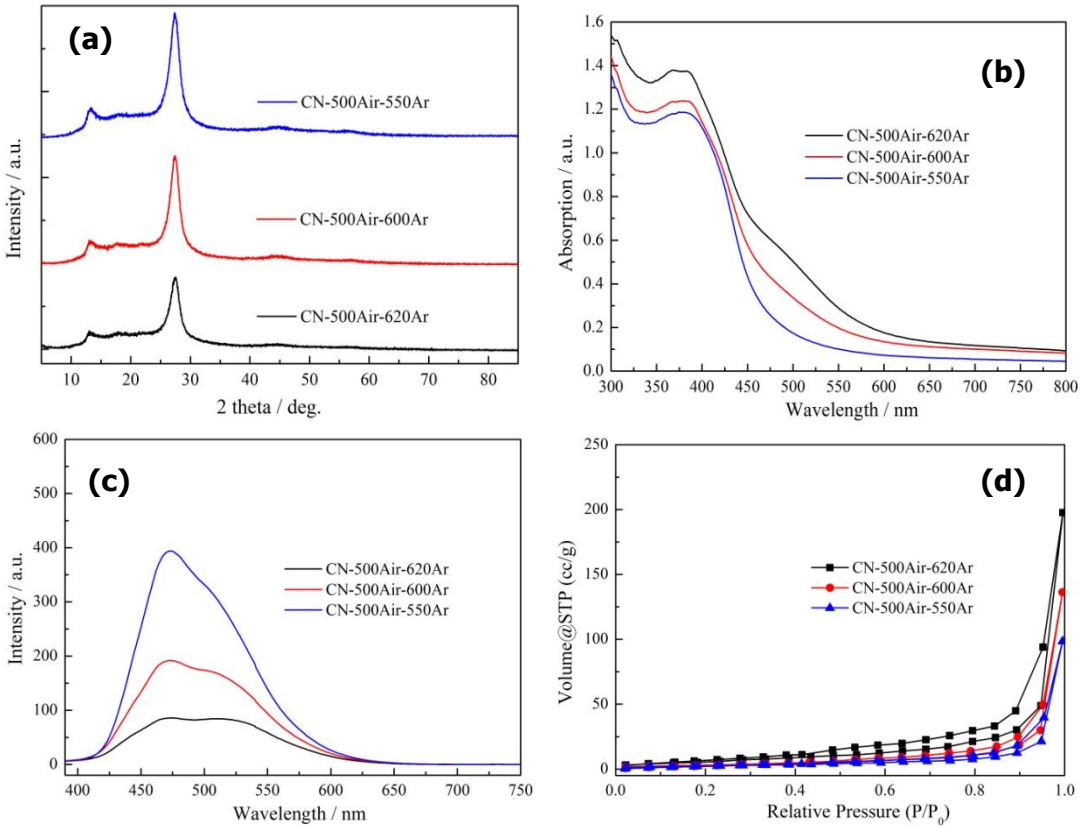

Figure 35 Structure characterization of CN. (a)XRD; (b)UV-vis; (d)PL; (c)BET

The structure of graphitic carbon nitride with a two-step treatment approach was characterized by various measurements such as XRD, UV-vis, PL and BET. As is known to all, the thermal treatment temperature plays a vital role in photocatalyst preparation and greatly affects the photocatalytic performance. From XRD patterns in Figure 35(a), the crystalline intensity of (002) and (100) planes were both greatly weakened when the thermal treatment temperature was increased from 550 °C to 620 °C, which indicated that some amorphous CN polymer may be formed on the surface of its parent. Meanwhile, numerous mesoporous were introduced into CN bulks with the temperature increasing, which can be obtained from Figure 35(d), the specific surface area and meso-porous volume are 9.6 m^2/g, 12.4 m^2/g, 23.2 m^2/g and 0.033cc/g, 0.046cc/g, 0.075cc/g for 550 °C, 600 °C, 620 °C, respectively. Any

products could be obtained when the thermal treatment temperature was above 650 °C. Moreover, from Figure 35(b), it indicated that the visible-light absorption ability of CN photocatalyst can also be tuned by altering the thermal treatment temperature. The absorption edge of CN can be extended from 460nm to 650 nm, which reflects the significance of surface modification by this two-step thermal treatment. Most importantly, the photogenerated charge carriers' recombination can also be greatly restrained by this approach, because the PL intensity was weakened 4 times after increasing the temperature from 550 °C to 620 °C, as shown in Figure 35(c).

4.4 The photocatalytic activity of two-steps thermal treated g-C_3N_4

4.4.3 Activity evaluation of CN with/without Cover

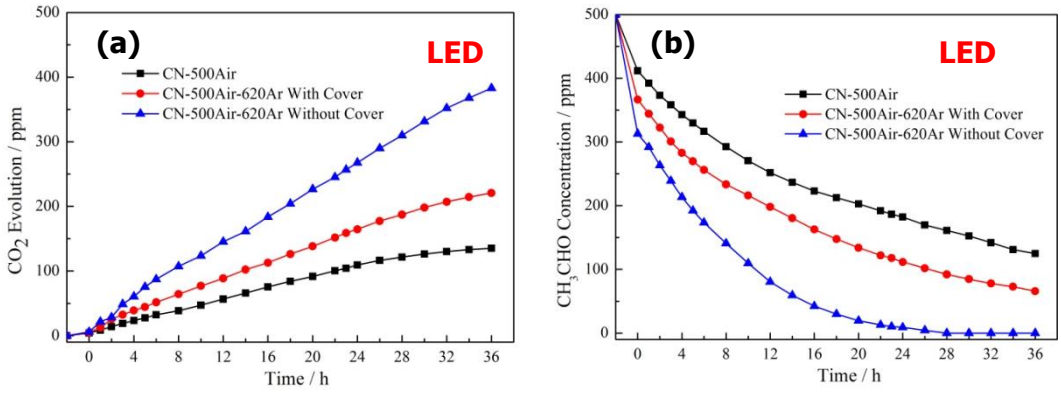

Figure 36 Photocatalytic activity evaluation of CN photocatalysts under visible light irradiation. (a) CO_2 evolution, (b) CH_3CHO concentration variation.

Under the irradiation of 435 nm monochromatic light, the CN photocatalyst prepared without cover during two-step thermal treatment showed about 3 times higher activity enhancement than that of CN-500Air, it also presented

1.73 times higher than CN fabricated with cover (Figure 36). The activity enhancement is attributed to the extended visible-light-responsive ability and larger specific surface area, changing from 4.3 m^2/g (CN-500Air) to 23.2 m^2/g (CN-500Air-620Ar without cover). Typically, the larger of S_{BET} means the more adsorption and reaction active sites, further proved by CH_3CHO concentration variation curves in Figure 36(b).The CN with larger S_{BET} can fully adsorb 500 ppm CH_3CHO within 24 h while CN-500Air takes more than 36 h.

4.4.2 Activity evaluation of CN with different ramping rates

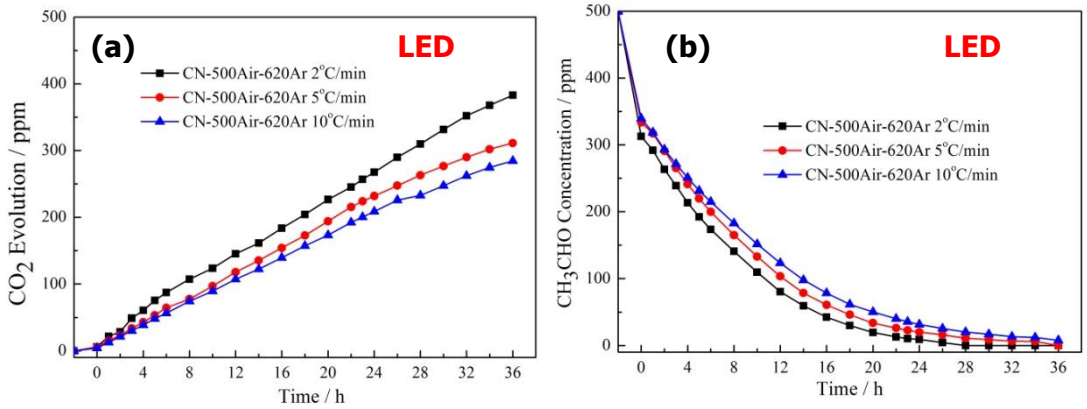

Figure 37 Photocatalytic activity evaluation of CN photocatalysts under visible light irradiation. (a) CO_2 evolution, (b) CH_3CHO concentration variation.

Figure 37 showed the effect of temperature ramping rate on photocatalytic activity of acetaldehyde degradation. The results showed that the activity increased with lowering the temperature ramping rate. It is because with decreasing the temperature ramping rate, the number of defects can also be reduced simultaneously, which is clearly demonstrated by the PL spectra in Figure 34(c). By lowering the temperature ramping rate, the UV-vis also shows a red-shift. Therefore, it means the CN photocatalyst prepared at 2 °C/min is with better charge carrier separation efficiency.

4.4.3 Activity evaluation of CN with different thermal temperature

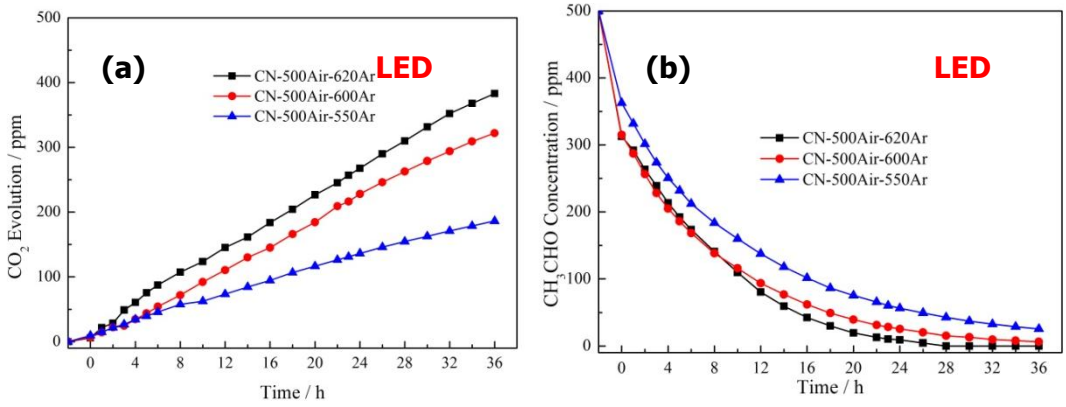

Figure 38 Photocatalytic activity evaluation of CN photocatalysts under visible light irradiation. (a) CO_2 evolution, (b) CH_3CHO concentration variation.

Figure 38 gave the activity evaluation results of CN photocatalysts prepared at various thermal treatment temperatures. From the time course of CO_2 evolution in Figure 38(a), the activity of CN-500Air-620Ar showed about 2 times higher than that of CN-500Air-620Ar sample. Such enhancement is mainly ascribed to the specific surface increment and numerous meso-porous introduced by 620 °C treatment, while under the irradiation of LED 435nm, the absorption intensity of these two samples are almost the same, as shown in Figure 35(b) and Figure 35(d).

4.4.4 Activity evaluation of CN with different thermal atmosphere

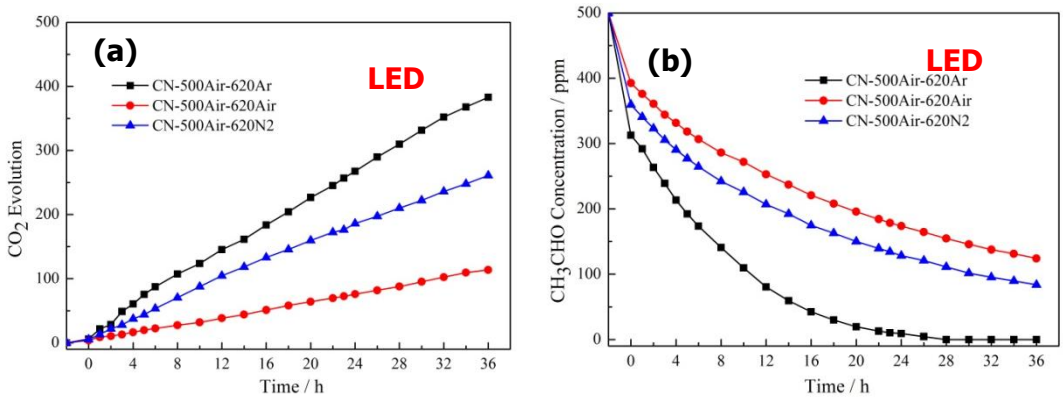

Figure 39 Photocatalytic activity evaluation of CN photocatalysts under visible light irradiation. (a) CO_2 evolution, (b) CH_3CHO concentration variation.

In order to verify the necessity of two-step thermal treatment under Ar atmosphere, N_2 and Air atmosphere were also adopted in photocatalytic activity evaluation experiments. The results were presented in Figure 39. Interestingly, in inert gases (N_2 or Ar) as the thermal treatment atmosphere, a relatively higher photocatalytic performance can be achieved, at least 2 times up than that of CN prepared at Air atmosphere. It may because at Air atmosphere, C and N elements would react with O_2 while N_2 or Ar is beneficial for the removal of the residual ammonia groups in graphitic carbon nitride.

4.4.5 Activity evaluation of CN with 480nm cut-off

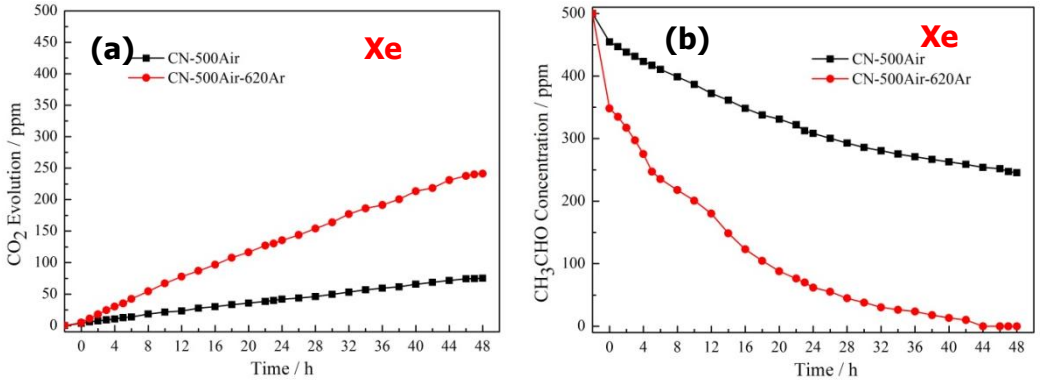

Figure 40 Photocatalytic activity evaluation of CN photocatalysts under Xe-lamp with 480 nm cut-off irradiation. (a) CO_2 evolution curves, (b) CH_3CHO concentration variation.

As CN-500Air and CN-500Air-620Ar samples are with the approximate absorption values at 435 nm wavelength as shown in Figure 35(b). Therefore, we need further to select an appropriate irradiation light source. Herein, Xe lamp with 480 nm cutoff filter is adopted as the light source. Because the adsorption edge of CN-500Air is 460nm, it is with very weak absorption (Abs=0.185) under irradiation wavelength $\lambda > 480$ nm. However, CN-500Air-620Ar sample shows strong absorption (Abs=0.586) under irradiation wavelength $\lambda > 480$ nm. As shown in Figure 40, the photocatalytic activity was enhanced 5 times higher under irradiation with wavelength longer than 480 nm. Besides, CN-500Air-620Ar sample also possesses an extremely faster CH_3CHO adsorption kinetics than CN-500Air sample. Within 48 hours, 500 ppm CH_3CHO was fully adsorption by CN-500Air-620Ar sample, while only 250 ppm CH_3CHO was adsorption by CN-500Air sample. Typically, adsorption of VOCs on photocatalyst surface is the prerequisite condition for the subsequent degradation. Therefore, this CN-500Air-620Ar photocatalyst is one of the optimal candidates for environmental remediation.

4.5 Conclusions

In this section, a facile and feasible surface modification method was established via two-steps thermal treatment (as presented in Figure 41), the optical adsorption edge of g-C_3N_4 photocatalyst was extended from 460 nm to 650 nm, and it also presented a larger specific surface area. As a good visible-light-responsive photocatalyst with extremely high charge carriers' separation efficiency, it exhibits a much superior activity in CH_3CHO degradation to CO_2. With respect to CN-500Air, the photocatalytic activity of g-C_3N_4 prepared by two-steps thermal treatment was enhanced 5 times higher under irradiation with wavelength longer than 480 nm. Therefore, this two-step thermal treatment is a good approach to enhance photooxidation ability of g-C_3N_4.

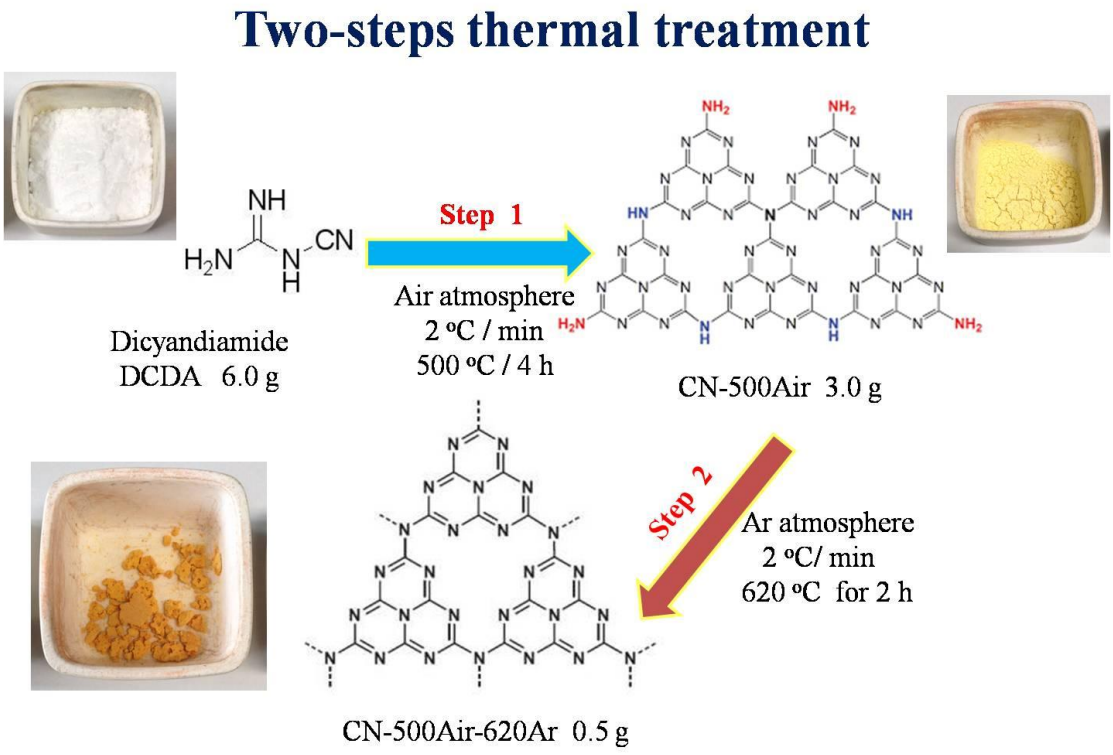

Figure 41 A facile and feasible route to extend the visible light absorption of g-C_3N_4 photocatalysts by the two-steps thermal treatment.

Chapter 5 Construction of g-C_3N_4-based nanohybrid heterojunctions

5.1 Introduction

With face-centered cubic (fcc) structure, cerium dioxide (CeO_2) has been successfully employed as catalyst or catalyst support for various reactions because of its excellent oxygen storage capacity (OSC). Especially, shape-controlled synthesis of CeO_2 nanocrystals has received great attention due to their unique shape-dependent properties. Besides, hydrothermal method has been proven to be particularly effective in controlling the size and morphology of various nano-materials. These characteristics suggest that morphology controlled CeO_2 could be potentially used as a photocatalyst for the oxidation of pollutants (as illustrated in Figure 42). Meanwhile, g-C_3N_4 has turned out to be a fascinating choice for a visible photocatalyst to photochemical splitting of water and some photoreduction reactions. However, the photogenerated electrons and holes easily recombine which restricts its photocatalytic performance and the photooxidation ability is also weak due to its low valence band. Therefore, the purpose of this research work is the improvement of the photooxidation activity of g-C_3N_4 by morphology controlled CeO_2 nanocrystals.

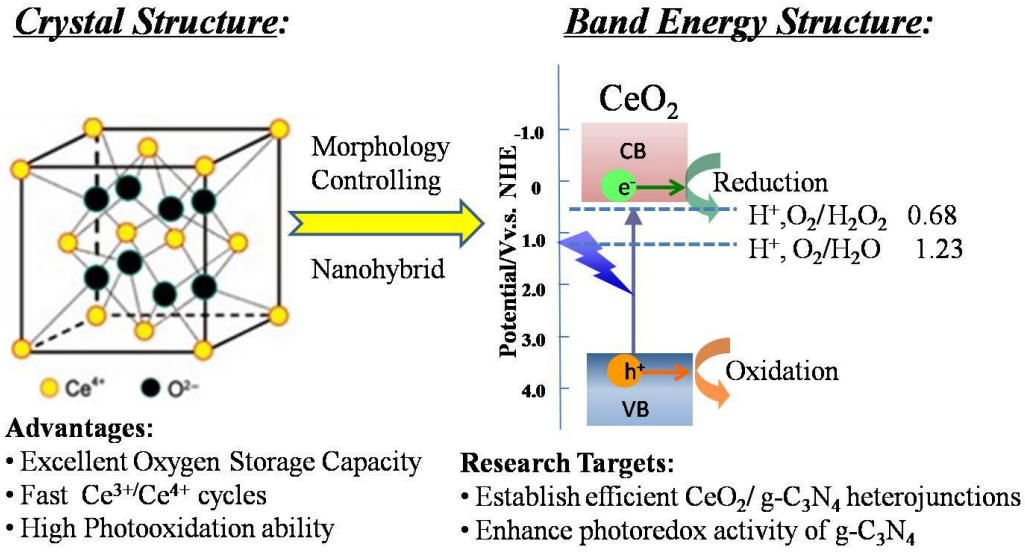

Figure 42 Crystal and band energy structure of CeO_2

5.2 Experimental

5.2.1 Materials

Sodium Hydroxide (Wako) Assay min 97.0%; Cerium(III) Nitrate Hexahydrate (Wako) Assay min 98.0%; Potassium bicarbonate (Wako) Assay min 97.0%;Nickel(II) Nitrate Hexahydrate (Wako) Assay min 98.0%; Ethanol (Wako) Assay min 99.5%; Melamine (Wako) Assay min 99.0%; Acetaldehyde(SIGMA-ALDRICH) ACS reagent Assay min 99.5%; Rhodamine B were purchased from Wako Pure Chemical Industries, Ltd. Bismuth subcarbonate powders were commercial samples purchased from Alfa Aesar. Acetaldehyde and potassium dichromate were purchased from Sigma-Aldrich. Both of them are extremely toxic and carcinogenic, and the use of personal protective equipment is required.Pure Carbon Dioxide (Taiyo Nippon Sanso) Assay min 99.995%; Pure Air (Taiyo Nippon Sanso) CO_2 < 0.1ppm.

5.2.2 Preparation of samples

5.2.2.1 Preparation of morphology controlled CeO_2 nanocrystals

Various solvothermal treatments: 2 mmol Ce $(NO_3)_3 \cdot 6H_2O$, 2 mmol PVP and certain volume ratio of ethanol/water (10/30) were added to Teflon reaction lined equipped with stainless steel autoclave. And then, it was placed in an oven at 160 ^{o}C under assistance of stirring and microwave treatment. The controlled experiment was also carried out in the absence of stirring and microwave treatment. After cooling, the residue was centrifuged, dried, the obtain products were denoted by SR-CeO_2, MW-CeO_2 and CE-CeO_2, respectively.

Various solvothermal reaction times: 2 mmol Ce $(NO_3)_3 \cdot 6H_2O$, 2 mmol PVP and certain volume ratio of ethanol/water (10/30) were added to Teflon

reaction lined equipped with stainless steel autoclave. And then, it was placed in an oven at 160 °C for 1h, 3h, 6h, 12h, 18h, 24h, and 48h. After cooling, the residue was centrifuged, dried, the obtain products were denoted by 1h-CeO_2, 3h-CeO_2, 6h-CeO_2, 12h-CeO_2, 18h-CeO_2, 24h-CeO_2 and 48h-CeO_2.

Various basic concentrations: 2 mmol Ce $(NO_3)_3 \cdot 6H_2O$, 2 mmol PVP , certain volume ratio of ethanol/water (10/30) and different concentrations of NaOH (2M, 1M, 0.5M, 0.1M) were added to Teflon reaction lined equipped with stainless steel autoclave. And then, it was placed in an oven at 160 °C for 18h. The as-synthesized yellow powder was marked as 2M-CeO_2, 2M-CeO_2, 1M-CeO_2, 0.5M-CeO_2, 0.1M-CeO_2.

Various ethanol/water ratios: 2 mmol Ce $(NO_3)_3 \cdot 6H_2O$, 2 mmol PVP and various volume ratio of ethanol/water (40/0, 30/10, 20/20, 17/23, 10/30, 0/40) were added to Teflon reaction lined equipped with stainless steel autoclave. And then, it was placed in an oven at 160 °C for 18h. After cooling, the residue was centrifuged, dried, the obtain products were characterized.

5.2.2.2 Preparation of in-situ grown CeO_2/g-C_3N_4 nanohybrid heterojunctions

Pure g-C_3N_4: 30 g melamine was heated at 550 °C for 4 h in electric furnace with a ramp rate of 2.3 °C/min, then the yellow bulks were ground into powder, denoted as Pure-g-C_3N_4.

CeO_2/g-C_3N_4: In a typical synthesis, the above as-prepared Pure-g-C_3N_4 (0.6 g), specified molar ratio of $Ce(NO_3)_3 \cdot 6H_2O$ (0mmol, 0.25mmol, 0.5mmol, 1.0mmol, 2.0mmol and 3.0mmol) were added to Teflon reaction lined equipped with stainless steel autoclave. After dispersed in ethanol/water (34ml/46ml) mixed solvent for 2 h, the autoclave was transferred to an oven at 160 °C for 18 h. After cooling, the residue was centrifuged, dried and ground. For simplification, the obtain products were denoted as mCeO_2/g-C_3N_4, where m=0, 0.25, 0.5, 1.0,

2.0 and 3.0. The controlled experiment was also carried out to prepare pure CeO_2 according with the same above procedure except addition of as-prepared Pure-g-C_3N_4.

5.2.2.3 Preparation of NiO/g-C_3N_4 and CeO_2/CN-Rods heterojunctions

As to prepare NiO/g-C_3N_4 heterojunctions, the preparation procedures are similar with in-situ grown CeO_2/g-C_3N_4 nanohybrid heterojunctions in 5.2.2.2, except using Ni $(NO_3)_2{\cdot}6H_2O$ as Ni source instead of $Ce(NO_3)_3{\cdot}6H_2O$. As to prepare CeO_2/CN-Rods heterojunctions, the preparation procedures are similar with in-situ grown CeO_2/g-C_3N_4 nanohybrid heterojunctions in 5.2.2.2, except using CN-Rods produced in Chapter 3 instead of Pure-g-C_3N_4.

5.2.2.4 Preparation of $Bi_2O_2CO_3$/g-C_3N_4 heterojunction photocatalysts

In a typical synthesis, the above as-prepared Pure-g-C_3N_4 (0.6 g) together with a specified molar ratio of $Bi_2O_2CO_3$ (hereafter denoted as BIOC) was first mixed in 20 mL deionized water and then transferred to a 50 mL agate bowl containing 50 g yttrium-stabilized zirconia (YSZ) grinding beads (0.6 mm in diameter, Nikkato Co.,). The agate bowl was put on a planetary mill machine (Planetary Micro Mill pulverisette 7, Fritsch Japan Co.,), operating at 750 rpm for 10 min with 3 repetitions. After cooling to RT, the YSZ beads could be moved by screening, and the sample was separated by filtration, washed with deionized water 3 times, and dried in a vacuum drying oven at 60 $^{\circ}$C overnight. These as-prepared samples were denoted as mBIOC-CN, where m= 0.125, 0.25, 0.5, 1.0, 1.5 and 3.0 mmol. Control experiments were also carried out to prepare $Bi_2O_2CO_3$ and g-C_3N_4 counterparts by the same procedure as that described above, and they are denoted as BIOC-PM and CN-PM. Samples without any treatment are denoted as BIOC-Bare and CN-Bare.

5.2.3 Characterization

The samples were characterized by XRD, SEM, TEM, HR-TEM, BET, FTIR, PL, XPS and UV-vis. The detailed instrument models and relevant parameters refer to the characterization section given in chapter 2.

5.2.4 Photocatalytic activity experiment

CH_3CHO photooxidation: In this section, 500 ppm CH_3CHO was still adopted as model pollution to evaluate the photocatalytic performance under visible light irradiation. The evaluation process and parameter setting are same with chapter 2.

2-propanol photooxidation: Samples powder (100 mg), which had completed extinction of incident radiation, was spread on a glass dish, and the glass dish was put into a Tedlar bag (AS ONE Co. Ltd.) with a volume of 125 mL mixed air (79% N_2, 21% O_2, <0.1 ppm of CO_2, 500 ppm of 2-propanol). After 2 h adsorption equilibrium in the dark, the photocatalysts were exposed under the visible light (LED with central wavelength of 435 nm). The light intensity was fixed to 3 mW/cm^2. In the photocatalysis process, generation of carbon dioxide, acetone and consumption of 2-propanol were monitored by online gas chromatography (Agilent Technologies, 3000A Micro-GC, TCD detector) equipped with OV1 and PLOT-Q columns.

CO_2 photoelectrochemical reduction: The photoelectrochemical CO_2 reduction evaluation tests were carried out in three electrode cell irradiated by a portable solar simulator (PEC-L01). A FTO glass (1.5cmx4cm) coated with photocatalyst films (coated by electrophoretic deposition method), a glassy carbon, and Ag/AgCl electrode were used as working, counter, and reference electrode, respectively. The cell was made of quartz glass, and 0.3M $KHCO_3$ was used as an electrode. Before irradiation, the solution was saturated with CO_2 for 30 min

and simultaneously the oxygen was also fully removed. The photocurrent was measured by linear sweep voltammeter (LSV) from +1.2 to -1.2V (vs. Ag/AgCl) with a scan rate of 10mV/s. The Chrono-Amperometry (CA) measurement was conducted at -0.4 V (vs Ag/AgCl), as a meaning -0.2 V applied bias (vs.NHE = 0V) was applied in this photoelectrochemical CO_2 reduction system. Finally, the concentration of generated reaction products in liquid and gas phases were analyzed by gas chromatography (Hitachi G-3500, FID detector) with DB-WAXETR columns, and ion chromatography (Dionex, ICS-900) with IonPac AS-12A column.

RhB degradation and Cr (VI) photoreduction: RhB dye and heavy metal Cr (VI) ions are regarded as common contaminants in domestic and industrial waste water. They were therefore selected as model pollutants to evaluate the photocatalytic activity of the as-prepared photocatalysts. The experimental procedures were as follows. First, 50mg of the photocatalyst was dispersed in a 50 mL Pyrex glass container with 2×10^{-5} mol L^{-1} RhB aqueous solution (10 mg L^{-1}) or 1.7×10^{-4} mol L^{-1} $K_2Cr_2O_7$ aqueous solution (50 mg L^{-1}). Prior to irradiation, the suspensions were magnetically stirred in the dark for 60 min to ensure adsorption equilibrium. Then the sample was irradiated by a 500 W Xe arc lamp (OPM2-502XQ, USHIO) with a heat-absorbing filter (Sigma Koki) and a 400 nm cutoff filter (Sigma Koki). The light intensity was measured to be 25 mW cm^{-2} (Orion-TH, Ophir Optronics). At certain time intervals, 3 mL of the suspension was sampled and centrifuged to remove the solid samples. The concentrations of supernatant liquid were analyzed by an UV-vis spectrophotometer (Shimadzu, UV-2600) according to the peak value of maximum absorption (λ_{max}=554 nm for RhB, λ_{max}=373 nm for $K_2Cr_2O_7$). The amount of H_2O_2 generated during photocatalytic oxidation of RhB degradation was analyzed by iodometry according to a previous report[189].

5.2.5 Photoelectrochemical measurements

The photoelectrodes were prepared by electrophoretic deposition (EPD) method on conducting FTO glass supports (Asahi Glass Co.). As displayed in Figure 43, EPD was carried out in acetone (30 mL) containing photocatalysts powder (50 mg) and iodine (20 mg), which was dispersed by sonication for 15 min. Two FTO electrodes (1.5 X 4 cm^2) were immersed parallel in the solution with a distance of 10 mm, and 15 V of bias was then applied between the electrodes for 3 min using a potentiostat (HAL-3001, Hokuto Denko Co.). The coated area was controlled to be ca. 1.5 X 2 cm^2. The electrode was dried in air on a digital hot plate (HP-1SA, As One Co.) at 200 ^{o}C for 2 hours. Transient photocurrent response measurements of the as-prepared photoelectrodes were carried out by using an automatic polarization system (HSV-100, Hokuto Denko Co.) with a three electrode system, in which the prepared electrode, a Pt electrode and a silver–silver chloride (Ag/AgCl) electrode were used as a working electrode, counter electrode and reference electrode, respectively. The electrolyte used was 0.1 M Na_2SO_4 solution, which was bubbled with Ar gas for 30 min to remove dissolved air. The pH of the solution after bubbling was pH 6.8. The light source and intensity used were same with the conditions in RhB degradation and Cr (VI) photoreduction.

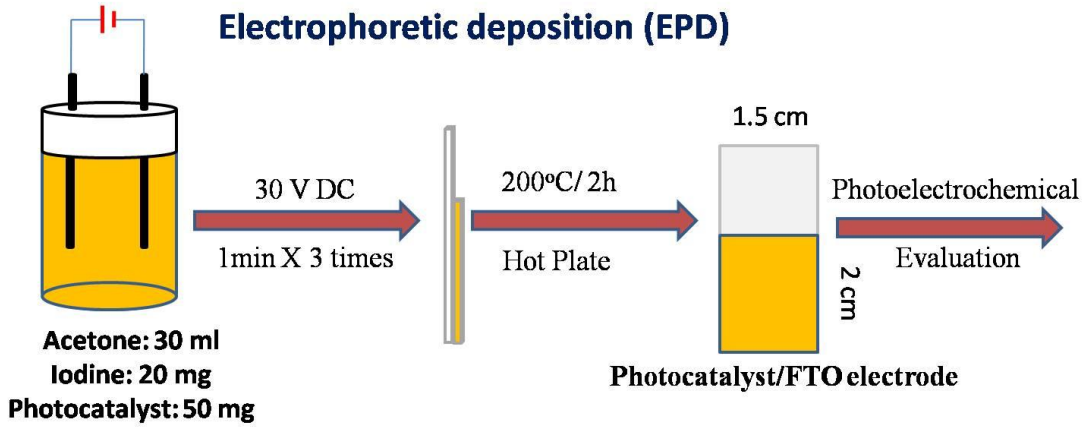

Figure 43 Films electrode prepared by electrophoretic deposition (EPD)

5.3 Results and discussion

5.3.1 Morphology controlling and photocatalytic activity of CeO_2

5.3.1.1 Effect of different solvothermal treatment methods

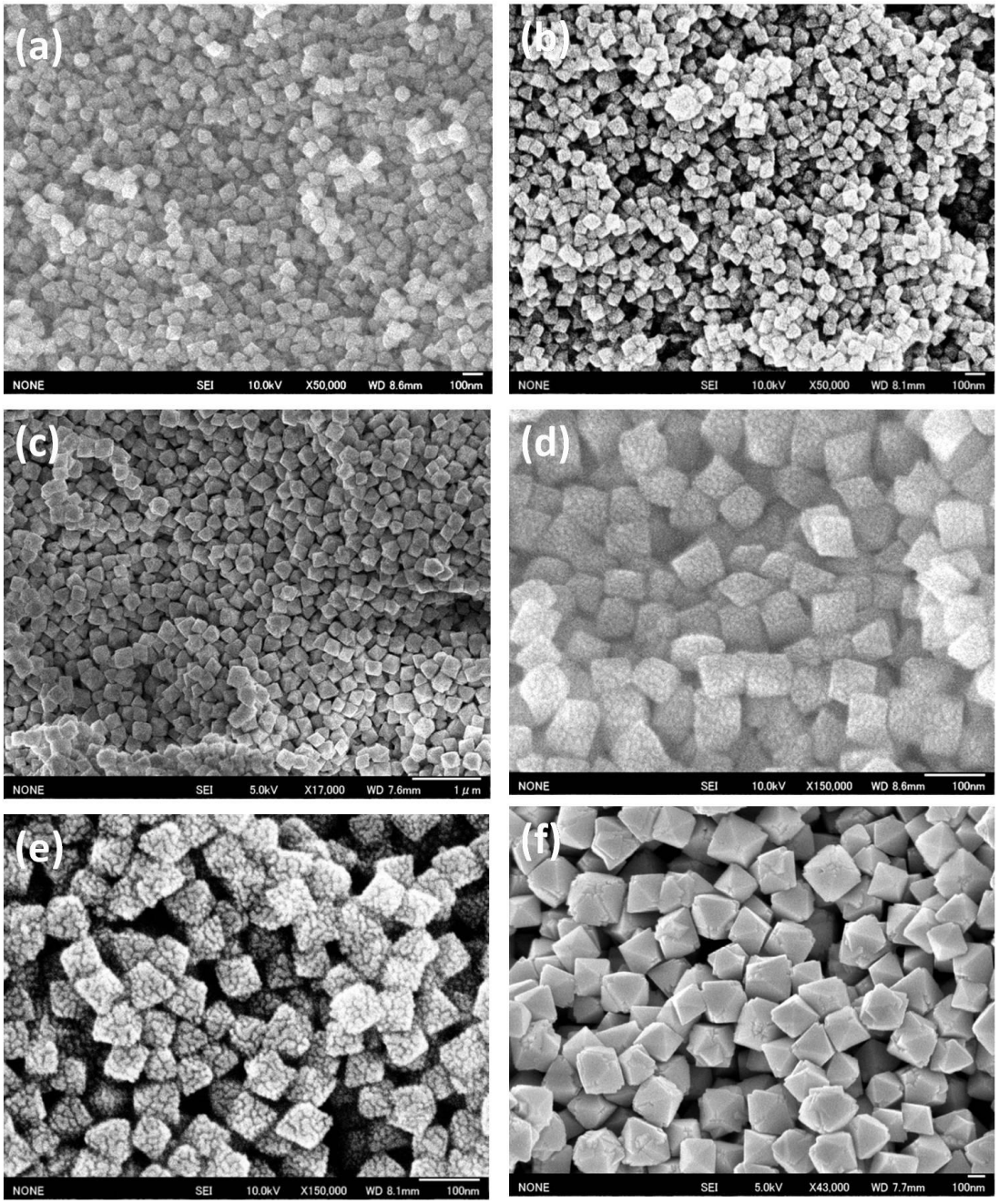

Figure 44 SEM images of CeO_2 nanocrystals prepared by different solvothermal treatment methods. (a, c) ST-CeO_2, (b, e) MW-CeO_2 and (c, f) CE-CeO_2.

Figure 44 shows SEM images of CeO_2 prepared by various methods. From Figure 44(a, c), it indicates well-defined octahedral CeO_2 NPs with diameter of 80 nm were successfully fabricated by solvothermal treatment in the assistance of stirring. The as-prepared CeO_2 is marked as ST-CeO_2. Figure 44 (b, e) show that smaller octahedral CeO_2 NPs (70 nm) can be prepared by microwave assisted solvothermal reaction. Herein, the as-obtained CeO_2 is called MW-CeO_2 for short. Moreover, the controlled experiment was also carried out by solvothermal treatment in the absence of stirring and microwave. The SEM images of prepared CE-CeO_2 NPs were displayed in Figure 44(c, f), From SEM images of CE-CeO_2, we can observe that octahedral CeO_2 with diameter of 180nm. Meanwhile, the as-prepared CE-CeO_2 NPs also exhibits some defects on the edges and vertexes. Eventually, we draw a conclusion that good monodispersed octahedral CeO_2 NPs can be successfully prepared both by microwave assisted solvothermal or conventional treatment with a tailored ethanol/water volume ratio.

Figure 45 (a, b) show XRD patterns and UV-vis spectra of as-prepared CeO_2 nanocrystals by various solvothermal treatment. From XRD patterns in Figure 45(a), the diffraction peaks are well assigned to face-centered cubic fluorite crystal phase (JCPDS 34-0394), and the characteristics peaks are with good purity, indicating that no impurities coexist. Moreover, the UV-vis spectra in Figure 45(b) indicate the MW-CeO_2 octahedral NPs are with big red-shift absorption. In other words, The octahedral CeO_2 prepared by microwave assisted solvothermal treatment promotes its absorption in visible light region than that of ST-CeO_2 and CE-CeO_2.The phenomena is also in good consistence with the activity evaluation results of CH_3CHO photocatalytic degradation.

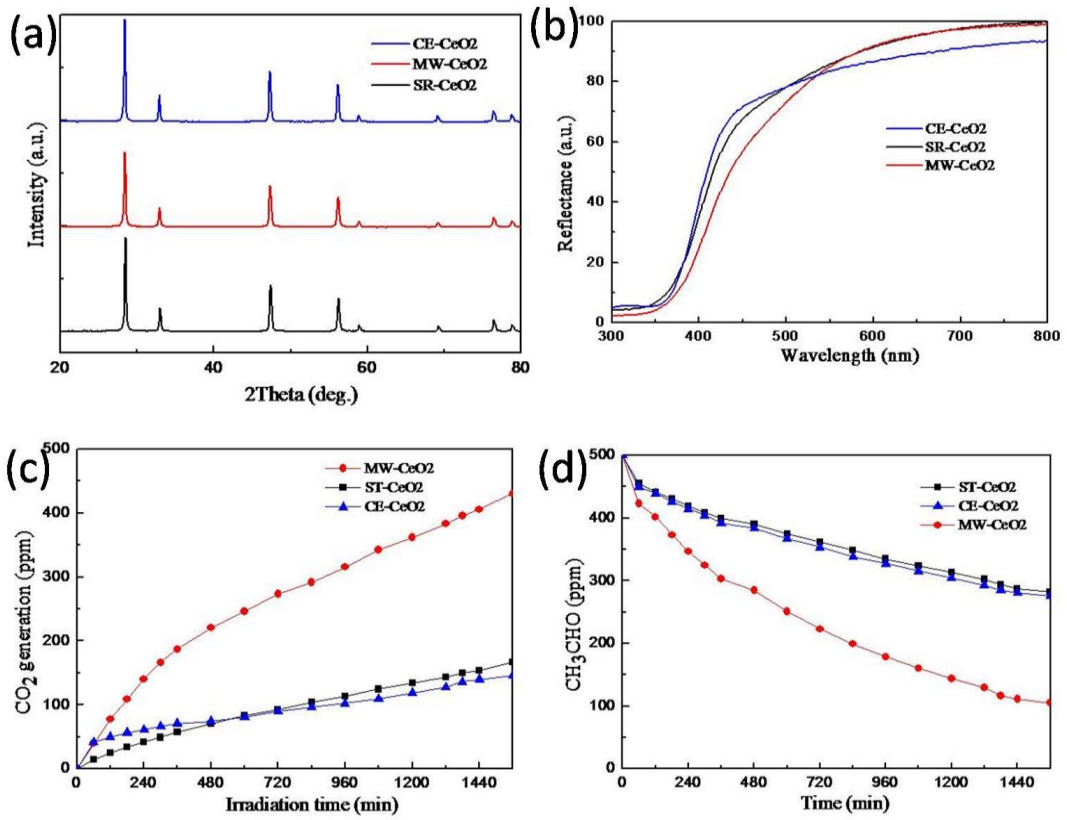

Figure 45 Structure and photoactivity characterization of CeO_2 nanocrystals prepared by different solvothermal treatment methods. (a) XRD patterns, (b) UV-vis spectra, (c) CO_2 evolution curves, (d) CH_3CHO concentration variation.

Figure 45(c, d) give the photocatalytic activity evaluation results. From Figure 45(a), we can conclude that the MW-CeO_2 displayed the highest CO_2 generation concentration, showing nearly 4 times higher activity than that of ST-CeO_2 and CE-CeO_2. The photocatalytic performance improvement of octahedral CeO_2 are mainly attributed to two reasons. On the one hand, the relatively smaller MW-CeO_2 NPs (70nm) are with better CH_3CHO adsorption ability, the curves in Figure 45(b) well proved this point. On the other hand, the MW-CeO_2 octahedral NPs show better visible light absorption and then much more photogenerated holes and electrons promote the improvement of photocatalytic performance, which is in good accordance with the UV-vis spectra in Figure 45(b).

5.3.1.2 Effect of various solvothermal reaction times

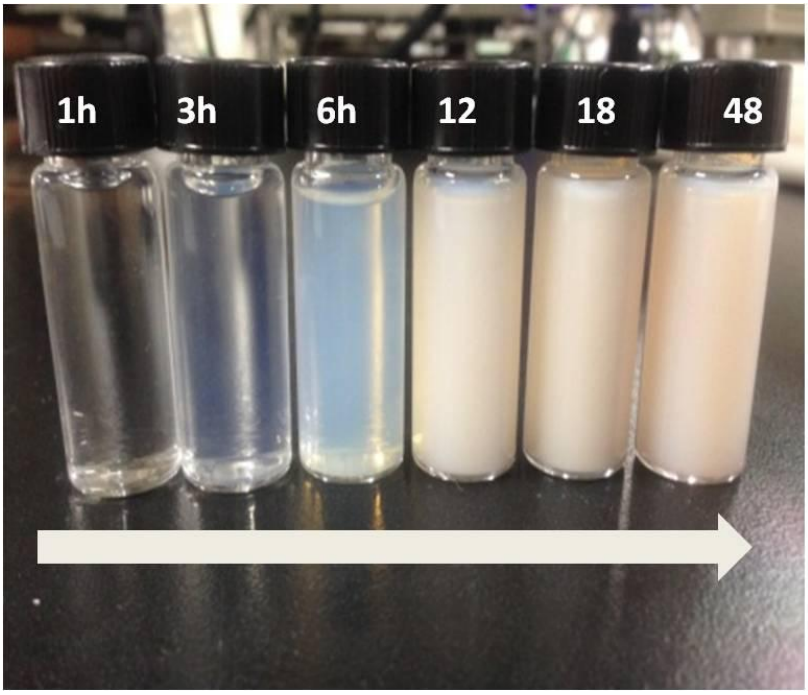

Figure 46 Color evolution of CeO_2 suspension with reaction time extension

Figure 46 shows the photographs of CeO_2 suspensions after various solvothermal reaction times from 1h to 48h. It can know that there is no product generated after 1h solvothermal reaction, the crystal grains appeared gradually after 6h solvothermal reaction. With the further prolongation of reaction time, the hydrolysis of Ce^{3+} to $Ce(OH)_3$ enhanced, then the $Ce(OH)_3$ intermediate product was gradually oxidized to CeO_2 NPs. Therefore, after 6 h reaction, the CeO_2 products are considerable and can be collected for photocatalytic activity evaluation. Figure 47 displays SEM images of CeO_2 prepared by various solvothermal reaction times. The SEM images indicated that octahedral CeO_2 NPs (ca. 60 nm) were prepared after 6h solvothermal reaction. The diameter can be increased to 90 nm after12h solvothermal reaction. The largest octahedral CeO_2 NPs (ca.180 nm) were formed at 18h reaction time. From this critical point, the diameter of octahedral CeO_2 would diminish to 110 nm at 24h reaction time and kept a constant value.

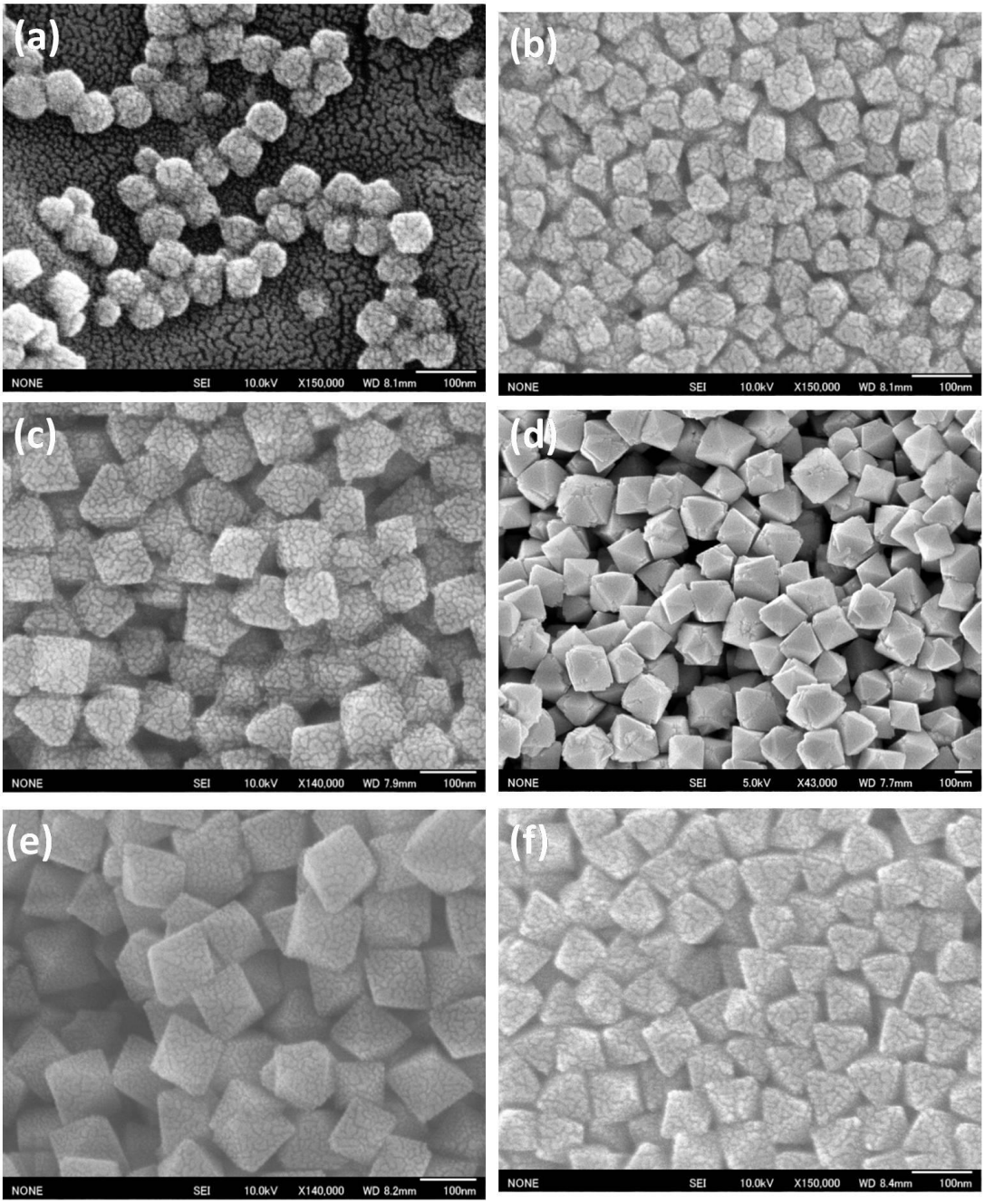

Figure 47 SEM images of CeO_2 nanocrystals prepared by various solvothermal reaction times. (a) 3h, (b) 6h, (c) 12h, (d) 18h, (e) 24h and (f) 48h. (Scale bars are all 100nm)

From XRD patterns in Figure 48(a), the diffraction peaks are well assigned to face-centered cubic fluorite crystal phase (JCPDS 34-0394), and the characteristics peaks are pure, indicated no impurities coexisted. Moreover, The obviously broaden diffraction peak of 12h-CeO_2 demonstrated a relatively

smaller CeO_2 particles were formed, which is in good consistence with SEM images in Figure 47. Moreover, Figure 48(b) indicated that CeO_2 prepared by various solvothermal reaction times possessed different absorption edges, the 48h-CeO_2 NPs showed a better visible light absorption. From Figure 48 (c), we can conclude that the 12h-CeO_2 displayed the highest CO_2 generation concentration, showing nearly 2 times higher activity than that of 18h-CeO_2, 24h-CeO_2 and 48-CeO_2. The photocatalytic performance improvement of octahedral 12h-CeO_2 is attributed to its relatively smaller diameter (ca.90 nm) and higher Ce^{3+} contents, because the smaller particle is with higher specific surface area. The curves in Figure 48(b) well proved this point.

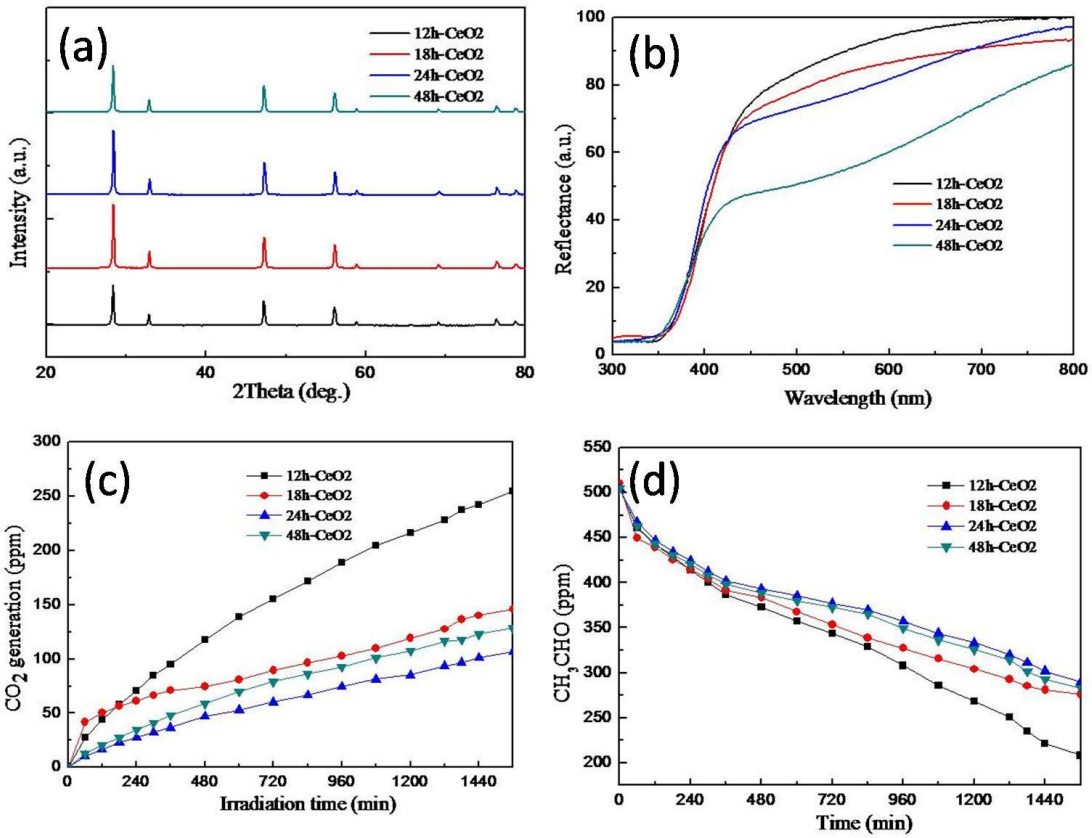

Figure 48 Structure and photoactivity characterization of CeO_2 nanocrystals prepared by different solvothermal reaction times. (a) XRD patterns, (b) UV-vis spectra, (c) CO_2 evolution curves, (d) CH_3CHO concentration variation.

5.3.1.3 Effect of Basic Solvothermal Medium

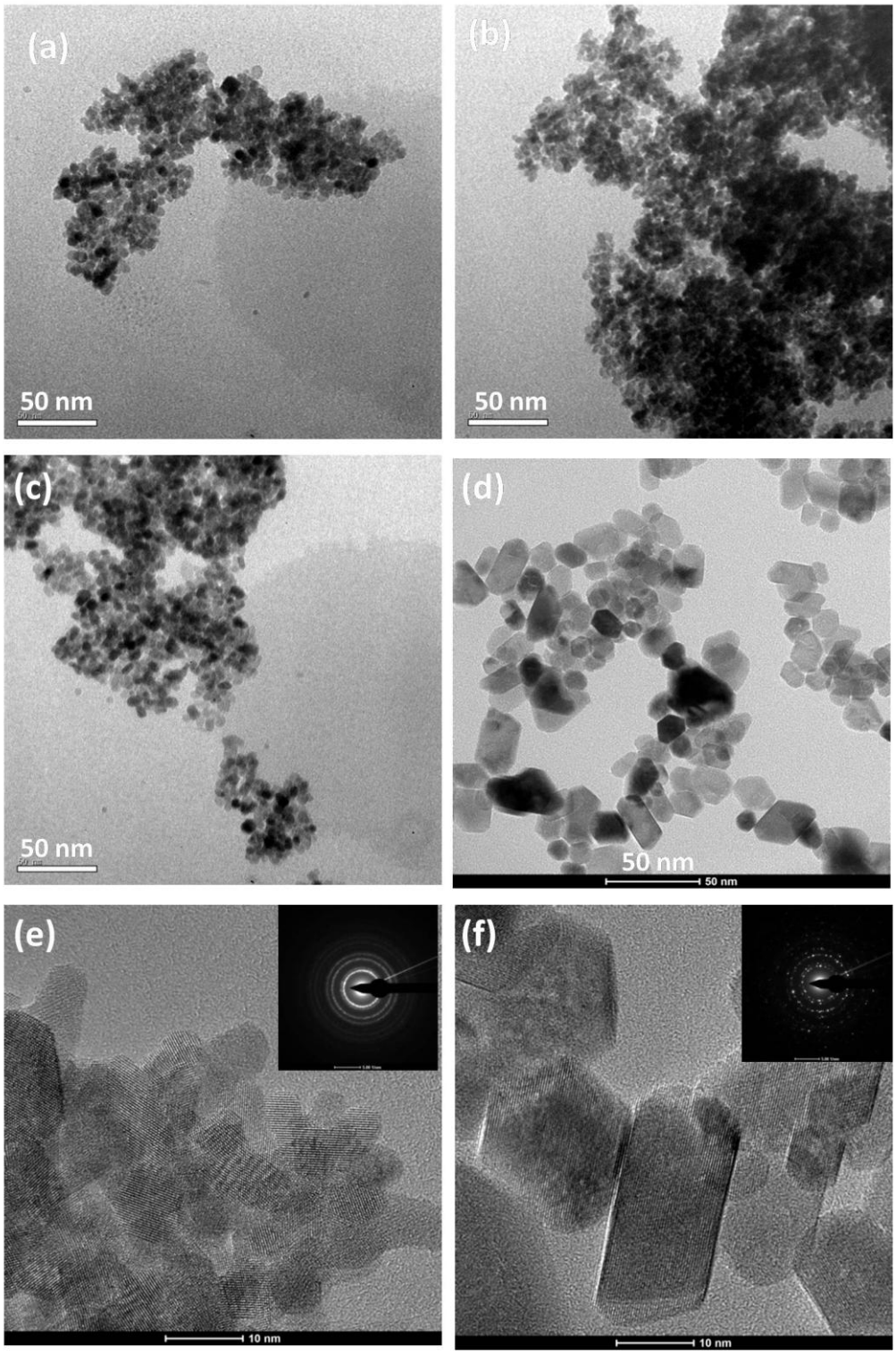

Figure 49 TEM images of as-prepared CeO_2 in various concentrations basic medium. (a) 2M (b) 1M (c) 0.5M (d) 0.1M and HR-TEM images and SAED patterns of (e) 0.5M and (f) 0.1M.

Figure 49 presents TEM images of as-prepared CeO_2 in various concentrations basic medium. CeO_2 NPs (< 10 nm) with severe aggregation were prepared in high concentration NaOH solutions by solvothermal treatment (Figure 49(a-c)), which is attributed to the fast speed hydrolysis of Ce^{3+} ions. Numerous small grains are formed in a short period. Meanwhile, in order to decrease the surface energy, the small grains are apt to aggregate. The inset SAED pattern in Figure 49(e) confirmed that the aggregated CeO_2 NPs are polycrystalline. When the concentration of NaOH solution was decreased to 0.1M, CeO_2 nanorods with exposed well-defined crystal facets were fabricated. The nanorods also displayed a relatively lower length-diameter ratio. It indicated that the $Ce(OH)_3$ grains have enough time to grow to be nanorods with good crystalline quality in a relatively low concentration NaOH solution.

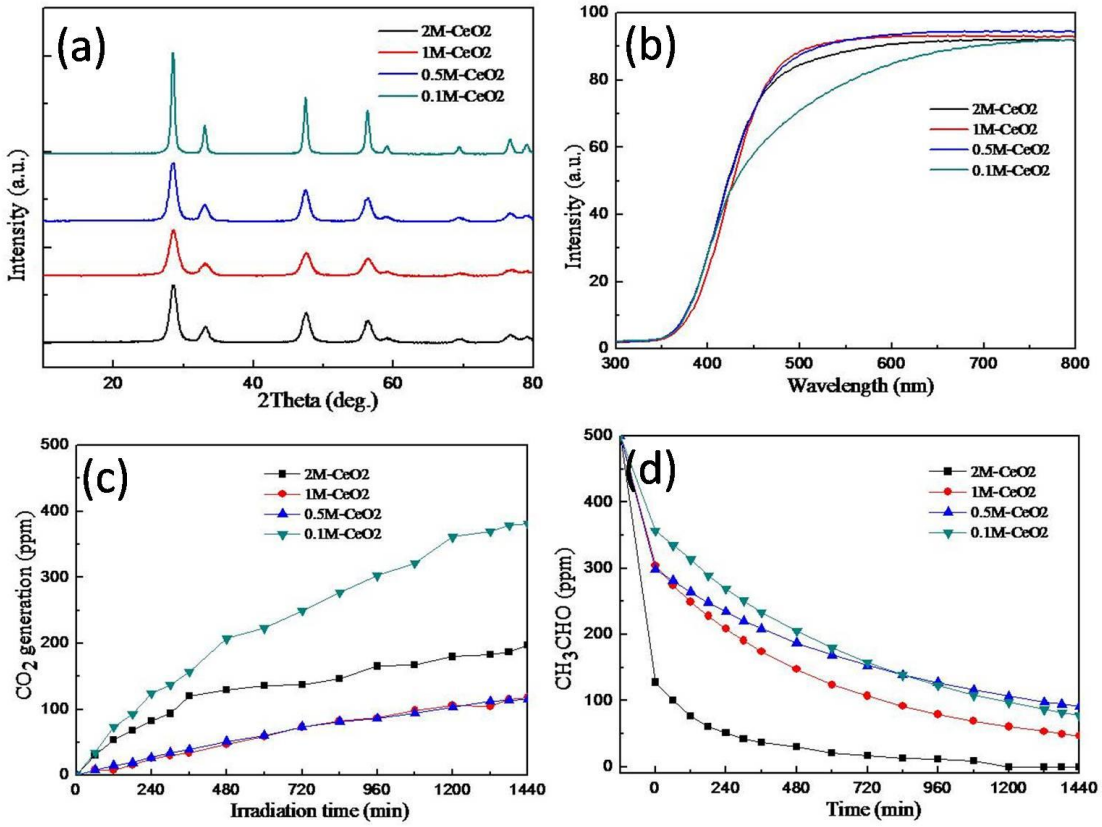

Figure 50 Structure and photoactivity characterization of CeO_2 nanocrystals prepared by different concentrations of basic medium. (a) XRD patterns, (b) UV-vis spectra, (c) CO_2 evolution curves, (d) CH_3CHO concentration variation.

From XRD patterns in Figure 50(a), the sharp and narrow diffraction peak of 0.1M-CeO_2 indicated that the good crystalline and growth to bigger grains. From Figure 50(b), we can observe that the 0.1M-CeO_2 nanorods are with a better visible light adsorption. The blue-shift of the other three CeO_2 NPs (< 10 nm) is attributed to the quantum confinement effect. Figure 50(c, d) shows the photocatalytic activity evaluation results of the CeO_2 prepared in different NaOH concentrations. The CeO_2 nanorods exhibit the best photocatalytic activity to degrade the CH_3CHO to CO_2, showing nearly 4 times higher activity than that of 1M-CeO_2 and 0.5M-CeO_2. The performance improvement of CeO_2 nanorods are mainly attributed to two reasons. Firstly, the nanorods CeO_2 are with better crystalline and dispersity. Moreover, the well-defined exposed high-index crystal facets may promote the efficiency separation of photogenerated electron-hole pairs.

5.3.1.4 Effect of Different Ethanol/Water Ratios

Figure 51 indicates that with increasing of ethanol volume, the diameter of CeO_2 decreased. Uniform octahedral CeO_2 with diameter of 250 nm was obtained by tuning ethanol/water volume ratio at 17:23. Monodisperse spherical nano-CeO_2 can be fabricated when ethanol/water ratio was less than 30:10. The growth mechanism of CeO_2 particles follows two stages, the initial nucleation of CeO_2 nuclei and the subsequent ripening of nuclei in the hydrothermal process. The nucleation involves the precipitation of Ce^{3+} cations by OH^- ions to form $Ce(OH)_3$ nanoparticles and the transition from $Ce(OH)_3$ to 2～3 nm CeO_2 nuclei through an oxidation and rapid dehydration process. The mixed solvents affect the polarity of the reaction system and the addition of ethanol restrains the nucleation of CeO_2 nuclei leading to the decrease of CeO_2 particles. Therefore, ethanol/water volume ratios play a vital role in controlling the morphology of CeO_2 nanocrystals.

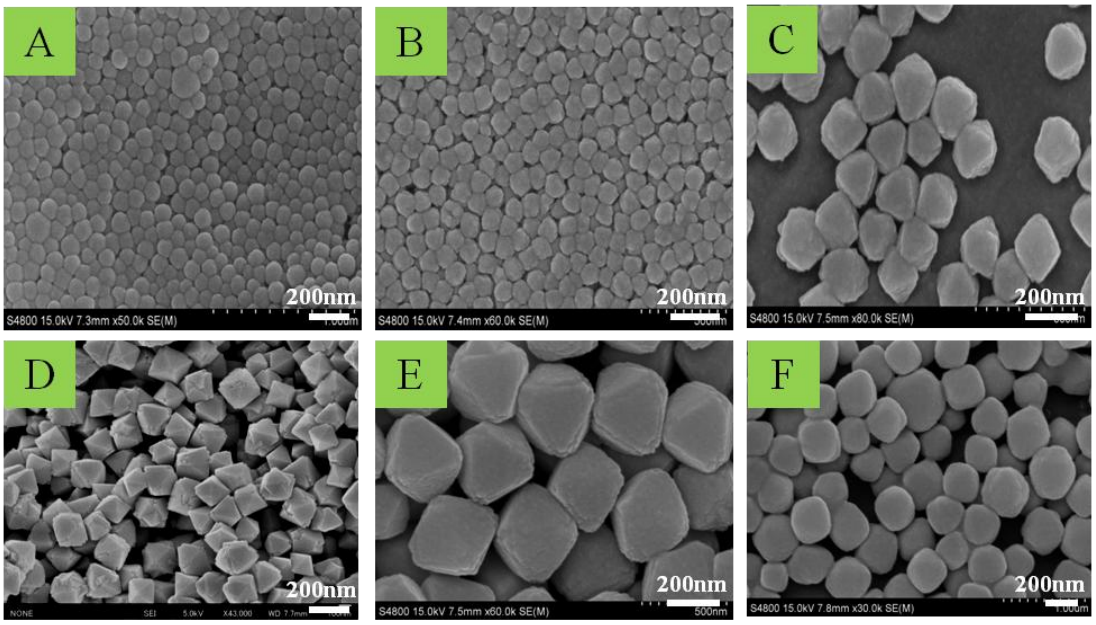

Figure 51 SEM images of CeO_2 nanocrystals prepared in different EtOH: H_2O ratios. (A) 40:0, (B) 30:10, (C) 20:20, (D) 17:23, (E) 10:30 and (F) 0:40.

5.3.2 Characterization and photocatalytic activity of CeO_2/g-C_3N_4

5.3.2.1 Morphology characterization of in-situ grown CeO_2/g-C_3N_4 nanohybrids

The shape and size information of the in-situ grown CeO_2/g-C_3N_4 nanohybrid photocatalysts were obtained by scanning electron microscope, as shown in Figure 52. Figure 52(A) shows that bulk g-C_3N_4 synthesized from melamine pyrolyzation is with sheet-stacked structure and the surface is smooth and several microns. However, g-C_3N_4 sheets would be partially etched and peeled by ethanol/water mixed solvothermal treatment (shown in Figure 52(B)). Simtaneously, the specific surface area of g-C_3N_4 increased from 10.4 m^2/g to 31.9m^2/g originated from breakdown of marginal $-NH_2$ from g-C_3N_4 matrix. The released NH_3 gases introduced a great number of disordered mesopores, which is well consistent with BET and BJH calculation results (Figure 53(a)).By comparison with SEM images of Figure 52(C-G), we can draw the conclusion that with increasing the mole ratios of cerium salts to the in-situ reaction

system with g-C_3N_4, the size and its coverage fraction of as-obtained CeO_2 nanocrystals on g-C_3N_4 surface increased gradually. In addition, octahedral CeO_2 nanoparticles with good dispersity as well as particle size distribution (PSD) were successfully fabricated on g-C_3N_4 substrate on condition that appropriate cerium salt mole ratio was adopted (here m < 2). Therefore, in-situ mixed solvothermal treatment has turned out to be a feasible approach to fabricated morphology controlled CeO_2/g-C_3N_4 nanohybrid photocatalysts. On the one hand, the negatively charged g-C_3N_4 sheets provide numerous "active-sites" for Ce^{3+} cations, so Ce^{3+} ions can uniformly anchor on g-C_3N_4 surface, because isoelectric point (IEP) of g-C_3N_4 is 6.32. On the other hand, the slow-released NH_3 gases from g-C_3N_4 sheets dissolve in the mixed solvent, and then the weak basic environment guarantees the growth and ripening of CeO_2 crystal grains. Therefore, octahedral morphology CeO_2 nanoparticles can be easily controlled by this method under the assistance of negatively charged g-C_3N_4. Meanwhile, the specific surface area of g-C_3N_4 can also be enlarged effectively (increased about 3 times).

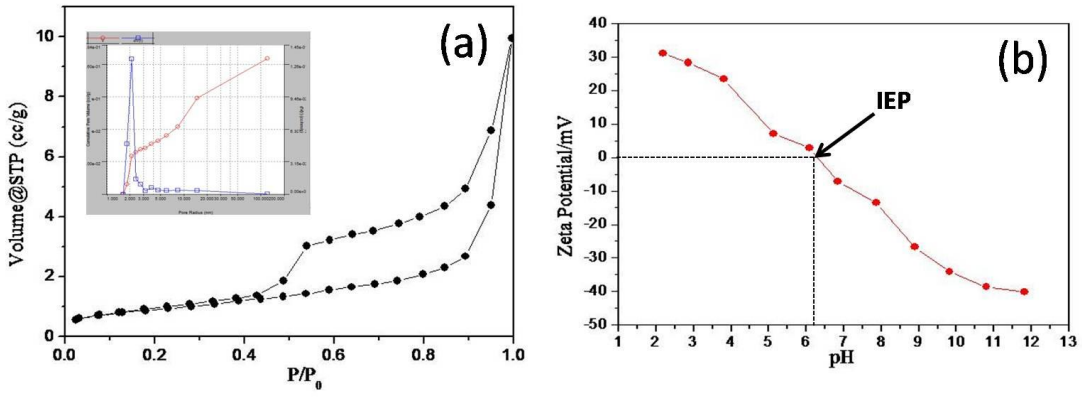

Figure 53 (a) Nitrogen adsorption-desorption isotherms and corresponding pore size distribution curves (inset) of mixed solvothermal treated g-C_3N_4; (b) Zeta potential curves change by pH of mixed solvothermal treated g-C_3N_4.

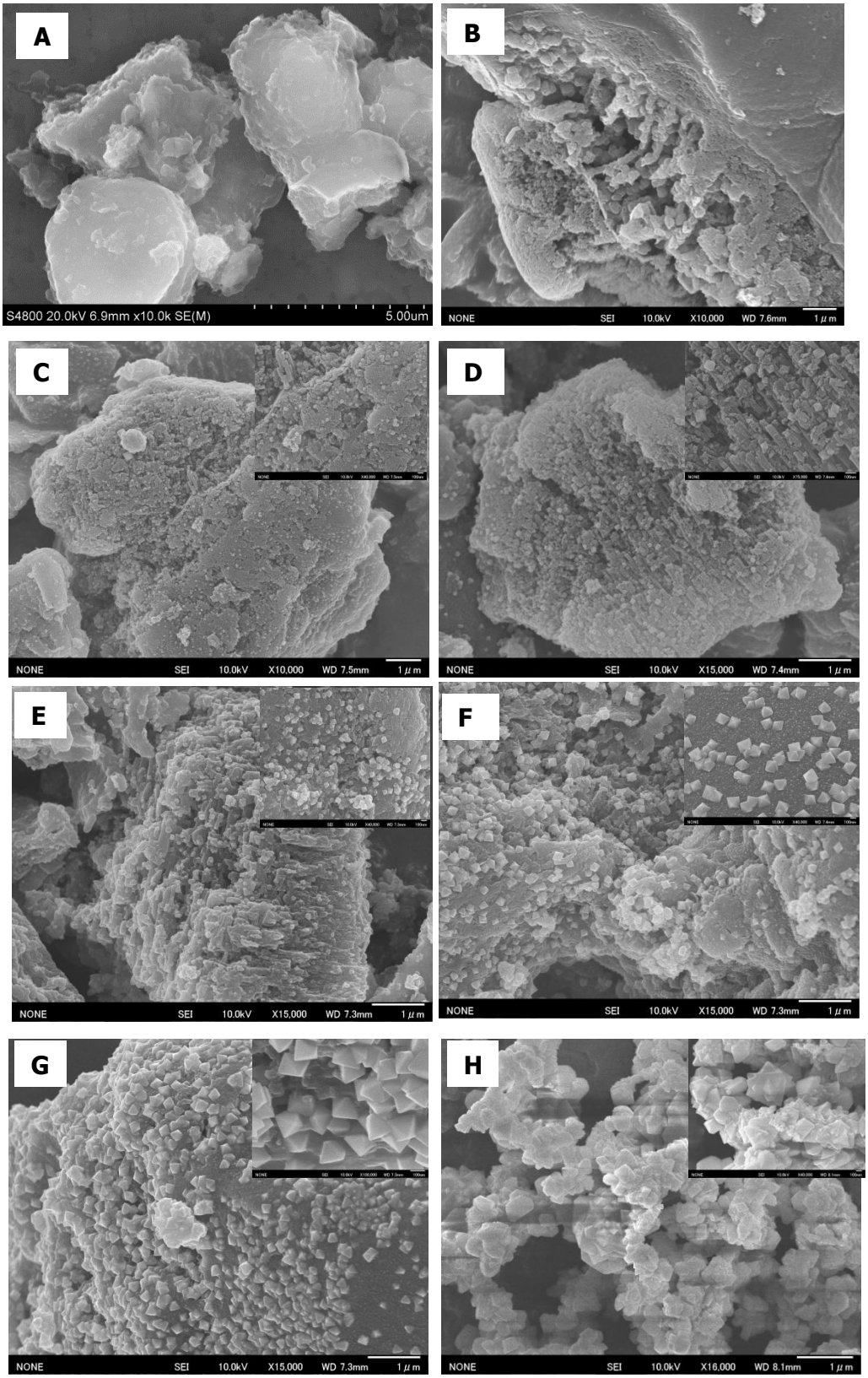

Figure 52 SEM images of $mCeO_2/g\text{-}C_3N_4$ nanohybrid photocatalysts. (A) Pure $g\text{-}C_3N_4$; (B) $0CeO_2/g\text{-}C_3N_4$; (C) $0.25CeO_2/g\text{-}C_3N_4$; (D)$0.5CeO_2/g\text{-}C_3N_4$; (E) $1.0CeO_2/g\text{-}C_3N_4$; (F) $2.0CeO_2/g\text{-}C_3N_4$; (G) $3.0CeO_2/g\text{-}C_3N_4$; (H)Pure CeO_2. (Scale bars in the main image and inset are 1μm and 100nm, respectively)

5.3.2.2 Structure characterization of in-situ grown CeO_2/g-C_3N_4 nanohybrids

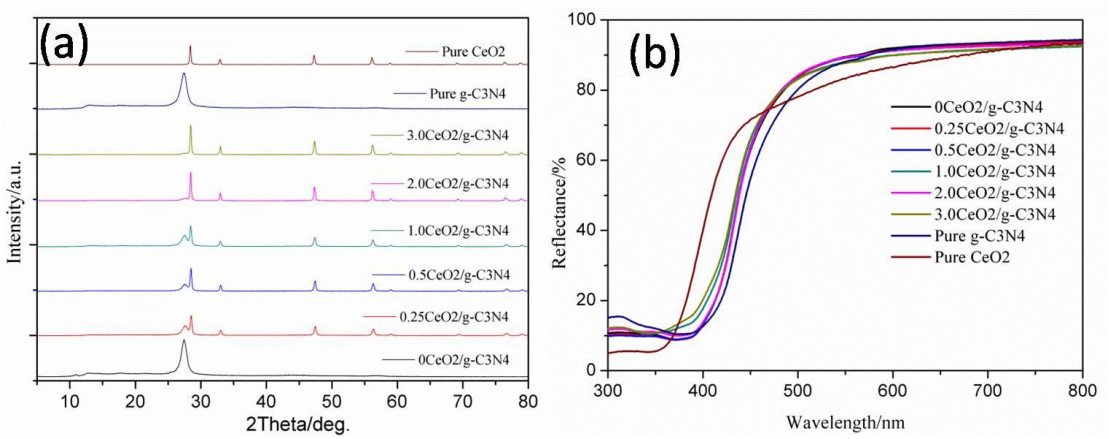

Figure 54 (a) XRD patterns, (b) UV-vis spectra of mCeO_2/g-C_3N_4 nanohybrids.

Figure 54 (a) shows the XRD patterns of a series of as-prepared mCeO_2/g-C_3N_4 nanohybrid photocatalysts. The two distinct diffraction peaks of pure g-C_3N_4 at 13.1°and 27.4°are respectively indexed as (100) and (002), which corresponds to distance of the in-plane structural packing motif (d=0.676nm) and aromatic segments interlayer stacking (d=0.326nm). which also matches well with literature reported values (JCPDS 87-1526).The peaks of pure CeO_2 are well assigned to face-centered cubic fluorite crystal phase (JCPDS 34-0394), the characteristics peaks are pure indicated no impurities coexisted .By analysis of the XRD patterns, we can also conclude that with increasing of Cerium salts amount, the g-C_3N_4 surface was gradually covered by generated CeO_2 nanoparticles, because the peak intensity of g-C_3N_4 at (002) became weaken in mCeO_2/g-C_3N_4 (where m=0,0.25,0.5.1.0,2.0,3.0). The XRD results are also well accordance with SEM images shown in Figure 52. Figure 54(b) exhibits the diffuse reflectance spectra of mCeO_2/g-C_3N_4.It indicates that the pure CeO_2 shows relatively weak visible response, while the pure g-C_3N_4 has turned out to be as a good visible-light-driven photocatalyst. Therefore, the as prepared mCeO_2/g-C_3N_4 nanohybrid photocatalysts displayed obvious red-shift compared with pure CeO_2 ones.

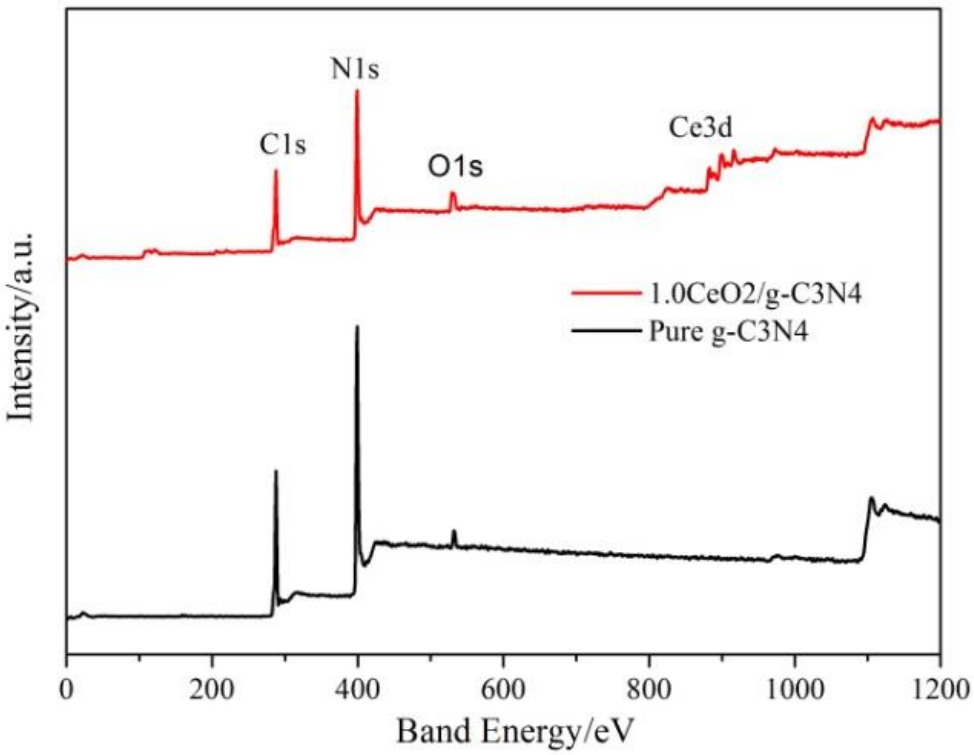

Figure 55 XPS survey spectra of g-C_3N_4 and mCeO_2/g-C_3N_4 nanohybrids.

XPS measurements were performed to explicate the valence states of various species. Figure 55 shows the survey scan XPS spectra of g-C_3N_4 and the mCeO_2/g-C_3N_4 (here m = 1.0) nanohybrid samples. The result indicates the presence of Ce, O, C, and N in the 1.0CeO_2/g-C_3N_4. High resolution spectra of Ce3d, O1s, C1s, and N1s are shown in Figure 56(a-d). The binding energy values of Ce $3d_{5/2}$ and Ce $3d_{3/2}$ are deconvolved into ten individual peaks (Ce(III) = v^0 + v' + u^0 + u' and Ce(IV) =v + v" + v"' + u + u" + u"', in Figure 56(a) only marked Ce(III)), which are very close to the XPS results provided by the literatures reported for CeO_2, suggesting the typical binding energies of cerium atom. However, the binding energy values of Ce $3d_{5/2}$ and Ce $3d_{3/2}$ in the 1.0CeO_2/g-C_3N_4 nanohybrids are observed at 884 eV and 902 eV, which are slightly lower than those for pure CeO_2. Such a shift may be attributed to the interaction between CeO_2 and g-C_3N_4. The O1s peak (Figure 56(b)) centered at 529.8 eV is associated with the O^{2-} in the CeO_2. The other three O1s peaks

(531.1eV, 533.4 eV and 534.2 eV) are associated with the presence of an –OH group, adsorbed H_2O and O_2 molecule on the surface of CeO_2/g-C_3N_4 nanohybrid photocatalysts. The C1s peak at 288.2 eV (Figure 56(c)) is assigned to a C–N–C coordination. The other C1s peak at 284.8 eV is attributed to the adventitious carbon on the surface of CeO_2/g-C_3N_4 nanohybrids. In the N1s spectrum (Figure 56(d)) several binding energies can be separated. The main N1s peak at a binding energy of 398.7 eV can be assigned to sp^2-hybridized nitrogen (C=N–C), thus confirming the presence of sp^2-bonded graphitic carbon nitride. The two peaks at 400.1 eV, 401.4 eV and 404.8 eV are attributed to tertiary nitrogen (N–$(C)_3$) groups, amino(-NH_2) function groups and the charging effects. Therefore, XPS investigation results confirmed the existence of both components in the nanohybrids heterojunction structure.

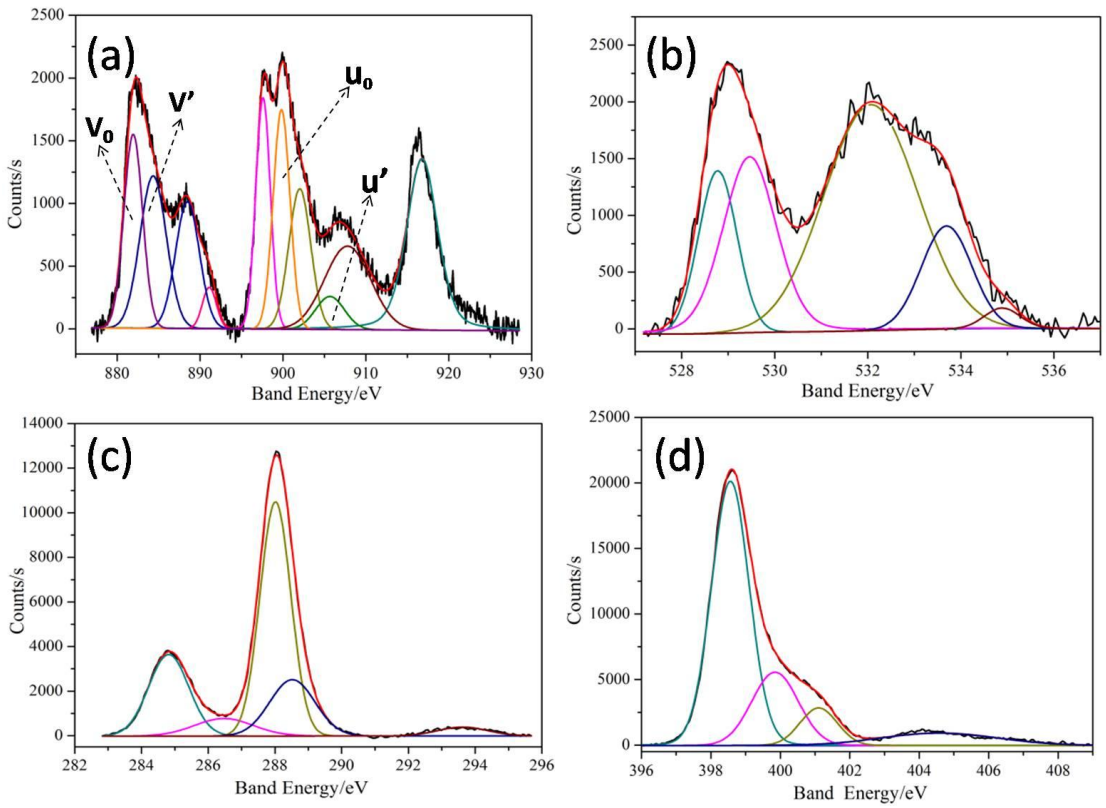

Figure 56 High resolution XPS spectra of 1.0CeO_2/g-C_3N_4 nanohybrids.

(a) Ce3d, (b) O1s, (c) C1s and (d) N1s.

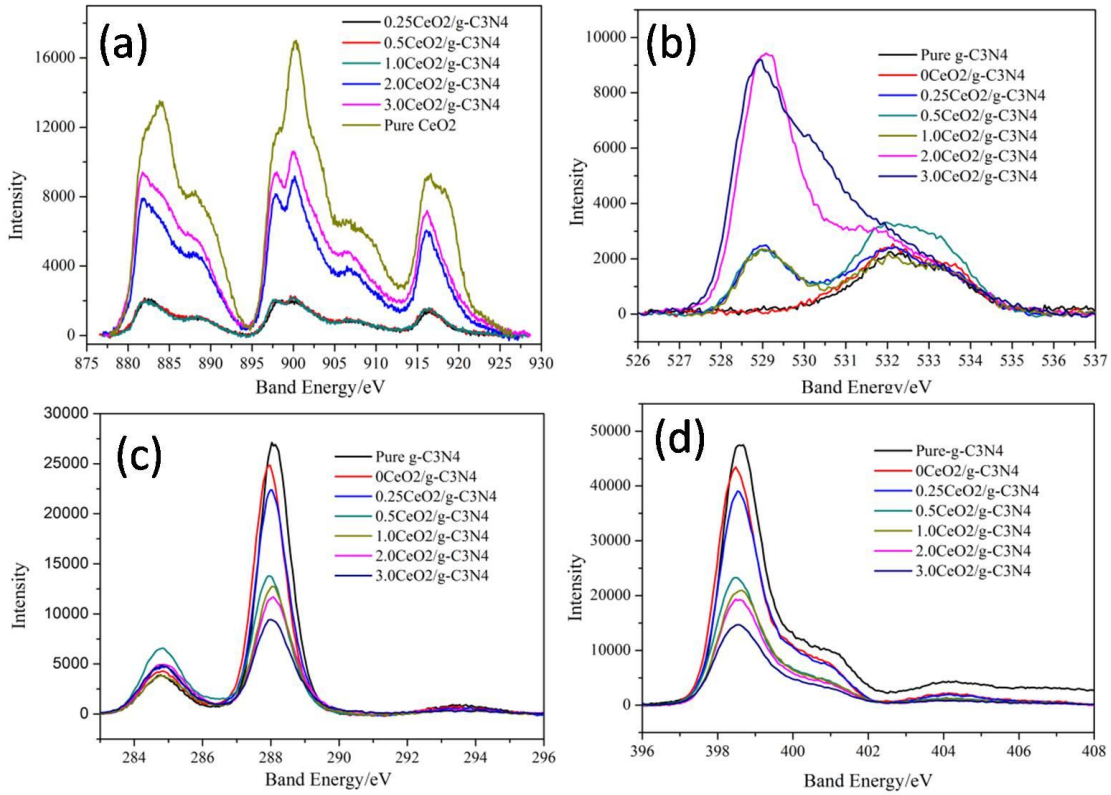

Figure 57 High resolution XPS spectra of $mCeO_2/g\text{-}C_3N_4$ nanohybrids.

(a) Ce3d, (b) O1s, (c) C1s and (d) N1s.

Figure 57(a-d) panels display the resolution spectra of $g\text{-}C_3N_4$ and $mCeO_2/g\text{-}C_3N_4$. It is found that the XPS signal intensity has a direct relationship with the component and content of the $CeO_2/g\text{-}C_3N_4$ nanohybrid photocatalysts. It can draw a conclusion that with increasing the addition contents of cerium salt precursor in this in-situ preparation process, the final obtained heterogeneous products show a enhancement XPS characteristic signal of Ce 3d and O 1s spectra, however, the XPS signals of C 1s and N 1s peaks become weaken dramatically, which is attributed to the gradual reduction of $g\text{-}C_3N_4$ exposed surface. An optimal coverage fraction and a better monodispersity of CeO_2 nanoparticles can be achieved of $1.0CeO_2/g\text{-}C_3N_4$ sample. Moreover, we can also obtain the C/N atom ratio of $g\text{-}C_3N_4$ as well as O/Ce, Ce^{3+}/Ce^{4+} atom ratio of CeO_2 by the corresponding integrated peak areas ratio. In this calcinations process, we should beware that different

elements are with different relative sensitivity factors (RSF). In this study, the RSF values of C1s, N1s, O1s and Ce 3d are 0.278, 0.477, 0.780 and 8.808, respectively. Herein, take pure g-C_3N_4 as an example, the total integrated area of N1s is 81083.28 and C1s is 32136.56 (deduced the area of adventitious carbon located at 284.6 eV), abridged as A_{C1s}, A_{N1s}. Therefore, the C/N atom ratio of pure g-C_3N_4 is as following: C/N atom% = $(A_{C1s}/RSF_{C1s})/(A_{N1s}/RSF_{N1s})$ =0.68. Besides, according the above equation, we also obtained the C/N atom ratio of g-C_3N_4 after ethanol/water hydrothermal at 160 ^{o}C, the C/N value is 0.73. Therefore, the as-prepared g-C_3N_4 is very close to the perfect g-C_3N_4 (its C/N atom ratio is 0.75). The amino groups (-NH_2) bonded on the edge of g-C_3N_4 network are easily deaminized under assistance of hydrothermal treatment, this point was also proved by the final basic solution (pH=8.28) and the evolution of NH_3 gas. On the other hand, the small g-C_3N_4 fragments with numerous defects and oligomers with relatively low molecular weight possess better solubility in ethanol/water solution and self-generated high pressure. By this way, the g-C_3N_4 with an approximately perfect structure would be realized. At the same time, Ce^{3+} mol% and CeO_2 weight ratios of mCeO_2/g-C_3N_4 hybrid photocatalysts are summarized in Table 2.

Table 2 Component analysis of mCeO_2/g-C_3N_4 nanohybrid photocatalysts

Items	[a]CeO_2wt%	[b]Ce^{3+}mol%
Pure CeO_2	100%	~15%
0.25CeO_2/g-C_3N_4	3.86wt%	31%
0.5CeO_2/g-C_3N_4	7.44wt%	35%
1.0CeO_2/g-C_3N_4	11.57wt%	35%
2.0CeO_2/g-C_3N_4	26.64wt%	23%
3.0CeO_2/g-C_3N_4	39.19wt%	20%

a: CeO_2 wt% obtained from TGA; b: Ce^{3+} mol% calculated from XPS

5.3.2.3 Photooxidation activity of $mCeO_2/g\text{-}C_3N_4$ nanohybrid photocatalysts

Figure 58 shows the photooxidation activity results. From Figure 58(a), we can conclude that the $1.0CeO_2/g\text{-}C_3N_4$ nanohybrid photocatalyst displayed the highest CO_2 generation concentration (740ppm;), showing nearly 5.8 times and 3.5 times higher activity than that of Pure $g\text{-}C_3N_4$ (128ppm) and Pure CeO_2 (211ppm) under visible light irradiation. From Figure 58(b), it can conclude that the $1.0CeO_2/g\text{-}C_3N_4$ photocatalyst also displayed the highest CO_2 generation concentration (840ppm;), showing nearly 3.7 times higher activity than that of Pure $g\text{-}C_3N_4$ (225ppm) under UV light irradiation. The photocatalytic performance improvement of $mCeO_2/g\text{-}C_3N_4$ is mainly attributed to following reasons. On condition of visible light irradiation, only $g\text{-}C_3N_4$ is visible light response, because the bandgap energy of CeO_2 is about 3.0eV. However, the photogenerated electrons of $g\text{-}C_3N_4$ can inject into CeO_2 surface because they established an intimate interfacial contact (Figure 59(a)). Then, the injected electrons are easily captured by the oxygen vacancies (Vo) bestrewed on CeO_2 surface (the concentration of Vo is in direct proportion with Ce^{3+} concentration), Thus the charge carriers could be separated efficiently, which was further confirmed by PL spectra, as shown in Figure 59(a), after in-situ hybridization with CeO_2 nanocrystals, the PL intensity of $g\text{-}C_3N_4$ was decreased greatly and show a small blue shift, this means the photogenerated carriers separation efficiency of $CeO_2/g\text{-}C_3N_4$ heterojunction photocatalysts was improved greatly. Namely, the photooxidation ability would be enhanced greatly by in-situ hybridization with appropriate content CeO_2 nanocrystals (herein, ca. 10 wt%); Under UV light irradiation, both materials can be photoexcited to establish a z-scheme type nanohybrid heterojunction by assistance of Ce^{3+}/Ce^{4+} fast cycling, greatly promoting to generated much more activated reaction species (such as $\cdot OH$, $\cdot O^{2-}$) to speed up photoredox reactions.

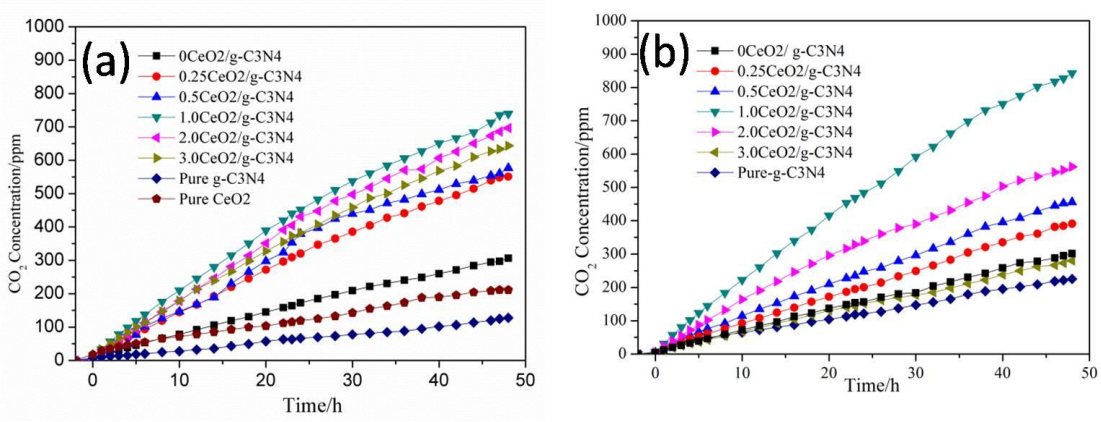

Figure 58 Photooxidation activity of CH_3CHO to CO_2 by $mCeO_2/g\text{-}C_3N_4$ nanohybrids. (a) Visible light (LED-435nm); (b) UV light (LED-365nm).

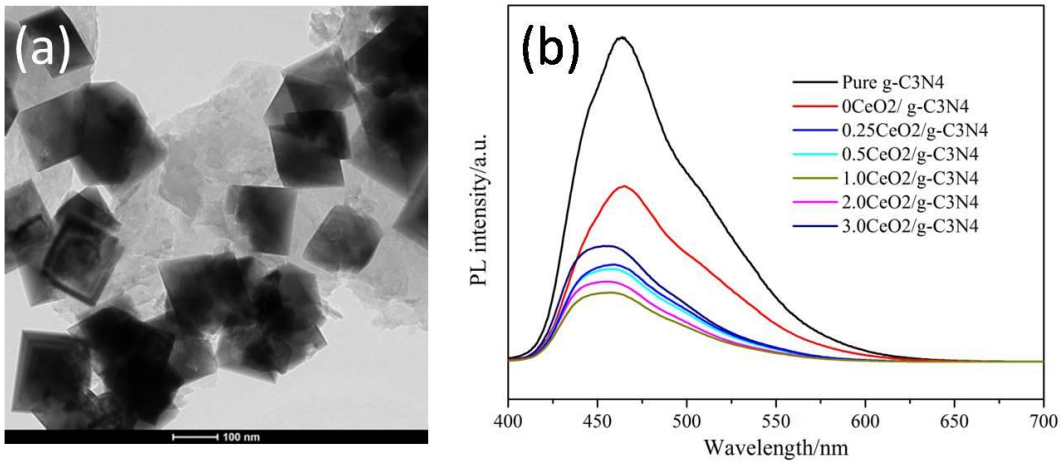

Figure 59 (a) HR-TEM image of $1.0CeO2/g\text{-}C_3N_4$ nanohybrids and (b) PL spectra of $mCeO_2/g\text{-}C_3N_4$ nanohybrids (excited at 365 nm).

Moreover, which had discussed before, the greatly enlarged S_{BET} (increased 3 times) as well as the appearance of numerous mesoporous (0.167cc/g) of g-C_3N_4 introduced by mixed solvothermal treatment is with better CH_3CHO adsorption ability. On the other hand, the relatively small octahedral CeO_2 NPs (54nm, 86nm, 87nm, 220nm and 203nm corresponding to m=0.25, 0.5, 1.0, 2.0 and 3.0) are with good monodispersity (as summarized in Table 3), More importantly, the octahedral CeO_2 nanoparticles have intimate contact with g-C_3N_4 substrate, which is beneficial to separate photogenerated holes and electrons efficiently. Therefore, much more photogenerated holes and electrons prefer to involve in the photocatalytic reaction rather than annihilate by the form of radiation. In summary, photooxidation performance of g-C_3N_4 under visible/UV light irradiation can be greatly promoted by hybridization with morphology controlled octahedral-CeO_2 nanocrystals, which is attributed to a synergistic effect of Ce^{3+}/Ce^{4+} fast redox reaction, intimate interfacial contact as well as relatively large specific surface area and mesoporosity derived from this novel CeO_2/g-C_3N_4 nanohybrid heterogeneous photocatalyst.

Table 3 Surface area and particle size of mCeO_2/g-C_3N_4 nanohybrids

Items	Pure g-C_3N_4	0CeO_2/g-C_3N_4	0.25CeO_2/g-C_3N_4	0.5CeO_2/g-C_3N_4	1.0CeO_2/g-C_3N_4	2.0CeO_2/g-C_3N_4	3.0CeO_2/g-C_3N_4	Pure CeO_2
Size	~um	~um	54 nm	86 nm	87 nm	220 nm	203 nm	>500 nm
S_{BET}	10.4m^2/g	31.9m^2/g	25.8m^2/g	32.5m^2/g	19.2m^2/g	15.9m^2/g	15.8m^2/g	4.9m^2/g

5.3.3 Other g-C_3N_4-based heterojunction nanohybrid photocatalysts

5.3.3.1 Structure and photocatalytic activity of $Bi_2O_2CO_3$/g-C_3N_4 nanohybrids

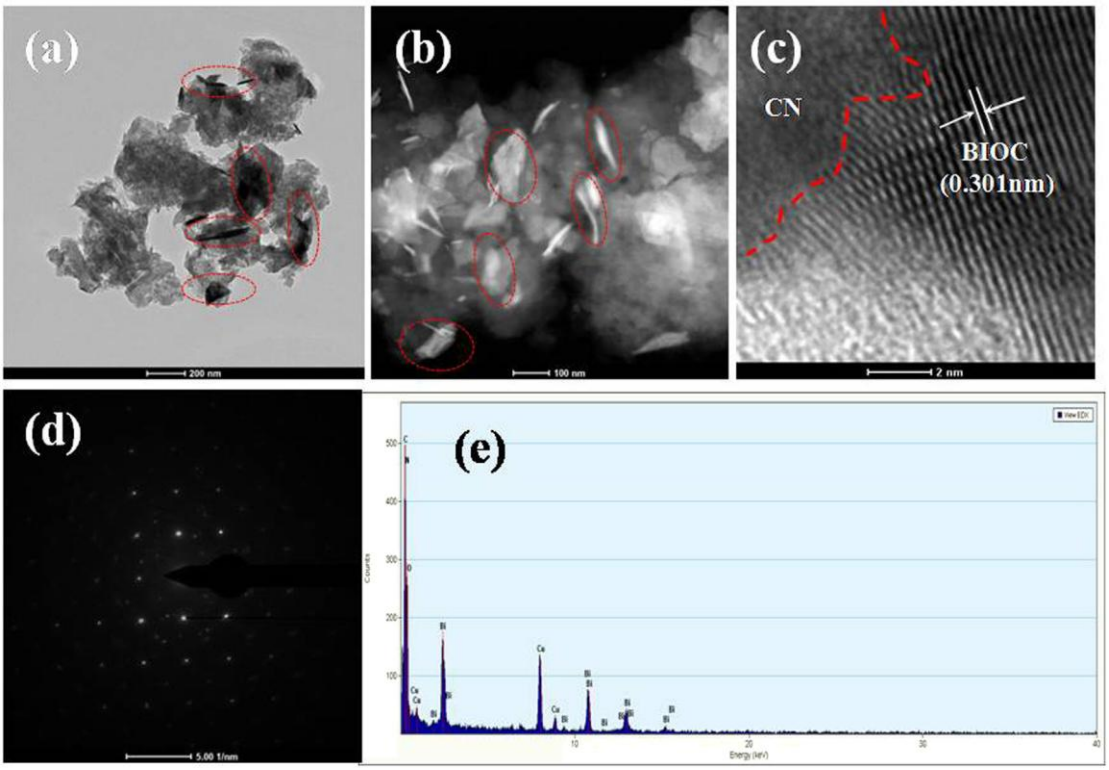

Figure 60 Morphology characterization of TEM (a), HAADF (b), HR-TEM (c), SAED (d) and EDX (e) for the 1.0BIOC-CN sample.

The results of characterization of surface morphology for 1.0$Bi_2O_2CO_3$/g-C_3N_4 nanosheet-based hybrids are provided in Figure 60. The dark parts in Figure 60(a) together with the bright parts in Figure 60(b), marked by red cycles, only presenting the $Bi_2O_2CO_3$ component. Meanwhile, the size of $Bi_2O_2CO_3$ after planetary milling treatment is about 20 nm, which is well consistence with results of XRD calculation. Therefore, after planetary milling treatment, BIOC nanosheets were indeed embedded into the flexible and multiporous g-C_3N_4 matrix to establish an intimated and well-defined heterojunction interfacial structure. The $Bi_2O_2CO_3$ nanosheets showed a single-crystal phase with exposed (103) facets (d_{space}=0.301 nm).

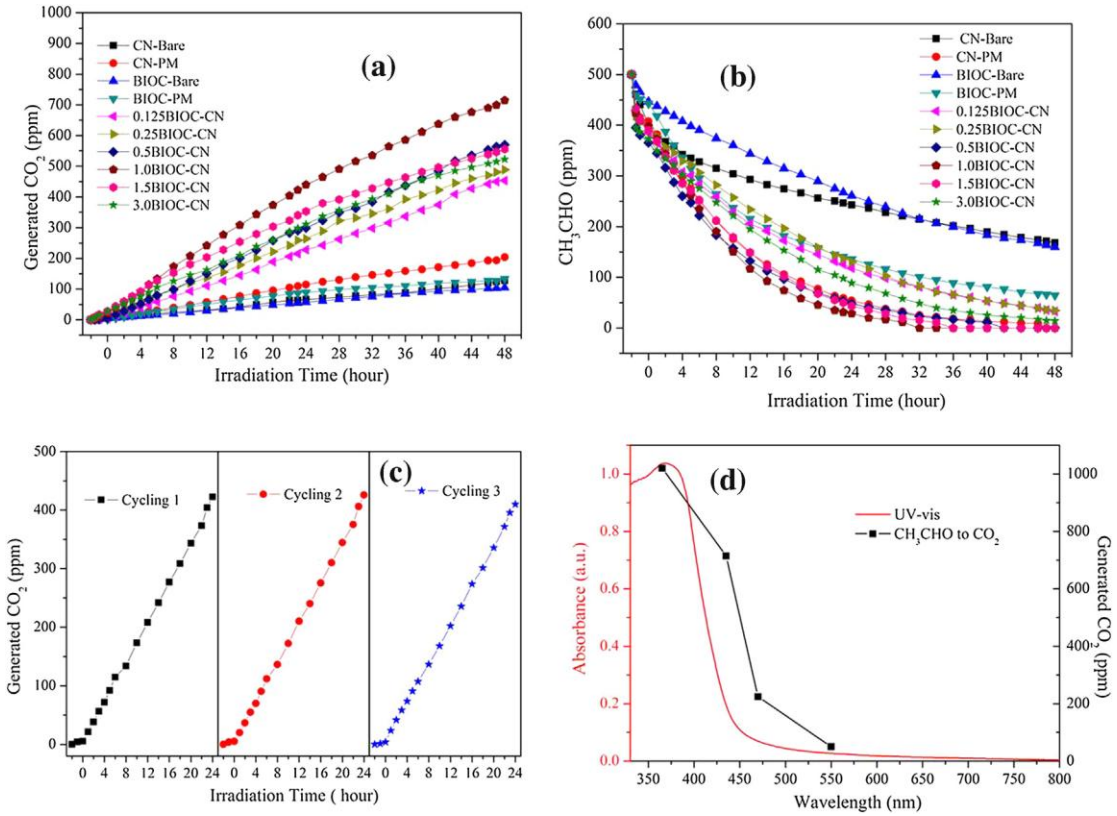

Figure 61. Results of photocatalytic activity for CH_3CHO degradation. (a) Time course of CO_2 evolution curves. (b) Time course of CH_3CHO concentration variation. (c) Three activity cycling tests by 1.0BIOC-CN. (d) Action spectra of the 1.0BIOC-CN sample.

Figure 61(a) showed the time courses of CO_2 evolution during the CH_3CHO degradation process. BIOC-Bare samples without planetary milling treatment showed extremely weak photooxidation ability for conversion CH_3CHO to CO_2, and only 105 ppm of CO_2 was generated after 48 hours of visible light irradiation, due to the small specific surface area and weak visible absorption ability. CN-Bare samples also presented weak CH_3CHO abatement capability (127ppm of CO_2 generated after 48h) because the strong recombination rate of photogenerated charge carriers in the bulk and the relatively slow adsorption on reaction active sites greatly impeded the enhancement of photocatalytic performance. The slow descending tendencies of CH_3CHO variation curves for BIOC-Bare and CN-Bare shown in Figure 61(b)

are the best circumstantial evidence of the above-mentioned inference. Results of blank experiments confirmed that the self-photolysis of CH_3CHO and self-photodecomposition of photocatalysts were both negligible. Planetary milling is an extremely foolproof approach for elevating the specific surface area and reaction sites. More importantly, it is also a super-practical but neglected way to establish heterojunction composite photocatalysts. Therefore, in this study, with the purpose of coupling these two photocatalysts, planetary milling treatment was used to fabricate a series of BIOC-CN heterojunction photocatalysts. Compared with CN-Bare and BIOC-Bare, the photooxidation ability to degrade CH_3CHO of all hybridized BIOC-CN photocatalysts were greatly enhanced, at least by 3 times, further illustrating the synergistic effect of these photocatalysts with layer-structure. Among the samples, the 1.0BIOC-CN sample showed the highest CO_2 evolution rate, generating 715 ppm of CO_2 after 48 h of visible light irradiation, which was 6.8 and 5.6 times higher than the rates by BIOC-Bare and CN-Bare, respectively. The recycle test and action spectra were also given in Figure 61(c,d).

Although the excellent photooxidation activity for gaseous CH_3CHO degradation has been proclaimed, the adaptability and efficacy of this BIOC-CN heterojunction photocatalyst in relieving liquid-phase contaminants still remain mysterious. Consequently, the two common water contaminants RhB and Cr (VI) were selected as model pollutants. The results of assessment are gathered in Figure 62(a-d). The rate of RhB degradation by the 1.0BIOC-CN was 4.0-times and 11.7-times faster than the rates by CN-Bare and BIOC-Bare, respectively. The activity of 1.0BIOC-CN for Cr (VI) photoreduction was 2.5-times and 8.8-times higher activity than the activities of CN-Bare and BIOC-Bare, respectively.

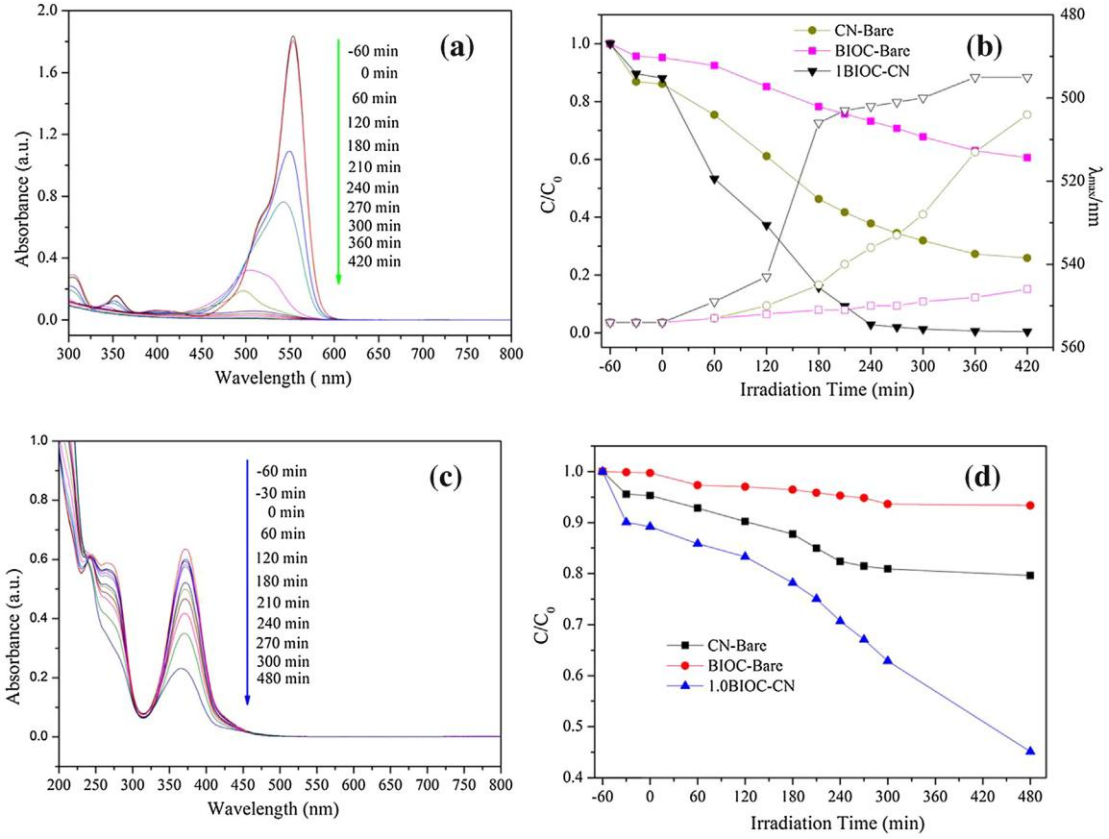

Figure 62. Results of photocatalytic activity for RhB and Cr (VI) degradation. (a) RhB and (c) Cr(VI) absorption spectra of 1.0BIOC-CN. (b) RhB and (d) Cr (VI) degradation curves over various samples.

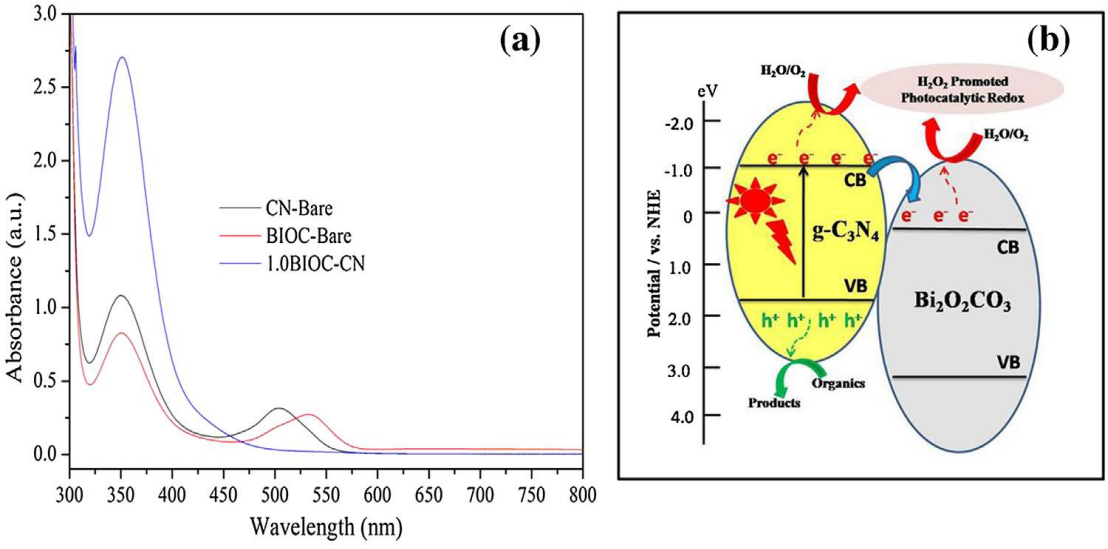

Figure 63 Absorption spectra of generated H_2O_2 during RhB degradation (a) and a proposed mechanism for photoactivity enhancement (b).

As shown in Figure 63(a), 92.09 μM of H_2O_2 was generated, an amount that is 3.28-times and 2.5-times larger than those generated by BIOC-Bare and CN-Bare, respectively. Since the redox potential of $H_2O/\cdot OH$ (E = 2.4 eV vs NHE) is much higher than the VB of g-C_3N_4, it is very difficult to generate ·OH in the BIOC-CN system, while $O_2/\bullet O^{2-}$ (E = -0.16 eV vs NHE) is prone to proceed. Actually, the generated H_2O_2 is a highly efficient intermediate with redox ability to further promote the improvement of photocatalytic activity, as proposed in the schematic illustration of Figure 63(b). Therefore, the dramatically enhanced photocatalytic performance of the BIOC-CN hybridized photocatalyst is finally attributed to a synergistic effect of established nanosheets/nanosheets heterojunction, enlarged S_{BET}/V_{pore} and high content of generated H_2O_2 ROS.

5.3.3.2 Structure and photocatalytic activity of NiO/g-C_3N_4 nanohybrids

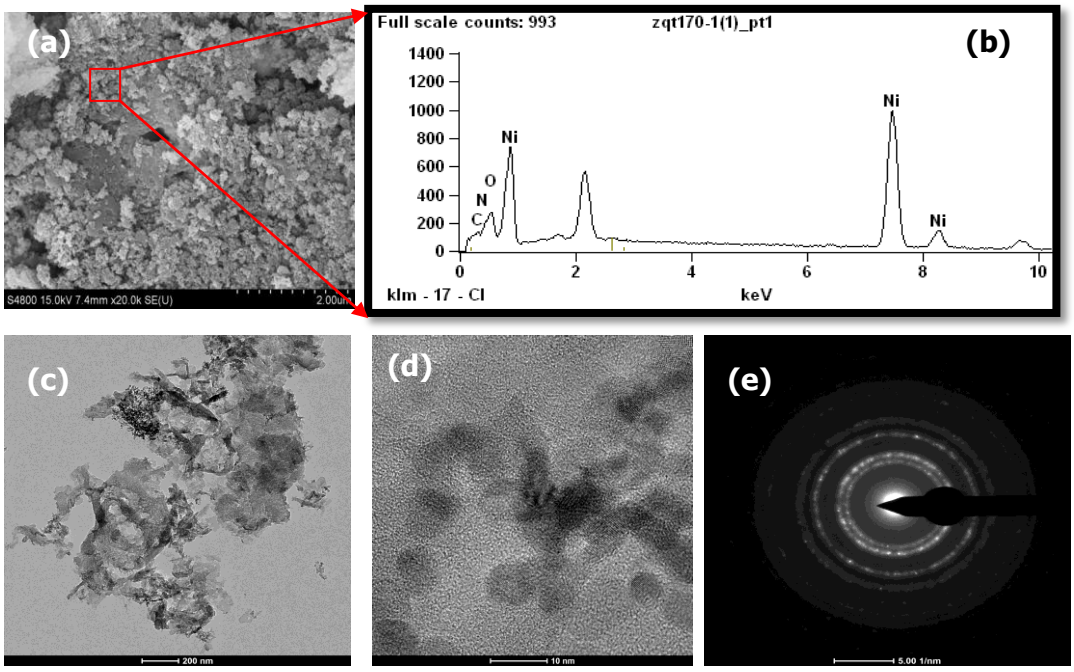

Figure 64 (a) SEM image; (b) EDS spectra; (c) HR-TEM image; (d) HR-TEM image; (e) SAED pattern for 1.0NiO@g-C_3N_4 nanohybrids.

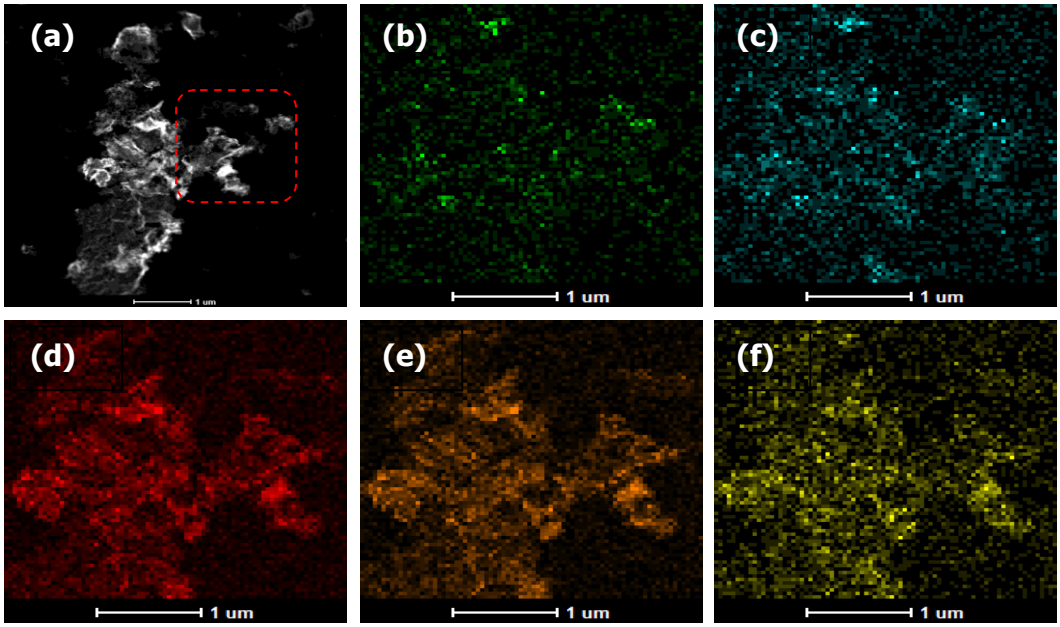

Figure 65 EDS-Mapping images of 1.0NiO@g-C_3N_4. (a)HAADF; (b-c)Ni-K/L; (d)C-K; (e)N-K; (f)O-K.

The shape and size information of the in-situ prepared 1.0NiO@g-C_3N_4 hybrid photocatalysts were obtained by HR-TEM, as shown in Figure 64. In order to further visualize the distribution of NiO nanoparticles on g-C_3N_4 surface, EDS elemental mapping technique was adopted, the results are shown in Figure 65. Figure 65(a) is high angle annular dark filed (HAADF) image, by using a STEM and a high-angle detector, it is possible to form atomic resolution images where the contrast is directly related to the atomic number (z-contrast image). The directly interpretable z-contrast image makes STEM imaging with a high-angle detector appealing. This is in contrast to the conventional high resolution electron microscopy technique, which just uses phase-contrast, and therefore produces results which need interpretation by simulation. Specifically, the contrast intensity of HAADF is in direct proportion to the square value of atomic number. Therefore, we can draw the conclusion that NiO nanoparticles in-situ grown on margin of g-C_3N_4 surface, which is a supplementary instruction of above-mentioned viewpoint.

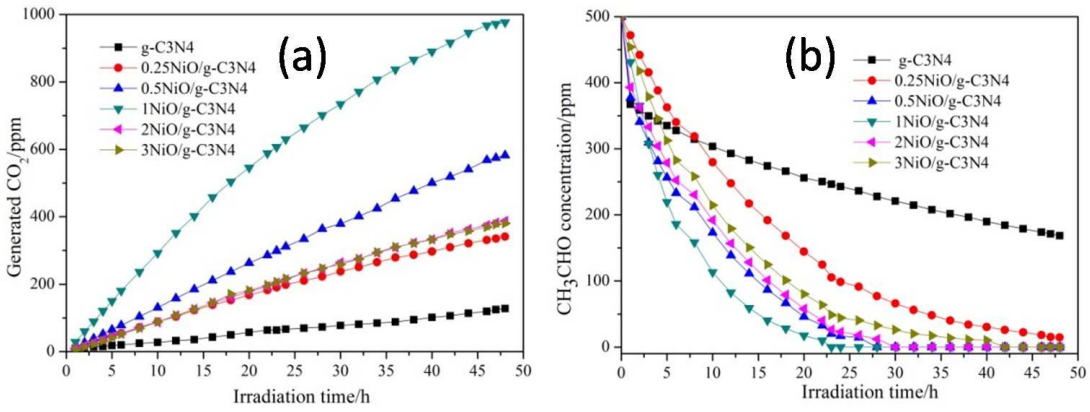

Figure 66 Photooxidation activity evaluation of NiO/g-C_3N_4 nanohybrids.

(a) CO_2 evolution curves; (b) CH_3CHO concentration variation.

Figure 66 shows the photooxidation activity evaluation results. From Figure 66(a), we can conclude that the 1.0NiO/g-C_3N_4 nanohybrid photocatalyst displayed the highest CO_2 generation concentration (977ppm), showing nearly 7.6 times higher activity than that of Pure g-C_3N_4 (128ppm). The photocatalytic performance improvement of mNiO/g-C_3N_4(at least increased 2.7 times) are mainly attributed to two reasons. On the one hand, the greatly enlarged S_{BET} (increased 9 times than g-C_3N_4 bulk counterpart) as well as the appearance of numerous mesoporous of g-C_3N_4 introduced by mixed solvothermal treatment are with better CH_3CHO adsorption ability. On the other hand, the relatively small NiO NPs (ca. 10nm corresponding to 1.0NiO/g-C_3N_4) are with good monodispersity, More importantly, the anchored p-type NiO nanoparticles have intimate contact with n-type g-C_3N_4 substrate, which is beneficial to establish a p/n heterojunction interface to separate photogenerated holes and electrons efficiently. Therefore, much more photogenerated holes and electrons prefer to involve in the photocatalytic reaction rather than annihilate by the form of radiation. In summary, photooxidation performance of g-C_3N_4 under visible light irradiation can be greatly promoted by incorporation with in-situ grown NiO nanoparticles.

5.3.3.3 Structure and photocatalytic activity of CeO_2/CN-Rods nanohybrids

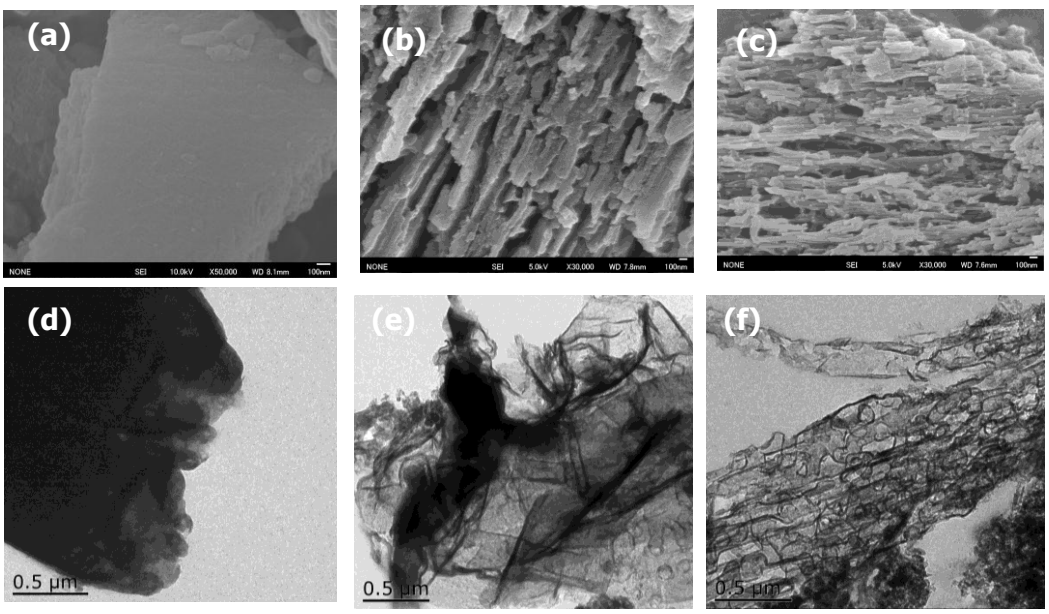

Figure 67 SEM&TEM images: (a,d) CN Bare; (b,e,f)Se-CN; (c)0.5CeO_2@Se-CN

The surface information and textural structure of as-prepared samples are displayed in Figure 67. Figure 67(a,d) indicated that g-C_3N_4 prepared without copolymerizing with Se monomer displayed numerous sheets-stacked bulks with an extremely smooth surface. When selenium powder was introduced into the melamine substrates, the generated g-C_3N_4 2D sheets were partially exfoliated to be rod-like nano-arrays as well as Se-CN nanosheets with only a few layers (shown in Figure 67(b,e,f)). Meanwhile, in Figure 67(c), it can be observed that in-situ grown octahedral CeO_2 nanocrystals with good monodispersity (particle size around 100 nm) as well as good crystallinity were successfully fabricated on Se-CN nanorod substrate on condition that appropriate cerium salt mole ratio was adopted. The formation mechanism of Se-CN and CeO_2/CN-Rods (or named by CeO_2@Se-CN) was similar with CeO_2/g-C_3N_4 above-mentioned.

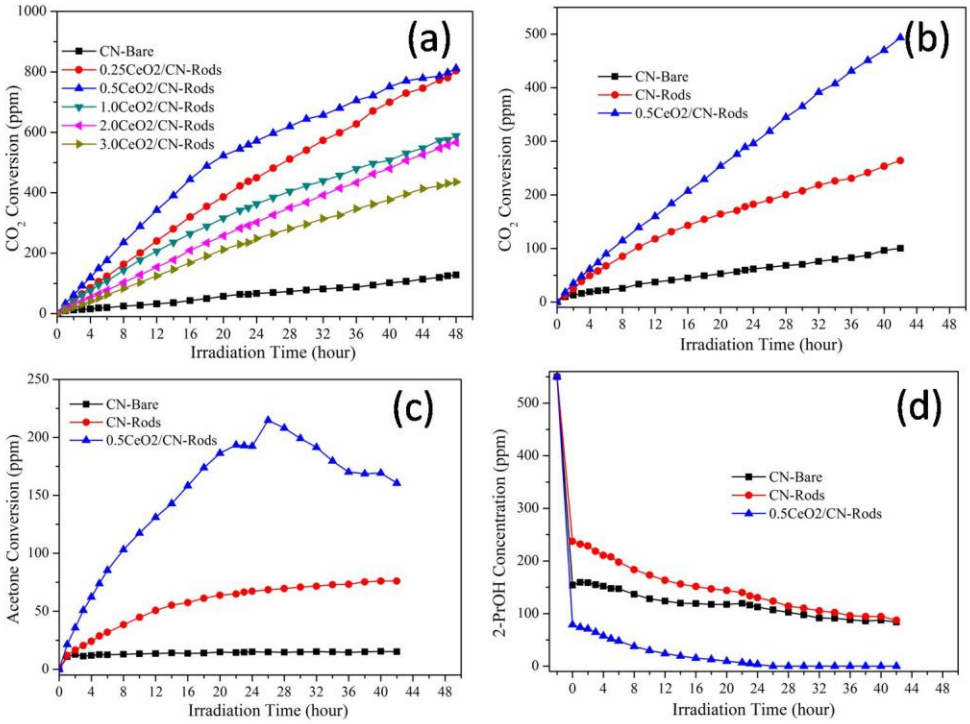

Figure 68 Photooxidation activities by CeO_2/CN-Rods nanohybrids. (a) CH_3CHO conversion to CO_2, (b) 2-PrOH conversion to CO_2, (c) 2-PrOH conversion to acetone and (d) 2-PrOH concentration variations.

As given in Figure 68, both gaseous CH_3CHO and 2-PrOH were adopted as model pollutions to evaluate the photooxidation activities of CeO_2/g-C_3N_4 nanohybrids. With respect to CN-Bare, the photooxidation activity for CH_3CHO degradation by 0.5CeO_2/g-C_3N_4 nanohybrids was enhanced 8 times. As to 2-PrOH photooxidation, the activity to produce CO_2 was enhanced 5 times, while the selectivity activity for acetone generation was enhanced as high as 10.6 times. The promotion mechanism was proposed in Figure 69.

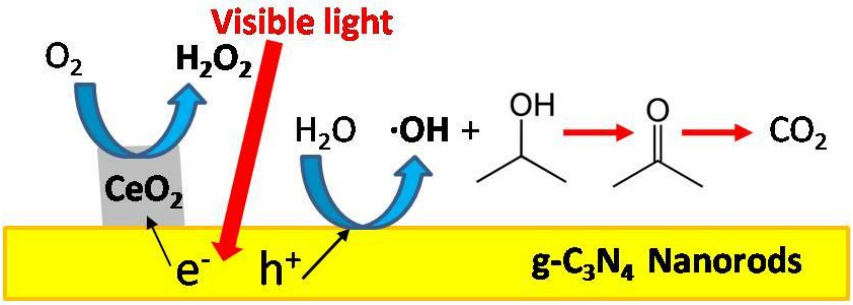

Figure 69 Proposed mechanism for 2-PrOH photooxidation by CeO_2/CN-Rods.

Table 4 Summary of CO_2 PEC reduction by CeO_2/CN-Rods nanohybrids

		H_2		CO		
Cocatalyst	Coulomb (C)	Content (μmol)	F.E. (%)	Content (μmol)	F.E. (%)	Total F.E. (%)
g-C_3N_4	0.0180	0.005	5.35	n.d.	--	5.35
Se-CN	0.0216	0.021	18.81	0.005	4.78	23.59
CeO_2@Se-CN	0.0360	0.040	21.32	0.017	8.92	30.24
Cu	0.0144	0.026	34.35	0.025	33.90	68.25
Au	0.0072	0.027	71.88	0.005	13.83	85.71
Pt	0.0072	0.020	53.53	0.004	10.93	64.46
Pd	0.0036	0.013	66.90	0.003	16.95	83.85
Rh	0.0540	0.132	47.28	0.099	35.68	82.96
Ag	0.0108	0.017	29.74	0.011	18.73	48.47
Mo	0.0054	0.011	38.66	0.005	16.65	55.31
Ni	0.0054	0.011	37.77	0.005	17.34	55.11

As summarized in Table 4, the low faradic efficiency values of CN Bare electrodes indicates that the inferior PEC CO_2 reduction performance as well as weak PEC H_2O splitting ability. After Selenium exfoliation and CeO_2 in-situ growing on g-C_3N_4, better photoelectric response and long-range stability for CO_2 PEC reduction to CO were achieved, which is possibly attributed to the formation of CeO_2 and Se-CN heterojunction (built-in electric filed formation). The nanohybrid heterojunction greatly promotes the efficient separation of photogenerated electron-hole pair. Besides, with the aid of metal cocatalyst deposition on CeO_2@Se-CN surface, PEC water splitting and CO_2 reduction can both be further promoted, because metal cocatalysts are typically with good electrons transportation rate and numerous activated reaction sites. To sum up, the in-situ anchored CeO_2 nanoparticles on Se-CN substrate to fabricate a hierarchical structure hybrid photocatalysts can greatly promote CO_2 photoelecrochemical reduction to CO products. Meanwhile, good CO selectivity from CO_2 PEC reduction can be achieved with appropriate metal deposition (such as Cu and Rh), while loading noble metals such as Pt, Au, Pt are beneficial for water-splitting to produce hydrogen gas.

5.3.4 Novel Melem-based nanohybrid heterojunctions photocatalysts

5.3.4.1 Morphology characterization of mCeO$_2$-Melem

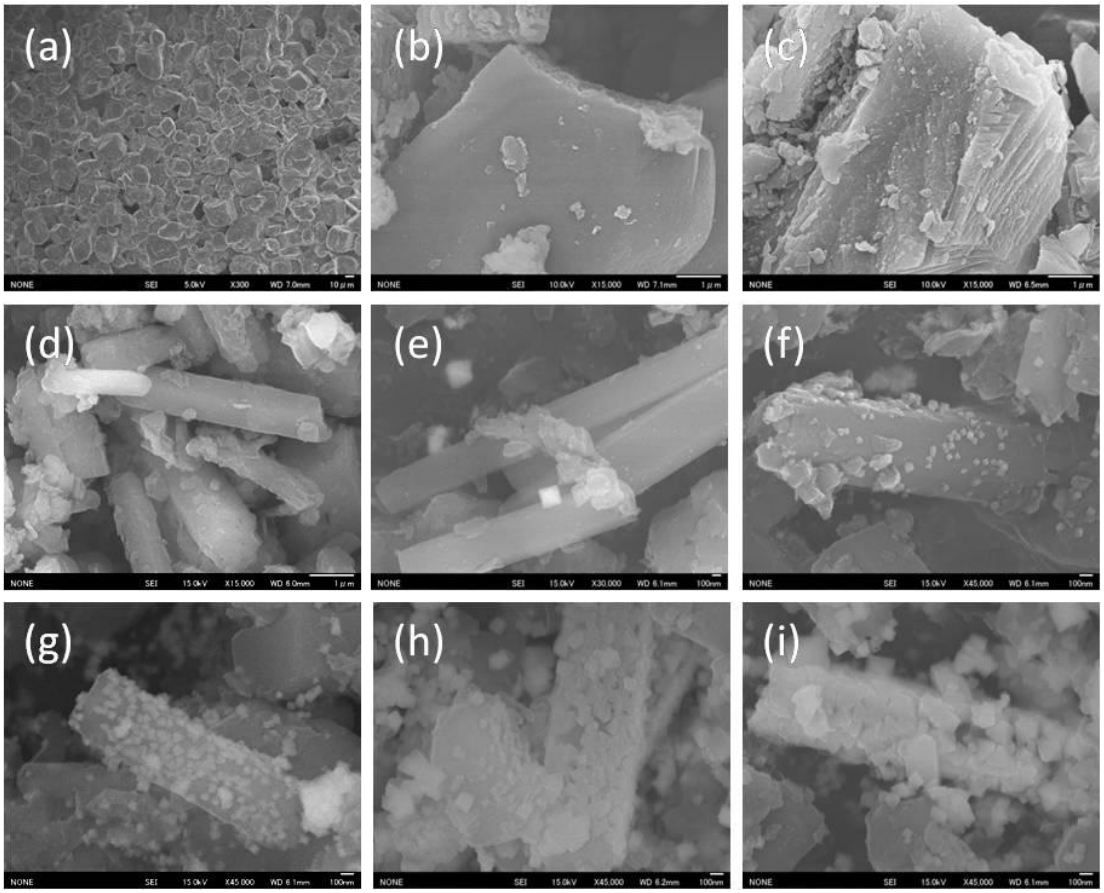

Figure 70 SEM images of CN prepared at different conditions. (a) Melamine precursor; (b) CN-Bare; (c) Melem-Bare; (d) Melem-ST; (e) 0.25CeO$_2$-Melem; (f) 0.5CeO$_2$-Melem; (g) 1.0CeO$_2$-Melem; (h) 2.0CeO$_2$-Melem and (i) 3.0CeO$_2$-Melem. The scale bar is 10 μm in (a), 1μm in (b-d) and 100 nm in (e-i).

Figure 70(a) shows the morphology information of Melamine precursor. It presents bulk-like texture structure with tens of microns size. Figure 70(b) indicated that CN-Bare displayed numerous sheets-stacked bulks with an extremely smooth surface. By observation of SEM images of Melem-Bare in Figure 70(c), the generated 2D sheets showed a resemble morphology with CN-Bare because of the incompletely polycondensation of melamine precursor. Namely, the as-prepared Melem-Bare produced at 450 °C comprised a mixture

of melem oligomers with different low-molecule-weight intermediates. However, it is worth to noting that with ethanol/water solvothermal treatment the bulk-like morphology was completely converted to rod-like with a big aspect ratio, meanwhile, the dimensional size was also reduced to several hundred nanometers. Such structure can not only provide much more active sites for redox reaction, but also beneficial to separate photogenerated electrons and holes (a shorter e^-/h^+ diffusion and transfer distance than bulk material). By comparison of Figure 70(e-i), with increasing the addition content of cerium (III) salt, the surface of rod-like melem was gradually anchored by the in-situ grown octahedral CeO_2 nanocrystals.

5.3.4.2 Structure characterization of mCeO_2-Melem

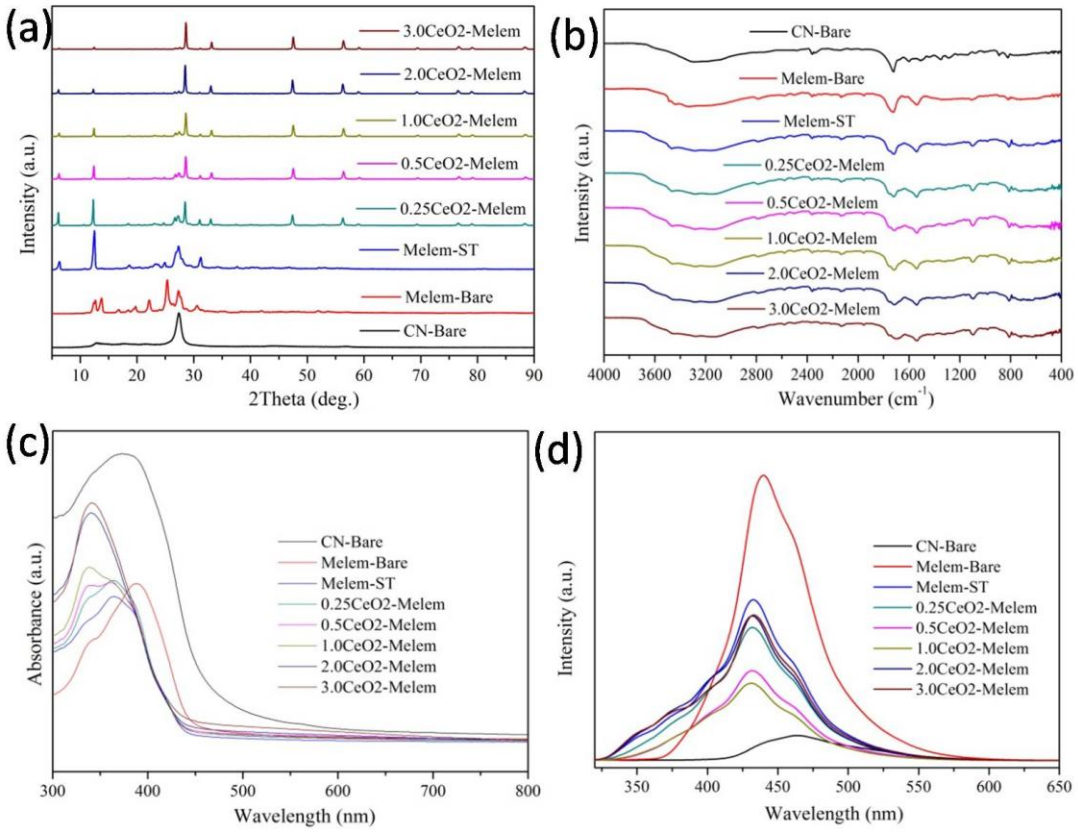

Figure 71 Structure characterization of CeO_2-Melem nanohybrids.

(a) XRD; (b) FTIR; (c) UV-vis and (d) PL;

Figure 71 shows various measurement results to probe its structure information. From XRD patterns (Figure 71(a)), two peaks at 13.1° and 27.4° in CN-Bare sample represent (100) and (002) diffraction planes (JCPDS 87-1526). As to Melem-Bare sample, the characteristic peaks can be fully ascribed to the melem oligomers. Assisting by solvothermal treatment, the melem oligomers (Melem-Bare) are almost converted to melem monomers with high purity (named Melem-ST), which shows much more efficiency and time-saving advantage than reported DMSO soluble method[190] (*JACS, 2015, 137, 1064-1072*). Because the ethanol/water solvothermal treatment adopted in our study is an effective way to tailor melem oligomers into melem monomers with increasing amino-groups (as shown in Figure 71(b)). The diffraction peaks of melem in mCeO_2-Melem hybrids reduced gradually, which is attributed to the anchored CeO_2 on its surface. From the optical absorption spectra of Figure 71(c), melem-based hybrid photocatalysts present blue-shift by comparison with CN-Bare counterpart. The maximum absorption wavelength of melem-based hybrids alters from 600 nm to 450 nm. Moreover, from PL spectra, it can draw the conclusion that melem-based photocatalysts possess greater ability to produce photogenerated charge carriers than typical g-C_3N_4 counterparts. Besides, by anchoring CeO_2 nanocrystals on melem surface by in-situ grown approach can further promote the separation of photogenerated holes and electrons, as depicted in Figure 71(d).

5.3.4.3 Activity evaluation of mCeO_2-Melem

The time course of acetaldehyde (CH_3CHO) degradation to CO_2 under visible light irradiation by this novel CeO_2-Melem nanohybrid photocatalysts were displayed in Figure 72. Compared with CN-Bare, the photooxidation activity of Melem-ST was enhanced 4 times. After introducing in-situ grown CeO_2 on melem, the photooxidation activity can be further greatly promoted,

by 8-times up. From action spectra in Figure 72(c), the 1.0CeO_2-Melem nanohybrid presents good optical response property, indicating that it is a real photocatalytic process. The enhancement of photocatalytic activity can't be ascribed to the change of S_{BET} and optical absorption. The proposed mechanism needs further investigated.

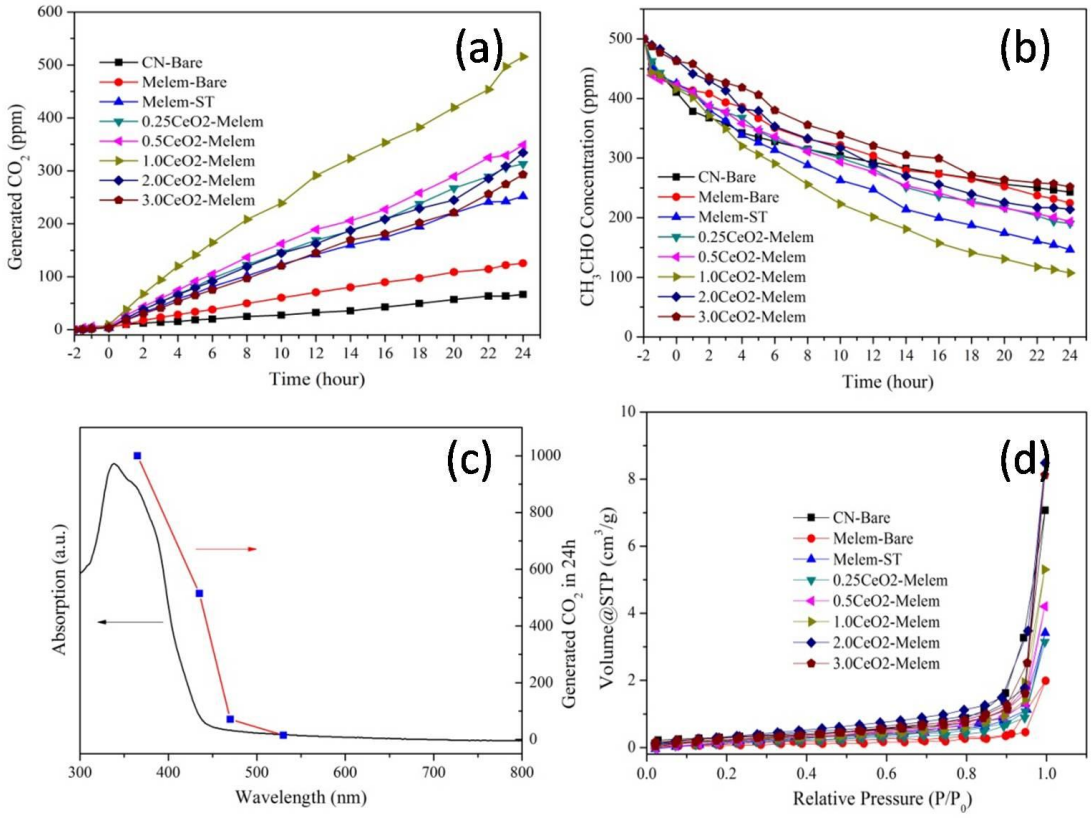

Figure 72 Activity evaluation of CH_3CHO degradation by CeO_2/Melem nanohybrids. (a) CO_2 evolution curves, (b) CH_3CHO concentration variation, (c) Action spectra and (d) BET isotherm.

5.4 Conclusions

In this section, a series of novel g-C_3N_4-based and melem-based nanohybrid heterojunction photocatalysts were successfully prepared by in-situ grown method, such as CeO_2/g-C_3N_4, $Bi_2O_2CO_3$/g-C_3N_4, NiO/g-C_3N_4, CeO_2/CN-rods and CeO_2/Melem. The above nanohybrid photocatalysts present superior activity than g-C_3N_4 bulks in RhB degradation, Cr (VI) photoreduction,

CH_3CHO degradation, 2-PrOH photooxidation and CO_2 PEC reduction. In detail, morphology controlled CeO_2 nanocrystals have been proved to be an excellent promoter to facilitate the photooxidation activity enhancement of g-C_3N_4 by establishing an efficient heterojunction (as given in Figure 73). Most importantly, an especially cost-effective way to purifying melem was also established. The optimal hybrid 1.0CeO_2-Melem presents an extremely high efficiency for charge carriers separation, thus exhibits a much superior activity in CH_3CHO degradation, increasing 8-times higher than g-C_3N_4 counterpart.

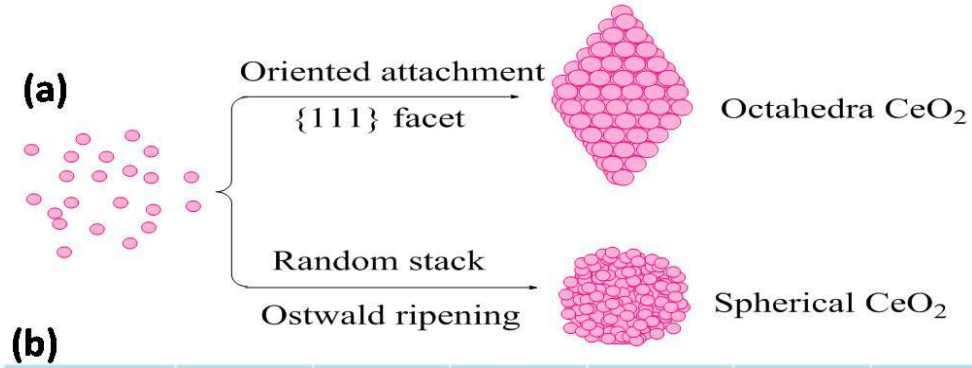

(b)

Entry	A	B	C	D	E	F
EtOH:H_2O/ml	40:0	30:10	20:20	17:23	10:30	0:40
Size/nm	80	100	200	250	400	500-600
Shape	sphere	sphere	Sphere-Octahedron	Octahedron	Octahedron	sphere
Monodispersity	○	◎	△	◎	○	△

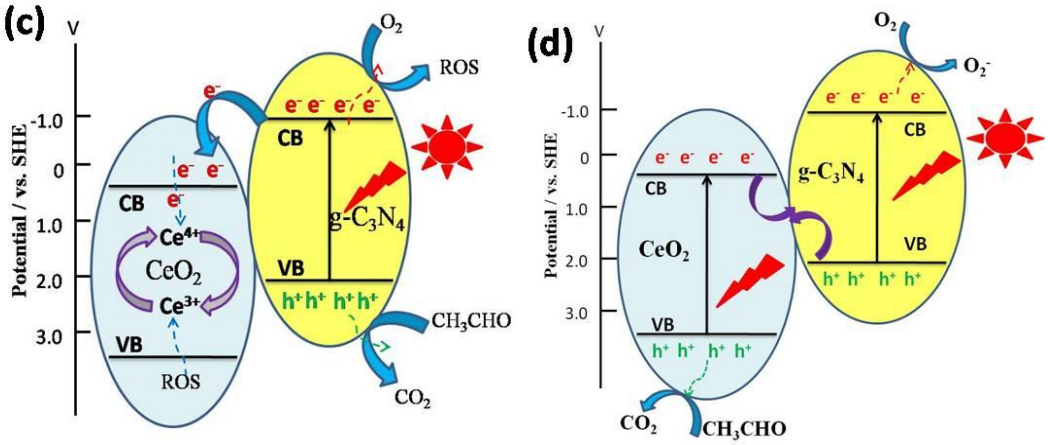

Figure 73 (a) Formation routes of CeO_2 nanocrystals, (b) Morphology controlled CeO_2 preparation by tuning ethanol/water ratio and photocatalytic mechanism of CeO_2/g-C_3N_4 nanohybrids (c) under visible light irradiation and (d) under UV light irradiation.

Chapter 6 General Conclusions

In this study, g-C_3N_4 bulks (CN-Bare) were prepared by conventional melamine thermal polycondensation approach. CN-Bare sample really presented extremely weak photooxidation ability. Then, three physicochemical modification approaches were investigated: planetary milling, hydrothermal treatment and selenium assisted exfoliation. The as-prepared g-C_3N_4 samples were denoted as CN-PM, CN-HT and CN-Rods, respectively. And their photooxidation activities showed 2-6 times higher than CN-Bare. Particularly, the morphology of g-C_3N_4 can vastly altered from bulk-like to nanorod arrays by selenium assisted exfoliation (CN-Rods). Such structural modified CN-Rods displayed superior photocatalytic performance (about 6 times up) than that of CN-Bare. And then, bandgap engineering was adopted to further promote the optical absorption of visible light by g-C_3N_4 by a facile two-step thermal treatment. Fascinatingly, the optical absorption edge of g-C_3N_4 was extended from 460 nm to 650 nm. In the last section, we adopted morphology-controlled CeO_2 nanocrystals to fabricate a series of CeO_2/g-C_3N_4 nanohybrids in order to further boost the photocatalytic activity of g-C_3N_4. It is noteworthy that the intimate degree of established heterojunctions between CeO_2 and g-C_3N_4 affect the photooxidation activity tremendously. The in-situ grown CeO_2 nanocrystals on g-C_3N_4 (mCeO_2/g-C_3N_4) achieved much better activity than CN-Bare (increased 8 times higher), which is attributed to the better separation efficiency of charge carriers. Besides, the pretty good versatility and expansibility of this in-situ grown other metal oxides (NiO, and $Bi_2O_2CO_3$) on g-C_3N_4 to obtain various novel g-C_3N_4-based nanohybrid photocatalysts were well-founded confirmed. Moreover, especially cost-effective way to purifying melem was also established. The optimal hybrid 1.0CeO_2-Melem presents an extremely high efficiency for charge carriers separation, thus exhibits a much superior activity in CH_3CHO degradation, increasing 8-times higher than CN-Bare.

References

(1) Obama, B.: The irreversible momentum of clean energy. *Science* 2017. DOI: 10.1126/science.aam6284.

(2) Turchi, C. S.; Ollis, D. F.: Photocatalytic degradation of organic water contaminants: Mechanisms involving hydroxyl radical attack. *Journal of Catalysis* 1990, *122*, 178-192.

(3) Sayama, K.; Arakawa, H.: Photocatalytic decomposition of water and photocatalytic reduction of carbon dioxide over zirconia catalyst. *The Journal of Physical Chemistry* 1993, *97*, 531-533.

(4) Hoffmann, M. R.; Martin, S. T.; Choi, W.; Bahnemann, D. W.: Environmental Applications of Semiconductor Photocatalysis. *Chemical Reviews* 1995, *95*, 69-96.

(5) Varghese, O. K.; Paulose, M.; LaTempa, T. J.; Grimes, C. A.: High-Rate Solar Photocatalytic Conversion of CO2 and Water Vapor to Hydrocarbon Fuels. *Nano letters* 2009, *9*, 731-737.

(6) Chen, X.; Shen, S.; Guo, L.; Mao, S. S.: Semiconductor-based Photocatalytic Hydrogen Generation. *Chemical Reviews* 2010, *110*, 6503-6570.

(7) Wang, C.; Xie, Z.; deKrafft, K. E.; Lin, W.: Doping Metal–Organic Frameworks for Water Oxidation, Carbon Dioxide Reduction, and Organic Photocatalysis. *Journal of the American Chemical Society* 2011, *133*, 13445-13454.

(8) Fujishima, A.; Honda, K.: Electrochemical Photolysis of Water at a Semiconductor Electrode. *Nature* 1972, *238*, 37-38.

(9) Roy, S. C.; Varghese, O. K.; Paulose, M.; Grimes, C. A.: Toward Solar Fuels: Photocatalytic Conversion of Carbon Dioxide to Hydrocarbons. *ACS Nano* 2010, *4*, 1259-1278.

(10) Zhang, H.; Lv, X.; Li, Y.; Wang, Y.; Li, J.: P25-Graphene Composite as a High Performance Photocatalyst. *ACS Nano* 2010, *4*, 380-386.

(11) Chen, X.; Liu, L.; Yu, P. Y.; Mao, S. S.: Increasing Solar Absorption for Photocatalysis with Black Hydrogenated Titanium Dioxide Nanocrystals. *Science* 2011, *331*, 746-750.

(12) Tong, H.; Ouyang, S.; Bi, Y.; Umezawa, N.; Oshikiri, M.; Ye, J.: Nano-photocatalytic Materials: Possibilities and Challenges. *Advanced Materials* 2012, *24*, 229-251.

(13) Yu, J.; Low, J.; Xiao, W.; Zhou, P.; Jaroniec, M.: Enhanced Photocatalytic CO2-Reduction Activity of Anatase TiO2 by Coexposed {001} and {101} Facets. *Journal of the American Chemical Society* 2014, *136*, 8839-8842.

(14) Bao, J.; Zimmler, M. A.; Capasso, F.; Wang, X.; Ren, Z. F.: Broadband ZnO Single-Nanowire Light-Emitting Diode. *Nano letters* 2006, *6*, 1719-1722.

(15) Zhang, H.; Chen, G.; Bahnemann, D. W.: Photoelectrocatalytic materials for environmental applications. *Journal of Materials Chemistry* 2009, *19*, 5089-5121.

(16) Wang, J.; Wang, Z.; Huang, B.; Ma, Y.; Liu, Y.; Qin, X.; Zhang, X.; Dai, Y.: Oxygen Vacancy Induced Band-Gap Narrowing and Enhanced Visible Light Photocatalytic Activity of ZnO. *ACS applied materials & interfaces* 2012, *4*, 4024-4030.

(17) Wang, H.; Dou, K.; Teoh, W. Y.; Zhan, Y.; Hung, T. F.; Zhang, F.; Xu, J.; Zhang, R.; Rogach, A. L.: Engineering of Facets, Band Structure, and Gas-Sensing Properties of Hierarchical Sn2+-Doped SnO2 Nanostructures. *Advanced Functional Materials* 2013, *23*, 4847-4853.

(18) Wang, H.; Rogach, A. L.: Hierarchical SnO2 Nanostructures: Recent Advances in Design, Synthesis, and Applications. *Chemistry of Materials* 2014, *26*, 123-133.

(19) Mishima, T.; Matsuda, M.; Miyake, M.: Visible-light photocatalytic properties and electronic structure of Zr-based oxynitride, Zr2ON2, derived from nitridation of ZrO2. *Applied Catalysis A: General* 2007, *324*, 77-82.

(20) Shifu, C.; Sujuan, Z.; Wei, L.; Wei, Z.: Preparation and activity evaluation of p–n junction photocatalyst NiO/TiO2. *Journal of Hazardous Materials* 2008, *155*, 320-326.

(21) Vahini, R.; Kumar, P. S.; Karuthapandian, S.: Bandgap-tailored NiO nanospheres: an efficient photocatalyst for the degradation of crystal violet dye solution. *Applied Physics A* 2016, *122*, 744.

(22) Wang, X.; Maeda, K.; Thomas, A.; Takanabe, K.; Xin, G.; Carlsson, J. M.; Domen, K.; Antonietti, M.: A metal-free polymeric photocatalyst for hydrogen production from water under visible light. *Nat Mater* 2009, *8*, 76-80.

(23) Ong, W.-J.; Tan, L.-L.; Ng, Y. H.; Yong, S.-T.; Chai, S.-P.: Graphitic Carbon Nitride (g-C3N4)-Based Photocatalysts for Artificial Photosynthesis and Environmental Remediation: Are We a Step Closer To Achieving Sustainability? *Chemical Reviews* 2016, *116*, 7159-7329.

(24) Liebig, J. V.: About Some Nitrogen Compounds. *Ann. Pharm.* 1984, *10*, 10.

(25) Franklin, E. C.: THE AMMONO CARBONIC ACIDS. *Journal of the American Chemical Society* 1922, *44*, 486-509.

(26) Pauling, L.; Sturdivant, J. H.: The Structure of Cyameluric Acid, Hydromelonic Acid and Related Substances. *Proceedings of the National Academy of Sciences of the United States of America* 1937, *23*, 615-620.

(27) Hosmane, R. S.; Rossman, M. A.; Leonard, N. J.: Synthesis and structure of tri-s-triazine. *Journal of the American Chemical Society* 1982, *104*, 5497-5499.

(28) Cohen, M. L.: Predicting Useful Materials. *Science* 1993, *261*, 307-308.

(29) Teter, D. M.; Hemley, R. J.: Low-Compressibility Carbon Nitrides. *Science* 1996, *271*, 53-55.

(30) Nesting, D. C.; Badding, J. V.: High-Pressure Synthesis of sp2-Bonded Carbon Nitrides. *Chemistry of Materials* 1996, *8*, 1535-1539.

(31) Komatsu, T.: The First Synthesis and Characterization of Cyameluric High Polymers. *Macromolecular Chemistry and Physics* 2001, *202*, 19-25.

(32) Kroke, E.; Schwarz, M.: Novel group 14 nitrides. *Coordination Chemistry Reviews* 2004, *248*, 493-532.

(33) Goettmann, F.; Fischer, A.; Antonietti, M.; Thomas, A.: Metal-free catalysis of sustainable Friedel-Crafts reactions: direct activation of benzene by carbon nitrides to avoid the use of metal chlorides and halogenated compounds. *Chemical communications* 2006, 4530-4532.

(34) Niu, P.; Zhang, L.; Liu, G.; Cheng, H.-M.: Graphene-Like Carbon Nitride Nanosheets for Improved Photocatalytic Activities. *Advanced Functional Materials* 2012, *22*, 4763-4770.

(35) Yang, S.; Gong, Y.; Zhang, J.; Zhan, L.; Ma, L.; Fang, Z.; Vajtai, R.; Wang, X.; Ajayan, P. M.: Exfoliated Graphitic Carbon Nitride Nanosheets as Efficient Catalysts for Hydrogen Evolution Under Visible Light. *Advanced Materials* 2013, *25*, 2452-2456.

(36) Zhang, X.; Xie, X.; Wang, H.; Zhang, J.; Pan, B.; Xie, Y.: Enhanced photoresponsive ultrathin graphitic-phase C3N4 nanosheets for bioimaging. *Journal of the American Chemical Society* 2013, *135*, 18-21.

(37) Schwinghammer, K.; Mesch, M. B.; Duppel, V.; Ziegler, C.; Senker, J.; Lotsch, B. V.: Crystalline carbon nitride nanosheets for improved visible-light hydrogen evolution. *Journal of the American Chemical Society* 2014, *136*, 1730-3.

(38) Kang, Y.; Yang, Y.; Yin, L.-C.; Kang, X.; Liu, G.; Cheng, H.-M.: An Amorphous Carbon Nitride Photocatalyst with Greatly Extended Visible-Light-Responsive Range for Photocatalytic Hydrogen Generation. *Advanced Materials* 2015, *27*, 4572-4577.

(39) Liu, J.; Liu, Y.; Liu, N.; Han, Y.; Zhang, X.; Huang, H.; Lifshitz, Y.; Lee, S.-T.; Zhong, J.; Kang, Z.: Metal-free efficient photocatalyst for stable visible water splitting via a two-electron pathway. *Science* 2015, *347*, 970-974.

(40) Han, Q.; Wang, B.; Gao, J.; Cheng, Z.; Zhao, Y.; Zhang, Z.; Qu, L.: Atomically Thin Mesoporous Nanomesh of Graphitic C3N4 for High-Efficiency Photocatalytic Hydrogen Evolution. *ACS Nano* 2016, *10*, 2745-2751.

(41) Zhang, Y.; Thomas, A.; Antonietti, M.; Wang, X.: Activation of carbon nitride solids by protonation: morphology changes, enhanced ionic conductivity, and photoconduction experiments. *Journal of the American Chemical Society* 2009, *131*, 50-1.

(42) Hong, Y.; Wang, Z.; Jin, X.: Sulfuric Acid Intercalated Graphite Oxide for Graphene Preparation. *Scientific reports* 2013, *3*, 3439.

(43) Sano, T.; Tsutsui, S.; Koike, K.; Hirakawa, T.; Teramoto, Y.; Negishi, N.; Takeuchi, K.: Activation of graphitic carbon nitride (g-C3N4) by alkaline hydrothermal treatment for photocatalytic NO oxidation in gas phase. *Journal of Materials Chemistry A* 2013, *1*, 6489-6496.

(44) Xu, J.; Zhang, L.; Shi, R.; Zhu, Y.: Chemical exfoliation of graphitic carbon nitride for efficient heterogeneous photocatalysis. *Journal of Materials Chemistry A* 2013, *1*, 14766-14772.

(45) Cheng, F.; Wang, H.; Dong, X.: The amphoteric properties of g-C3N4 nanosheets and fabrication of their relevant heterostructure photocatalysts by an electrostatic re-assembly route. *Chemical communications* 2015, *51*, 7176-7179.

(46) Du, X.; Zou, G.; Wang, Z.; Wang, X.: A scalable chemical route to soluble acidified graphitic carbon nitride: an ideal precursor for isolated ultrathin g-C3N4 nanosheets. *Nanoscale* 2015, *7*, 8701-8706.

(47) Ye, C.; Li, J.-X.; Li, Z.-J.; Li, X.-B.; Fan, X.-B.; Zhang, L.-P.; Chen, B.; Tung, C.-H.; Wu, L.-Z.: Enhanced Driving Force and Charge Separation Efficiency of Protonated g-C3N4 for Photocatalytic O2 Evolution. *ACS Catalysis* 2015, *5*, 6973-6979.

(48) Chen, X.; Zhang, J.; Fu, X.; Antonietti, M.; Wang, X.: Fe-g-C3N4-Catalyzed Oxidation of Benzene to Phenol Using Hydrogen Peroxide and Visible Light. *Journal of the American Chemical Society* 2009, *131*, 11658-11659.

(49) Wang, X.; Chen, X.; Thomas, A.; Fu, X.; Antonietti, M.: Metal-Containing Carbon Nitride Compounds: A New Functional Organic–Metal Hybrid Material. *Advanced Materials* 2009, *21*, 1609-1612.

(50) Zhang, J.; Sun, J.; Maeda, K.; Domen, K.; Liu, P.; Antonietti, M.; Fu, X.; Wang, X.: Sulfur-mediated synthesis of carbon nitride: Band-gap engineering and improved functions for photocatalysis. *Energy & Environmental Science* 2011, *4*, 675-678.

(51) Li, J.; Shen, B.; Hong, Z.; Lin, B.; Gao, B.; Chen, Y.: A facile approach to synthesize novel oxygen-doped g-C3N4 with superior visible-light photoreactivity. *Chemical communications* 2012, *48*, 12017-12019.

(52) Huang, Z.-F.; Song, J.; Pan, L.; Wang, Z.; Zhang, X.; Zou, J.-J.; Mi, W.; Zhang, X.; Wang, L.: Carbon nitride with simultaneous porous network and O-doping for efficient solar-energy-driven hydrogen evolution. *Nano Energy* 2015, *12*, 646-656.

(53) Guo, S.; Deng, Z.; Li, M.; Jiang, B.; Tian, C.; Pan, Q.; Fu, H.: Phosphorus-Doped Carbon Nitride Tubes with a Layered Micro-nanostructure for Enhanced Visible-Light Photocatalytic Hydrogen Evolution. *Angewandte Chemie International Edition* 2016, *55*, 1830-1834.

(54) Xiong, T.; Cen, W.; Zhang, Y.; Dong, F.: Bridging the g-C3N4 Interlayers for Enhanced Photocatalysis. *ACS Catalysis* 2016, *6*, 2462-2472.

(55) Zhang, J.; Chen , X.; Takanabe, K.; Maeda, K.; Domen, K.; Epping, J. D.; Fu, X.; Antonietti, M.; Wang , X.: Synthesis of a Carbon Nitride Structure for Visible-Light Catalysis by Copolymerization. *Angewandte Chemie International Edition* 2010, *49*, 441-444.

(56) Zhang, J.; Zhang, G.; Chen, X.; Lin, S.; Möhlmann, L.; Lipner, G.; Antonietti, M.; Blechert, S.; Wang, X.: Co-Monomer Control of Carbon Nitride Semiconductors to Optimize Hydrogen Evolution with Visible Light. *Angewandte Chemie International Edition* 2012, *51*, 3183-3187.

(57) Shiraishi, Y.; Kanazawa, S.; Kofuji, Y.; Sakamoto, H.; Ichikawa, S.; Tanaka, S.; Hirai, T.: Sunlight-Driven Hydrogen Peroxide Production from Water and Molecular Oxygen by Metal-Free Photocatalysts. *Angewandte Chemie International Edition* 2014, *53*, 13454-13459.

(58) Kofuji, Y.; Isobe, Y.; Shiraishi, Y.; Sakamoto, H.; Tanaka, S.; Ichikawa, S.; Hirai, T.: Carbon Nitride–Aromatic Diimide–Graphene Nanohybrids: Metal-Free Photocatalysts for Solar-to-Hydrogen Peroxide Energy Conversion with 0.2% Efficiency. *Journal of the American Chemical Society* 2016, *138*, 10019-10025.

(59) Kofuji, Y.; Ohkita, S.; Shiraishi, Y.; Sakamoto, H.; Tanaka, S.; Ichikawa, S.; Hirai, T.: Graphitic Carbon Nitride Doped with Biphenyl Diimide: Efficient Photocatalyst for Hydrogen Peroxide Production from Water and Molecular Oxygen by Sunlight. *ACS Catalysis* 2016, 7021-7029.

(60) Chen, X.; Liu, Q.; Wu, Q.; Du, P.; Zhu, J.; Dai, S.; Yang, S.: Incorporating Graphitic Carbon Nitride (g-C3N4) Quantum Dots into Bulk-Heterojunction Polymer Solar Cells Leads to Efficiency Enhancement. *Advanced Functional Materials* 2016, *26*, 1719-1728.

(61) Zheng, Y.; Liu, J.; Liang, J.; Jaroniec, M.; Qiao, S. Z.: Graphitic carbon nitride materials: controllable synthesis and applications in fuel cells and photocatalysis. *Energy & Environmental Science* 2012, *5*, 6717-6731.

(62) Cao, S.; Low, J.; Yu, J.; Jaroniec, M.: Polymeric Photocatalysts Based on Graphitic Carbon Nitride. *Advanced Materials* 2015, *27*, 2150-2176.

(63) Zhang, X.; Meng, Z.; Rao, D.; Wang, Y.; Shi, Q.; Liu, Y.; Wu, H.; Deng, K.; Liu, H.; Lu, R.: Efficient band structure tuning, charge separation, and visible-light response in ZrS2-based van der Waals heterostructures. *Energy & Environmental Science* 2016, *9*, 841-849.

(64) Novoselov, K. S.; Geim, A. K.; Morozov, S. V.; Jiang, D.; Zhang, Y.; Dubonos, S. V.; Grigorieva, I. V.; Firsov, A. A.: Electric Field Effect in Atomically Thin Carbon Films. *Science* 2004, *306*, 666-669.

(65) Coleman, J. N.; Lotya, M.; O'Neill, A.; Bergin, S. D.; King, P. J.; Khan, U.; Young, K.; Gaucher, A.; De, S.; Smith, R. J.; Shvets, I. V.; Arora, S. K.; Stanton, G.; Kim, H.-Y.; Lee, K.; Kim, G. T.; Duesberg, G. S.; Hallam, T.; Boland, J. J.; Wang, J. J.; Donegan, J. F.; Grunlan, J. C.; Moriarty, G.; Shmeliov, A.; Nicholls, R. J.; Perkins, J. M.; Grieveson, E. M.; Theuwissen, K.; McComb, D. W.; Nellist, P. D.; Nicolosi, V.: Two-Dimensional Nanosheets Produced by Liquid Exfoliation of Layered Materials. *Science* 2011, *331*, 568-571.

(66) Bergin, S. D.; Nicolosi, V.; Streich, P. V.; Giordani, S.; Sun, Z.; Windle, A. H.; Ryan, P.; Niraj, N. P. P.; Wang, Z.-T. T.; Carpenter, L.; Blau, W. J.; Boland, J. J.; Hamilton, J. P.; Coleman, J. N.: Towards Solutions of Single-Walled Carbon Nanotubes in Common Solvents. *Advanced Materials* 2008, *20*, 1876-1881.

(67) Hernandez, Y.; Nicolosi, V.; Lotya, M.; Blighe, F. M.; Sun, Z.; De, S.; McGovern, I. T.; Holland, B.; Byrne, M.; Gun'Ko, Y. K.; Boland, J. J.; Niraj, P.; Duesberg, G.; Krishnamurthy, S.; Goodhue, R.; Hutchison, J.; Scardaci, V.; Ferrari, A. C.; Coleman, J. N.: High-yield production of graphene by liquid-phase exfoliation of graphite. *Nat Nano* 2008, *3*, 563-568.

(68) Li, Y.; Ouyang, S.; Xu, H.; Wang, X.; Bi, Y.; Zhang, Y.; Ye, J.: Constructing Solid–Gas-Interfacial Fenton Reaction over Alkalinized-C3N4 Photocatalyst To Achieve Apparent Quantum Yield of 49% at 420 nm. *Journal of the American Chemical Society* 2016, *138*, 13289-13297.

(69) Tong, J.; Zhang, L.; Li, F.; Li, M.; Cao, S.: An efficient top-down approach for the fabrication of large-aspect-ratio g-C3N4 nanosheets with enhanced photocatalytic activities. *Physical Chemistry Chemical Physics* 2015, *17*, 23532-23537.

(70) Tong, J.; Zhang, L.; Li, F.; Wang, K.; Han, L.; Cao, S.: Rapid and high-yield production of g-C3N4 nanosheets via chemical exfoliation for photocatalytic H2 evolution. *RSC Advances* 2015, *5*, 88149-88153.

(71) Hummers, W. S.; Offeman, R. E.: Preparation of Graphitic Oxide. *Journal of the American Chemical Society* 1958, *80*, 1339-1339.

(72) Marcano, D. C.; Kosynkin, D. V.; Berlin, J. M.; Sinitskii, A.; Sun, Z.; Slesarev, A.; Alemany, L. B.; Lu, W.; Tour, J. M.: Improved Synthesis of Graphene Oxide. *ACS Nano* 2010, *4*, 4806-4814.

(73) Figueiredo, J. L.: Functionalization of porous carbons for catalytic applications. *Journal of Materials Chemistry A* 2013, *1*, 9351-9364.

(74) Su, D. S.; Perathoner, S.; Centi, G.: Nanocarbons for the development of advanced catalysts. *Chemical reviews* 2013, *113*, 5782-5816.

(75) Chu, S.; Wang, Y.; Guo, Y.; Feng, J.; Wang, C.; Luo, W.; Fan, X.; Zou, Z.: Band Structure Engineering of Carbon Nitride: In Search of a Polymer Photocatalyst with High Photooxidation Property. *ACS Catalysis* 2013, *3*, 912-919.

(76) Fan, X.; Zhang, L.; Cheng, R.; Wang, M.; Li, M.; Zhou, Y.; Shi, J.: Construction of Graphitic C3N4-Based Intramolecular Donor–Acceptor Conjugated Copolymers for Photocatalytic Hydrogen Evolution. *ACS Catalysis* 2015, *5*, 5008-5015.

(77) Guo, S.; Zhu, Y.; Yan, Y.; Min, Y.; Fan, J.; Xu, Q.: Holey structured graphitic carbon nitride thin sheets with edge oxygen doping via photo-Fenton reaction with enhanced photocatalytic activity. *Applied Catalysis B: Environmental* 2016, *185*, 315-321.

(78) Guo, Y.; Chu, S.; Yan, S.; Wang, Y.; Zou, Z.: Developing a polymeric semiconductor photocatalyst with visible light response. *Chemical communications* 2010, *46*, 7325-7327.

(79) Li, Z.; Kong, C.; Lu, G.: Visible Photocatalytic Water Splitting and Photocatalytic Two-Electron Oxygen Formation over Cu- and Fe-Doped g-C3N4. *The Journal of Physical Chemistry C* 2016, *120*, 56-63.

(80) Qiu, Y.; Xin, L.; Jia, F.; Xie, J.; Li, W.: Three-Dimensional Phosphorus-Doped Graphitic-C3N4 Self-Assembly with NH2-Functionalized Carbon Composite Materials for Enhanced Oxygen Reduction Reaction. *Langmuir* 2016, *32*, 12569-12578.

(81) Zheng, Y.; Jiao, Y.; Zhu, Y.; Li, L. H.; Han, Y.; Chen, Y.; Du, A.; Jaroniec, M.; Qiao, S. Z.: Hydrogen evolution by a metal-free electrocatalyst. *Nature communications* 2014, *5*.

(82) Dong, G.; Zhao, K.; Zhang, L.: Carbon self-doping induced high electronic conductivity and photoreactivity of g-C3N4. *Chemical communications* 2012, *48*, 6178-6180.

(83) Zhang, P.; Li, X.; Shao, C.; Liu, Y.: Hydrothermal synthesis of carbon-rich graphitic carbon nitride nanosheets for photoredox catalysis. *Journal of Materials Chemistry A* 2015, *3*, 3281-3284.

(84) Zhou, Y.; Zhang, L.; Huang, W.; Kong, Q.; Fan, X.; Wang, M.; Shi, J.: N-doped graphitic carbon-incorporated g-C3N4 for remarkably enhanced photocatalytic H2 evolution under visible light. *Carbon* 2016, *99*, 111-117.

(85) Dong, G.; Ai, Z.; Zhang, L.: Efficient anoxic pollutant removal with oxygen functionalized graphitic carbon nitride under visible light. *RSC Advances* 2014, *4*, 5553-5560.

(86) Cui, J.; Liang, S.; Wang, X.; Zhang, J.: First principle modeling of oxygen-doped monolayer graphitic carbon nitride. *Materials Chemistry and Physics* 2015, *161*, 194-200.

(87) Liu, J.; Li, W.; Duan, L.; Li, X.; Ji, L.; Geng, Z.; Huang, K.; Lu, L.; Zhou, L.; Liu, Z.; Chen, W.; Liu, L.; Feng, S.; Zhang, Y.: A Graphene-like Oxygenated Carbon Nitride Material for Improved Cycle-Life Lithium/Sulfur Batteries. *Nano letters* 2015, *15*, 5137-5142.

(88) Liu, S.; Sun, H.; Ang, H. M.; Tade, M. O.; Wang, S.: Integrated oxygen-doping and dye sensitization of graphitic carbon nitride for enhanced visible light photodegradation. *Journal of colloid and interface science* 2016, *476*, 193-199.

(89) Chen, G.; Gao, S.-P.: Structure and electronic structure of S-doped graphitic C 3 N 4 investigated by density functional theory. *Chinese Physics B* 2012, *21*, 107101.

(90) Ma, X.; Lv, Y.; Xu, J.; Liu, Y.; Zhang, R.; Zhu, Y.: A Strategy of Enhancing the Photoactivity of g-C3N4 via Doping of Nonmetal Elements: A First-Principles Study. *The Journal of Physical Chemistry C* 2012, *116*, 23485-23493.

(91) Zhang, J.; Zhang, M.; Zhang, G.; Wang, X.: Synthesis of Carbon Nitride Semiconductors in Sulfur Flux for Water Photoredox Catalysis. *ACS Catalysis* 2012, *2*, 940-948.

(92) Cao, L.; Wang, R.; Wang, D.: Synthesis and characterization of sulfur self-doped g-C3N4 with efficient visible-light photocatalytic activity. *Materials Letters* 2015, *149*, 50-53.

(93) Lin, S.; Ye, X.; Gao, X.; Huang, J.: Mechanistic insight into the water photooxidation on pure and sulfur-doped g-C3N4 photocatalysts from DFT calculations with dispersion corrections. *Journal of Molecular Catalysis A: Chemical* 2015, *406*, 137-144.

(94) Xu, C.; Han, Q.; Zhao, Y.; Wang, L.; Li, Y.; Qu, L.: Sulfur-doped graphitic carbon nitride decorated with graphene quantum dots for an efficient metal-free electrocatalyst. *Journal of Materials Chemistry A* 2015, *3*, 1841-1846.

(95) Liu, G.; Niu, P.; Sun, C.; Smith, S. C.; Chen, Z.; Lu, G. Q.; Cheng, H.-M.: Unique Electronic Structure Induced High Photoreactivity of Sulfur-Doped Graphitic C3N4. *Journal of the American Chemical Society* 2010, *132*, 11642-11648.

(96) Zhang, L.; Chen, X.; Guan, J.; Jiang, Y.; Hou, T.; Mu, X.: Facile synthesis of phosphorus doped graphitic carbon nitride polymers with enhanced visible-light photocatalytic activity. *Materials Research Bulletin* 2013, *48*, 3485-3491.

(97) Hu, S.; Ma, L.; You, J.; Li, F.; Fan, Z.; Wang, F.; Liu, D.; Gui, J.: A simple and efficient method to prepare a phosphorus modified g-C3N4 visible light photocatalyst. *RSC Advances* 2014, *4*, 21657-21663.

(98) Ma, T. Y.; Ran, J.; Dai, S.; Jaroniec, M.; Qiao, S. Z.: Phosphorus-Doped Graphitic Carbon Nitrides Grown In Situ on Carbon-Fiber Paper: Flexible and Reversible Oxygen Electrodes. *Angewandte Chemie International Edition* 2015, *54*, 4646-4650.

(99) Ran, J.; Ma, T. Y.; Gao, G.; Du, X.-W.; Qiao, S. Z.: Porous P-doped graphitic carbon nitride nanosheets for synergistically enhanced visible-light photocatalytic H2 production. *Energy & Environmental Science* 2015, *8*, 3708-3717.

(100) Zhou, Y.; Zhang, L.; Liu, J.; Fan, X.; Wang, B.; Wang, M.; Ren, W.; Wang, J.; Li, M.; Shi, J.: Brand new P-doped g-C3N4: enhanced photocatalytic activity for H2 evolution and Rhodamine B degradation under visible light. *Journal of Materials Chemistry A* 2015, *3*, 3862-3867.

(101) Chen, W.; Liu, T.-Y.; Huang, T.; Liu, X.-H.; Yang, X.-J.: Novel mesoporous P-doped graphitic carbon nitride nanosheets coupled with ZnIn2S4 nanosheets as efficient visible light driven heterostructures with remarkably enhanced photo-reduction activity. *Nanoscale* 2016, *8*, 3711-3719.

(102) Lan, D.-H.; Wang, H.-T.; Chen, L.; Au, C.-T.; Yin, S.-F.: Phosphorous-modified bulk graphitic carbon nitride: Facile preparation and application as an acid-base bifunctional and efficient catalyst for CO2 cycloaddition with epoxides. *Carbon* 2016, *100*, 81-89.

(103) Chen, W.; Huang, T.; Liu, T.-Y.; Duan, G.-R.; Yang, X.-J.; Liu, X.-H.: Ultrasound-assisted growth of Zn0.2Cd0.8S nanoparticles on mesoporous P-doped graphitic carbon nitride nanosheets for superior photocatalytic activities. *Journal of Alloys and Compounds* 2017, *690*, 503-511.

(104) Zhang, Y.; Mori, T.; Ye, J.; Antonietti, M.: Phosphorus-Doped Carbon Nitride Solid: Enhanced Electrical Conductivity and Photocurrent Generation. *Journal of the American Chemical Society* 2010, *132*, 6294-6295.

(105) Li, H.; Liu, Y.; Gao, X.; Fu, C.; Wang, X.: Facile Synthesis and Enhanced Visible-Light Photocatalysis of Graphitic Carbon Nitride Composite Semiconductors. *ChemSusChem* 2015, *8*, 1189-1196.

(106) Pan, H.; Zhang, H.; Liu, H.; Chen, L.: Interstitial boron doping effects on the electronic and magnetic properties of graphitic carbon nitride materials. *Solid State Communications* 2015, *203*, 35-40.

(107) Gao, D.; Liu, Y.; Liu, P.; Si, M.; Xue, D.: Atomically Thin B doped g-C3N4 Nanosheets: High-Temperature Ferromagnetism and calculated Half-Metallicity. *Scientific reports* 2016, *6*, 35768.

(108) Gu, Q.; Liu, J.; Gao, Z.; Xue, C.: Homogenous Boron-doping in Self-sensitized Carbon Nitride for Enhanced Visible-light Photocatalytic Activity. *Chemistry – An Asian Journal* 2016, *11*, 3169-3173.

(109) Raziq, F.; Qu, Y.; Zhang, X.; Humayun, M.; Wu, J.; Zada, A.; Yu, H.; Sun, X.; Jing, L.: Enhanced Cocatalyst-Free Visible-Light Activities for Photocatalytic Fuel Production of g-C3N4 by Trapping Holes and Transferring Electrons. *The Journal of Physical Chemistry C* 2016, *120*, 98-107.

(110) Sagara, N.; Kamimura, S.; Tsubota, T.; Ohno, T.: Photoelectrochemical CO2 reduction by a p-type boron-doped g-C3N4 electrode under visible light. *Applied Catalysis B: Environmental* 2016, *192*, 193-198.

(111) Wang, Y.; Di, Y.; Antonietti, M.; Li, H.; Chen, X.; Wang, X.: Excellent Visible-Light Photocatalysis of Fluorinated Polymeric Carbon Nitride Solids. *Chemistry of Materials* 2010, *22*, 5119-5121.

(112) Ding, K.; Wen, L.; Huang, M.; Zhang, Y.; Lu, Y.; Chen, Z.: How does the B,F-monodoping and B/F-codoping affect the photocatalytic water-splitting performance of g-C3N4? *Physical Chemistry Chemical Physics* 2016, *18*, 19217-19226.

(113) Zhang, G.; Zhang, M.; Ye, X.; Qiu, X.; Lin, S.; Wang, X.: Iodine Modified Carbon Nitride Semiconductors as Visible Light Photocatalysts for Hydrogen Evolution. *Advanced Materials* 2014, *26*, 805-809.

(114) Han, Q.; Hu, C.; Zhao, F.; Zhang, Z.; Chen, N.; Qu, L.: One-step preparation of iodine-doped graphitic carbon nitride nanosheets as efficient photocatalysts for visible light water splitting. *Journal of Materials Chemistry A* 2015, *3*, 4612-4619.

(115) Guo, Y.; Chen, T.; Liu, Q.; Zhang, Z.; Fang, X.: Insight into the Enhanced Photocatalytic Activity of Potassium and Iodine Codoped Graphitic Carbon Nitride Photocatalysts. *The Journal of Physical Chemistry C* 2016, *120*, 25328-25337.

(116) Tonda, S.; Kumar, S.; Kandula, S.; Shanker, V.: Fe-doped and -mediated graphitic carbon nitride nanosheets for enhanced photocatalytic performance under natural sunlight. *Journal of Materials Chemistry A* 2014, *2*, 6772-6780.

(117) Gao, L.-F.; Wen, T.; Xu, J.-Y.; Zhai, X.-P.; Zhao, M.; Hu, G.-W.; Chen, P.; Wang, Q.; Zhang, H.-L.: Iron-Doped Carbon Nitride-Type Polymers as Homogeneous Organocatalysts for Visible Light-Driven Hydrogen Evolution. *ACS applied materials & interfaces* 2016, *8*, 617-624.

(118) Zou, X.; Silva, R.; Goswami, A.; Asefa, T.: Cu-doped carbon nitride: Bio-inspired synthesis of H2-evolving electrocatalysts using graphitic carbon nitride (g-C3N4) as a host material. *Applied Surface Science* 2015, *357, Part A*, 221-228.

(119) Le, S.; Jiang, T.; Zhao, Q.; Liu, X.; Li, Y.; Fang, B.; Gong, M.: Cu-doped mesoporous graphitic carbon nitride for enhanced visible-light driven photocatalysis. *RSC Advances* 2016, *6*, 38811-38819.

(120) Bing, Y.; Qiuye, L.; Hideo, I.; Tetsuya, K.; Jinhua, Y.: Hydrogen production using zinc-doped carbon nitride catalyst irradiated with visible light. *Science and Technology of Advanced Materials* 2011, *12*, 034401.

(121) Ding, Z.; Chen, X.; Antonietti, M.; Wang, X.: Synthesis of Transition Metal-Modified Carbon Nitride Polymers for Selective Hydrocarbon Oxidation. *ChemSusChem* 2011, *4*, 274-281.

(122) Kong, L.; Dong, Y.; Jiang, P.; Wang, G.; Zhang, H.; Zhao, N.: Light-assisted rapid preparation of a Ni/g-C3N4 magnetic composite for robust photocatalytic H2 evolution from water. *Journal of Materials Chemistry A* 2016, *4*, 9998-10007.

(123) Mu, J.; Li, J.; Zhao, X.; Yang, E.-C.; Zhao, X.-J.: Cobalt-doped graphitic carbon nitride with enhanced peroxidase-like activity for wastewater treatment. *RSC Advances* 2016, *6*, 35568-35576.

(124) Chen, P.-W.; Li, K.; Yu, Y.-X.; Zhang, W.-D.: Cobalt-doped graphitic carbon nitride photocatalysts with high activity for hydrogen evolution. *Applied Surface Science* 2017, *392*, 608-615.

(125) Ghosh, D.; Periyasamy, G.; Pati, S. K.: Transition Metal Embedded Two-Dimensional C3N4–Graphene Nanocomposite: A Multifunctional Material. *The Journal of Physical Chemistry C* 2014, *118*, 15487-15494.

(126) Choudhuri, I.; Kumar, S.; Mahata, A.; Rawat, K. S.; Pathak, B.: Transition-metal embedded carbon nitride monolayers: high-temperature ferromagnetism and half-metallicity. *Nanoscale* 2016, *8*, 14117-14126.

(127) Chen, Y.; Zhang, J.; Zhang, M.; Wang, X.: Molecular and textural engineering of conjugated carbon nitride catalysts for selective oxidation of alcohols with visible light. *Chemical Science* 2013, *4*, 3244-3248.

(128) Zhang, G.; Wang, X.: A facile synthesis of covalent carbon nitride photocatalysts by Co-polymerization of urea and phenylurea for hydrogen evolution. *Journal of Catalysis* 2013, *307*, 246-253.

(129) Zhang, M.; Wang, X.: Two dimensional conjugated polymers with enhanced optical absorption and charge separation for photocatalytic hydrogen evolution. *Energy & Environmental Science* 2014, *7*, 1902-1906.

(130) Chen, Z.; Sun, P.; Fan, B.; Liu, Q.; Zhang, Z.; Fang, X.: Textural and electronic structure engineering of carbon nitride via doping with π-deficient aromatic pyridine ring for improving photocatalytic activity. *Applied Catalysis B: Environmental* 2015, *170–171*, 10-16.

(131) Ho, W.; Zhang, Z.; Lin, W.; Huang, S.; Zhang, X.; Wang, X.; Huang, Y.: Copolymerization with 2,4,6-Triaminopyrimidine for the Rolling-up the Layer Structure, Tunable Electronic Properties, and Photocatalysis of g-C3N4. *ACS applied materials & interfaces* 2015, *7*, 5497-5505.

(132) Qin, J.; Wang, S.; Ren, H.; Hou, Y.; Wang, X.: Photocatalytic reduction of CO2 by graphitic carbon nitride polymers derived from urea and barbituric acid. *Applied Catalysis B: Environmental* 2015, *179*, 1-8.

(133) Zhang, J.; Chen, Y.; Wang, X.: Two-dimensional covalent carbon nitride nanosheets: synthesis, functionalization, and applications. *Energy & Environmental Science* 2015, *8*, 3092-3108.

(134) Fan, X.; Zhang, L.; Wang, M.; Huang, W.; Zhou, Y.; Li, M.; Cheng, R.; Shi, J.: Constructing carbon-nitride-based copolymers via Schiff base chemistry for visible-light photocatalytic hydrogen evolution. *Applied Catalysis B: Environmental* 2016, *182*, 68-73.

(135) Zhang, J.; Zhang, M.; Sun, R.-Q.; Wang, X.: A Facile Band Alignment of Polymeric Carbon Nitride Semiconductors to Construct Isotype Heterojunctions. *Angewandte Chemie International Edition* 2012, *51*, 10145-10149.

(136) Wang, H.; Zhang, L.; Chen, Z.; Hu, J.; Li, S.; Wang, Z.; Liu, J.; Wang, X.: Semiconductor heterojunction photocatalysts: design, construction, and photocatalytic performances. *Chemical Society Reviews* 2014, *43*, 5234-5244.

(137) Bai, S.; Wang, X.; Hu, C.; Xie, M.; Jiang, J.; Xiong, Y.: Two-dimensional g-C3N4: an ideal platform for examining facet selectivity of metal co-catalysts in photocatalysis. *Chemical communications* 2014, *50*, 6094-6097.

(138) Zhang, W.; Huang, H.; Li, F.; Deng, K.; Wang, X.: Palladium nanoparticles supported on graphitic carbon nitride-modified reduced graphene oxide as highly efficient catalysts for formic acid and methanol electrooxidation. *Journal of Materials Chemistry A* 2014, *2*, 19084-19094.

(139) Sun, J.; Fu, Y.; He, G.; Sun, X.; Wang, X.: Green Suzuki–Miyaura coupling reaction catalyzed by palladium nanoparticles supported on graphitic carbon nitride. *Applied Catalysis B: Environmental* 2015, *165*, 661-667.

(140) Li, X.; Bi, W.; Zhang, L.; Tao, S.; Chu, W.; Zhang, Q.; Luo, Y.; Wu, C.; Xie, Y.: Single-Atom Pt as Co-Catalyst for Enhanced Photocatalytic H2 Evolution. *Advanced Materials* 2016, *28*, 2427-2431.

(141) Shiraishi, Y.; Kofuji, Y.; Kanazawa, S.; Sakamoto, H.; Ichikawa, S.; Tanaka, S.; Hirai, T.: Platinum nanoparticles strongly associated with graphitic carbon nitride as efficient co-catalysts for photocatalytic hydrogen evolution under visible light. *Chemical communications* 2014, *50*, 15255-15258.

(142) Zhang, G.; Lan, Z.-A.; Lin, L.; Lin, S.; Wang, X.: Overall water splitting by Pt/g-C3N4 photocatalysts without using sacrificial agents. *Chemical Science* 2016, *7*, 3062-3066.

(143) Shiraishi, Y.; Sakamoto, H.; Sugano, Y.; Ichikawa, S.; Hirai, T.: Pt–Cu Bimetallic Alloy Nanoparticles Supported on Anatase TiO2: Highly Active Catalysts for Aerobic Oxidation Driven by Visible Light. *ACS Nano* 2013, *7*, 9287-9297.

(144) Zhang, Y.; Ligthart, D. A. J. M.; Quek, X.-Y.; Gao, L.; Hensen, E. J. M.: Influence of Rh nanoparticle size and composition on the photocatalytic water splitting performance of Rh/graphitic carbon nitride. *International Journal of Hydrogen Energy* 2014, *39*, 11537-11546.

(145) Samanta, S.; Martha, S.; Parida, K.: Facile Synthesis of Au/g-C3N4 Nanocomposites: An Inorganic/Organic Hybrid Plasmonic Photocatalyst with Enhanced Hydrogen Gas Evolution Under Visible-Light Irradiation. *ChemCatChem* 2014, *6*, 1453-1462.

(146) Xue, J.; Ma, S.; Zhou, Y.; Zhang, Z.; He, M.: Facile Photochemical Synthesis of Au/Pt/g-C3N4 with Plasmon-Enhanced Photocatalytic Activity for Antibiotic Degradation. *ACS applied materials & interfaces* 2015, *7*, 9630-9637.

(147) Yao, X.; Liu, X.; Hu, X.: Synthesis of the Ag/AgCl/g-C3N4 Composite with High Photocatalytic Activity under Visible Light Irradiation. *ChemCatChem* 2014, *6*, 3409-3418.

(148) Wang, L.; Yu, M.; Wu, C.; Deng, N.; Wang, C.; Yao, X.: Synthesis of Ag/g-C3N4 Composite as Highly Efficient Visible-Light Photocatalyst for Oxidative Amidation of Aromatic Aldehydes. *Advanced Synthesis & Catalysis* 2016, *358*, 2631-2641.

(149) Dong, F.; Zhao, Z.; Sun, Y.; Zhang, Y.; Yan, S.; Wu, Z.: An Advanced Semimetal–Organic Bi Spheres–g-C3N4 Nanohybrid with SPR-Enhanced Visible-Light Photocatalytic Performance for NO Purification. *Environmental Science & Technology* 2015, *49*, 12432-12440.
(150) Kuriki, R.; Sekizawa, K.; Ishitani, O.; Maeda, K.: Visible-Light-Driven CO2 Reduction with Carbon Nitride: Enhancing the Activity of Ruthenium Catalysts. *Angewandte Chemie International Edition* 2015, *54*, 2406-2409.
(151) Lin, J.; Pan, Z.; Wang, X.: Photochemical Reduction of CO2 by Graphitic Carbon Nitride Polymers. *ACS Sustainable Chemistry & Engineering* 2014, *2*, 353-358.
(152) Ge, L.; Han, C.; Xiao, X.; Guo, L.: In situ synthesis of cobalt–phosphate (Co–Pi) modified g-C3N4 photocatalysts with enhanced photocatalytic activities. *Applied Catalysis B: Environmental* 2013, *142–143*, 414-422.
(153) Yan, H.; Yang, H.: TiO2–g-C3N4 composite materials for photocatalytic H2 evolution under visible light irradiation. *Journal of Alloys and Compounds* 2011, *509*, L26-L29.
(154) Kondo, K.; Murakami, N.; Ye, C.; Tsubota, T.; Ohno, T.: Development of highly efficient sulfur-doped TiO2 photocatalysts hybridized with graphitic carbon nitride. *Applied Catalysis B: Environmental* 2013, *142–143*, 362-367.
(155) Yu, J.; Wang, S.; Low, J.; Xiao, W.: Enhanced photocatalytic performance of direct Z-scheme g-C3N4-TiO2 photocatalysts for the decomposition of formaldehyde in air. *Physical Chemistry Chemical Physics* 2013, *15*, 16883-16890.
(156) Sun, J.-X.; Yuan, Y.-P.; Qiu, L.-G.; Jiang, X.; Xie, A.-J.; Shen, Y.-H.; Zhu, J.-F.: Fabrication of composite photocatalyst g-C3N4-ZnO and enhancement of photocatalytic activity under visible light. *Dalton Transactions* 2012, *41*, 6756-6763.
(157) Kumar, S.; Baruah, A.; Tonda, S.; Kumar, B.; Shanker, V.; Sreedhar, B.: Cost-effective and eco-friendly synthesis of novel and stable N-doped ZnO/g-C3N4 core-shell nanoplates with excellent visible-light responsive photocatalysis. *Nanoscale* 2014, *6*, 4830-4842.
(158) He, Y.; Wang, Y.; Zhang, L.; Teng, B.; Fan, M.: High-efficiency conversion of CO2 to fuel over ZnO/g-C3N4 photocatalyst. *Applied Catalysis B: Environmental* 2015, *168–169*, 1-8.
(159) Huang, L.; Xu, H.; Li, Y.; Li, H.; Cheng, X.; Xia, J.; Xu, Y.; Cai, G.: Visible-light-induced WO3/g-C3N4 composites with enhanced photocatalytic activity. *Dalton Transactions* 2013, *42*, 8606-8616.
(160) Jin, Z.; Murakami, N.; Tsubota, T.; Ohno, T.: Complete oxidation of acetaldehyde over a composite photocatalyst of graphitic carbon nitride and tungsten(VI) oxide under visible-light irradiation. *Applied Catalysis B: Environmental* 2014, *150–151*, 479-485.
(161) Martin, D. J.; Reardon, P. J. T.; Moniz, S. J. A.; Tang, J.: Visible Light-Driven Pure Water Splitting by a Nature-Inspired Organic Semiconductor-Based System. *Journal of the American Chemical Society* 2014, *136*, 12568-12571.
(162) Ohno, T.; Murakami, N.; Koyanagi, T.; Yang, Y.: Photocatalytic reduction of CO2 over a hybrid photocatalyst composed of WO3 and graphitic carbon nitride (g-C3N4) under visible light. *Journal of CO2 Utilization* 2014, *6*, 17-25.
(163) Ge, L.; Zuo, F.; Liu, J.; Ma, Q.; Wang, C.; Sun, D.; Bartels, L.; Feng, P.: Synthesis and Efficient Visible Light Photocatalytic Hydrogen Evolution of Polymeric g-C3N4 Coupled with CdS Quantum Dots. *The Journal of Physical Chemistry C* 2012, *116*, 13708-13714.

(164) Zhang, J.; Wang, Y.; Jin, J.; Zhang, J.; Lin, Z.; Huang, F.; Yu, J.: Efficient Visible-Light Photocatalytic Hydrogen Evolution and Enhanced Photostability of Core/Shell CdS/g-C3N4 Nanowires. *ACS applied materials & interfaces* 2013, *5*, 10317-10324.

(165) Ge, L.; Han, C.; Xiao, X.; Guo, L.: Synthesis and characterization of composite visible light active photocatalysts MoS2–g-C3N4 with enhanced hydrogen evolution activity. *International Journal of Hydrogen Energy* 2013, *38*, 6960-6969.

(166) Hou, Y.; Wen, Z.; Cui, S.; Guo, X.; Chen, J.: Constructing 2D Porous Graphitic C3N4 Nanosheets/Nitrogen-Doped Graphene/Layered MoS2 Ternary Nanojunction with Enhanced Photoelectrochemical Activity. *Advanced Materials* 2013, *25*, 6291-6297.

(167) Hou, Y.; Li, J.; Wen, Z.; Cui, S.; Yuan, C.; Chen, J.: N-doped graphene/porous g-C3N4 nanosheets supported layered-MoS2 hybrid as robust anode materials for lithium-ion batteries. *Nano Energy* 2014, *8*, 157-164.

(168) Shi, Y.; Jiang, S.; Zhou, K.; Wang, B.; Wang, B.; Gui, Z.; Hu, Y.; Yuen, R. K. K.: Facile preparation of ZnS/g-C3N4 nanohybrids for enhanced optical properties. *RSC Advances* 2014, *4*, 2609-2613.

(169) Yang, X.; Qian, F.; Zou, G.; Li, M.; Lu, J.; Li, Y.; Bao, M.: Facile fabrication of acidified g-C3N4/g-C3N4 hybrids with enhanced photocatalysis performance under visible light irradiation. *Applied Catalysis B: Environmental* 2016, *193*, 22-35.

(170) Chai, B.; Liao, X.; Song, F.; Zhou, H.: Fullerene modified C3N4 composites with enhanced photocatalytic activity under visible light irradiation. *Dalton Transactions* 2014, *43*, 982-989.

(171) Ge, L.; Han, C.: Synthesis of MWNTs/g-C3N4 composite photocatalysts with efficient visible light photocatalytic hydrogen evolution activity. *Applied Catalysis B: Environmental* 2012, *117–118*, 268-274.

(172) Zhong, Y.; Yuan, J.; Wen, J.; Li, X.; Xu, Y.; Liu, W.; Zhang, S.; Fang, Y.: Earth-abundant NiS co-catalyst modified metal-free mpg-C3N4/CNT nanocomposites for highly efficient visible-light photocatalytic H2 evolution. *Dalton Transactions* 2015, *44*, 18260-18269.

(173) Xiang, Q.; Yu, J.; Jaroniec, M.: Preparation and Enhanced Visible-Light Photocatalytic H2-Production Activity of Graphene/C3N4 Composites. *The Journal of Physical Chemistry C* 2011, *115*, 7355-7363.

(174) Du, A.; Sanvito, S.; Li, Z.; Wang, D.; Jiao, Y.; Liao, T.; Sun, Q.; Ng, Y. H.; Zhu, Z.; Amal, R.; Smith, S. C.: Hybrid graphene and graphitic carbon nitride nanocomposite: gap opening, electron-hole puddle, interfacial charge transfer, and enhanced visible light response. *Journal of the American Chemical Society* 2012, *134*, 4393-7.

(175) Wang, X.; Wang, L.; Zhao, F.; Hu, C.; Zhao, Y.; Zhang, Z.; Chen, S.; Shi, G.; Qu, L.: Monoatomic-thick graphitic carbon nitride dots on graphene sheets as an efficient catalyst in the oxygen reduction reaction. *Nanoscale* 2015, *7*, 3035-3042.

(176) Ge, L.; Han, C.; Liu, J.: In situ synthesis and enhanced visible light photocatalytic activities of novel PANI-g-C3N4 composite photocatalysts. *Journal of Materials Chemistry* 2012, *22*, 11843-11850.

(177) Yan, H.; Huang, Y.: Polymer composites of carbon nitride and poly(3-hexylthiophene) to achieve enhanced hydrogen production from water under visible light. *Chemical communications* 2011, *47*, 4168-4170.

(178) Bai, X.; Sun, C.; Wu, S.; Zhu, Y.: Enhancement of photocatalytic performance via a P3HT-g-C3N4 heterojunction. *Journal of Materials Chemistry A* 2015, *3*, 2741-2747.

(179) Sui, Y.; Liu, J.; Zhang, Y.; Tian, X.; Chen, W.: Dispersed conductive polymer nanoparticles on graphitic carbon nitride for enhanced solar-driven hydrogen evolution from pure water. *Nanoscale* 2013, *5*, 9150-9155.

(180) Hu, S.; Ma, L.; Wang, H.; Zhang, L.; Zhao, Y.; Wu, G.: Properties and photocatalytic performance of polypyrrole and polythiophene modified g-C3N4 nanocomposites. *RSC Advances* 2015, *5*, 31947-31953.

(181) Chen, S.; Hu, Y.; Meng, S.; Fu, X.: Study on the separation mechanisms of photogenerated electrons and holes for composite photocatalysts g-C3N4-WO3. *Applied Catalysis B: Environmental* 2014, *150–151*, 564-573.

(182) Martin, D. J.; Qiu, K.; Shevlin, S. A.; Handoko, A. D.; Chen, X.; Guo, Z.; Tang, J.: Highly Efficient Photocatalytic H2 Evolution from Water using Visible Light and Structure-Controlled Graphitic Carbon Nitride. *Angewandte Chemie International Edition* 2014, *53*, 9240-9245.

(183) Kim, D.; Sakimoto, K. K.; Hong, D.; Yang, P.: Artificial Photosynthesis for Sustainable Fuel and Chemical Production. *Angewandte Chemie International Edition* 2015, *54*, 3259-3266.

(184) Yan, S. C.; Li, Z. S.; Zou, Z. G.: Photodegradation Performance of g-C3N4 Fabricated by Directly Heating Melamine. *Langmuir* 2009, *25*, 10397-10401.

(185) Tang, H.; Lévy, F.; Berger, H.; Schmid, P. E.: Urbach tail of anatase TiO2. *Physical Review B* 1995, *52*, 7771-7774.

(186) Yaghoubi, H.; Li, Z.; Chen, Y.; Ngo, H. T.; Bhethanabotla, V. R.; Joseph, B.; Ma, S.; Schlaf, R.; Takshi, A.: Toward a Visible Light-Driven Photocatalyst: The Effect of Midgap-States-Induced Energy Gap of Undoped TiO2 Nanoparticles. *ACS Catalysis* 2015, *5*, 327-335.

(187) Hauchecorne, B.; Terrens, D.; Verbruggen, S.; Martens, J. A.; Van Langenhove, H.; Demeestere, K.; Lenaerts, S.: Elucidating the photocatalytic degradation pathway of acetaldehyde: An FTIR in situ study under atmospheric conditions. *Applied Catalysis B: Environmental* 2011, *106*, 630-638.

(188) Zhou, Y.; Li, C.; Huijbregts, M. A. J.; Mumtaz, M. M.: Carcinogenic Air Toxics Exposure and Their Cancer-Related Health Impacts in the United States. *PLOS ONE* 2015, *10*, e0140013.

(189) Tomita, O.; Ohtani, B.; Abe, R.: Highly selective phenol production from benzene on a platinum-loaded tungsten oxide photocatalyst with water and molecular oxygen: selective oxidation of water by holes for generating hydroxyl radical as the predominant source of the hydroxyl group. *Catalysis Science & Technology* 2014, *4*, 3850-3860.

(190) Lau, V. W.; Mesch, M. B.; Duppel, V.; Blum, V.; Senker, J.; Lotsch, B. V.: Low-molecular-weight carbon nitrides for solar hydrogen evolution. *Journal of the American Chemical Society* 2015, *137*, 1064-72.

List of published papers and attended conferences

A. Published Papers

1. **Qitao Zhang**, Bin Xu, Saisai Yuan, Ming Zhang, Teruhisa Ohno. Improving g-C_3N_4 photocatalytic performance by hybridizing with $Bi_2O_2CO_3$ nanosheets, Catalysis Today,.DOI:10.1016/j.cattod.2016.10.027. (*In* Press*),* 2017*;*

2. Zhengyuan Jin, **Qitao Zhang**, Liang Hu, Jiaqi Chen, Xing Cheng, Yu-Jia Zeng, Shuangchen Ruan, Teruhisa Ohno. Constructing hydrogen bond based melam/WO_3 heterojunction with enhanced visible-light photocatalytic activity, Applied Catalysis B: Environmental, 205, 569–575, 2017;

3. Bin Xu , **Qitao Zhang**, Saisai Yuan , Sixiao Liu, Ming Zhang, Teruhisa Ohno. Synthesis and photocatalytic performance of yttrium-doped CeO_2 with a hollow sphere structure, Catalysis Today, 281, 135–143, 2017;

4. Bin Xu , **Qitao Zhang**, Saisai Yuan , Ming Zhang, Teruhisa Ohno,Synthesis and photocatalytic performance of yttrium-doped CeO_2 with a porous broom-like hierarchical structure, Applied Catalysis B: Environmental, 183,361–370, 2016;

5. Zhengyuan Jin, **Qitao Zhang**, Saisai Yuan, Teruhisa Ohno, Synthesis high specific surface area nanotube g-C_3N_4 with two-step condensation treatment of melamine to enhance photocatalysis properties, RSC Advances., 5, 4026–4029, 2015;

6. Qingli Huang, **Qitao Zhang**, Saisai Yuan, Yongcai Zhang, Ming Zhang, One-pot facile synthesis of branched Ag-ZnO heterojunctionnanostructure as highly efficient photocatalytic catalyst, Applied Surface Science, 353,949–957, 2015;

7. Bin Xu, **Qitao Zhang**, Saisai Yuan, Ming Zhang, Teruhisa Ohno, Morphology control and photocatalytic characterization of yttrium-doped hedgehog-like CeO_2, Applied Catalysis B: Environmental, 164, 120-127, 2015;

8. ZhenXiong Ma, **Qitao Zhang**, JunLiang Liu, ChangHao Yan, Ming Zhang, Teruhisa Ohno. Preparation of luminescent polystyrene microspheres via surface-modified route with rare earth (Eu^{3+} and Tb^{3+}) complexes linked to 2, 2′-bipyridine, Rare Metals, 34, 590-594, 2015.

9. Bin Xu, **Qitao Zhang**, Saisai Yuan, Ming Zhang, Teruhisa Ohno, Morphology control and characterization of broom-like porous CeO_2, Chemical Engineering Journal, 260, 126-132,2015;

10. Saisai Yuan, **Qitao Zhang**, Bin Xu, Zhengyuan Jin, Ya Zhang, Yin Yang, Ming Zhang, Teruhisa Ohno. Porous cerium dioxide hollow spheres and their photocatalytic performance, RSC Advances**,** 4, 62255-62261, 2014;

11. Ye Chen, Naoya Murakami, Haiyan Chen, Jia Sun, **Qitao Zhang**, Zhifeng Wang,Teruhisa Ohno, Ming Zhang, Improvement of photocatalytic activity of high specific surface area graphitic carbon nitride by loading a cocatalyst, Rare Metals, 1–8, 2014;

12. Teruhisa Ohno, Takayoshi Higo, Naoya Murakami, Hirofumi Saito, **Qitao Zhang**,Yin Yang, Toshiki Tsubota, Photocatalytic reduction of CO2 over exposed crystal face controlled TiO2 nanorod having a brookite phase with co-catalyst loading, Applied Catalysis B: Environmental, 152, 309-316, 2014;

13. **Qitao Zhang**, Bin Xu, Saisai Yuan, Ming Zhang, Teruhisa Ohno, Fabrication and Characterization of Sesame Ball-like CeO2:Y3+/P (St-AA) Composite Microspheres Based on Electrostatic Interaction, Materials Letters, 121,109–112, 2014;

14. Zhenxiong Ma, Junliang Liu, Ye Chen, **Qitao Zhang**, Ming Zhang , Teruhisa Ohno, Facile preparation and characterization of luminescent polystyrene composite microspheres, New Journal of Chemistry, 37,2133-2138, 2013;

15. Zhenxiong Ma, Ye Chen, **Qitao Zhang**, Teruhisa Ohno, Ming Zhang, Facile fabrication of monodisperse fluorescent polystyrene composite microspheres, Advances in Intelligent Systems Research (AISR), 23, 1299-1303, 2012;

16. Zhenxiong Ma, Xingkai Zhang, **Qitao Zhang**, Yan Jiang, Ping Liu, Jiamei Ye, Junliang Liu, Ming Zhang, Controlled synthesis of mono-dispersed cerium oxide nano powders via a mixed solvothermal route, Advanced Materials Research, 610-615, 2012;

B. Attended Conferences

1. **Qitao Zhang** , Teruhisa Ohno, Ming Zhang, Selenium-assisted to fabricate g-C_3N_4 nanorods array hybridized with CeO_2 nanocrystals to enhance the visible-light-driven photocatalytic performance, International Symposium on Catalysis and Fine Chemicals 2016 (C&FC 2016), November 10-14, 2016 , Taipei, Taiwan.

2. **Qitao Zhang** , Ming Zhang, Teruhisa Ohno, Selenium-assisted to fabricate g-C_3N_4 nanorods array with enhanced visible-light-driven photocatalytic performance, The 16th International Congress on Catalysis (ICC 16), July 3- 8, 2016, Beijing, China.

3. **Qitao Zhang**, Naoya Murakami, Teruhisa Ohno, Improvement of Photocatalytic Activity of g-C3N4 by composite with Morphology Controlled CeO2 under Visible Light Irradiation, CSJ West Japan Chemistry Forum, November 16-17, 2013, Hiroshima, Japan

Acknowledgements

Starting with an old saying 'Time flies, One's youth never returns'. Involuntarily, I have been studied in Japan for four years. I still remember the day, with utmost care and yearning, I left my hometown to an unconversant country. Now as graduation day draws near, similar mixed feelings well up in my heart. Firstly, I would like to devote my gratitude to all those who helped me during the master and doctor course. My deepest gratitude goes first and foremost to my two superadvisors: Professor Teruhisa Ohno and Professor Ming Zhang. During my master and doctor study, they helped me so much, not only in the guidance of my research work but also in relieving my economic pressure. Professor Ohno is a humor and knowledgeable man, he is my abecedarian teacher to explore the world of photocatalysis, and his outstanding achievements in photocatalyst research always motivate me to work hard. I wish him good health, happiness and remember to have rest. Secondly, I would like to express heartfelt gratitude to associate Professor Toshiki Tsubota, Naoya Murakami, Changhao Yan, Junliang Liu, assistant Professor Sunao Kamimura, they also assist me to improve my research skills. Then my thanks would go to every members of in my laboratory and my research partners, especially to Dr. Zhenxiong Ma, Dr. Zhifeng Wang, Dr. Bin Xu, Dr. Saisai Yuan, Dr. Zhengyuan Jin, Dr. Jinquan Wang, Dr. Qingli Huang, Dr, Yuqing Li, Dr. Keisuke Hamada, M.S. Sixiao Liu, M.S. Yamashita Shimpei and so forth, they taught me how to use the machines for characterizations and discussed with me to solve academic problem and daily life issues. Last but not the least, I thank my parents and two sisters to support me study in Japan. Finally, I'd like to give my special thanks to my wife WEI LUAN and my daughter Enxi Zhang, they give me a happy family and I will always love them.

What an unforgettable experience it is !!!